CHALMERS

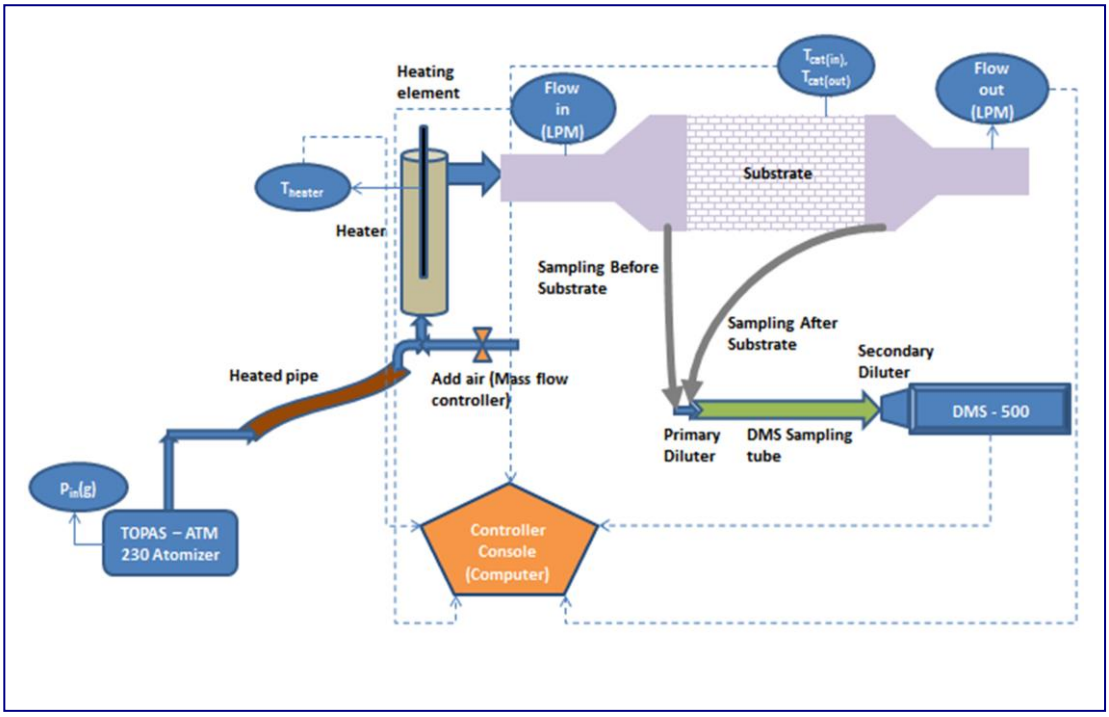

‘Particulate matter removal in automotive after-treatment systems’

Master Thesis in the Master’s programme in Innovative and Sustainable Chemical Engineering (MPISC)

ANANDA SUBRAMANI KANNAN

HOUMAN OJAGH

Department of Applied Mechanics
Division of Combustion and Division of Fluid dynamics
CHALMERS UNIVERSITY OF TECHNOLOGY
Göteborg, Sweden 2013

Master’s thesis 2013:33

MASTER THESIS IN INNOVATIVE AND SUSTAINABLE CHEMICAL ENGINEERING (MPISC)

‘Particulate matter removal in automotive after-treatment systems’

ANANDA SUBRAMANI KANNAN

HOUMAN OJAGH

Department of Applied Mechanics
Division of Combustion and Division of Fluid dynamics
CHALMERS UNIVERSITY OF TECHNOLOGY
Göteborg, Sweden 2013

Particulate matter removal in automotive after-treatment systems

ANANDA SUBRAMANI KANNAN
HOUMAN OJAGH

Master Thesis 2013:33
ISSN 1652-8557
Department of Applied Mechanics
Division of Combustion and Division of Fluid dynamics
Chalmers University of Technology
SE-412 96 Göteborg
Sweden
Telephone: + 46 (0)31-772 1000

Cover:
Modified exhaust after treatment system.

Chalmers reproservice
Göteborg, Sweden 2013

Particulate matter removal in automotive after-treatment systems

Master Thesis in the Master's programme in Innovative and Sustainable Chemical Engineering (MPISC)

ANANDA SUBRAMANI KANNAN
HOUMAN OJAGH
Department of Applied Mechanics
Division of Combustion and Division of Fluid dynamics
Chalmers University of Technology

ABSTRACT

There is growing concern in the world with regard to pollution and climate change. The relation between air pollution and climate change in particular is strong and complex. There is thus a shift towards greener technologies and a large amount of resources have been allocated for the research and development of such technologies. As emission regulations are becoming stricter, there is a concerted effort from all fronts in the EU to design and develop an optimal exhaust after-treatment system which would concur with current emission regulations imposed by Euro V and Euro VI (0.005 g/km of particulate matter (PM) and particulate number (PN) 6.0×10^{11}) for both gasoline and diesel powered drives). Open channel substrates (described in this work) are used for the removal of particulate matter from exhaust. Such substrates are made of channels (arranged in a honeycomb structure) which permit the flow of exhaust through them. The PM is ultimately trapped on the wall of these channels.

Over the past decade there has been a substantial increase in the computational power available to researchers. This increase of available computational resources has shifted the prime focus of research from time-consuming and expensive construction of pilot-scale prototypes towards simulation-driven development of new after treatment solutions. The current work aims to describe such a feedback between experiments and simulations in order to describe the capture of an inert particle (sodium chloride - NaCl) in an open substrate (monolith channel). The experiments and simulations are done in conjunction and such a systematic approach improves the quality of the experimental evaluation. This congruence is evident throughout this work, with the simulations generally, corresponding to the experimental results (simulations results are within the error limit of the experimental results). Both temperature and residence time have a significant impact on the capture efficiency due to Brownian deposition along an open channel. In addition the general trends with variation in residence time (flow conditions) and temperature are noticeably similar in both experiments and simulations. This indicates that the theory behind the description of capture efficiency in open channels (Brownian deposition in open substrates) is able to explain the capture phenomena of inert particulates accurately.

Key words: Computational, Brownian deposition, Capture efficiency, Inert particulates, Particulate matter, Particulate number, Open substrates

Contents

Preface

This master thesis has been conducted for the fulfilment of the Master of Science degree in Innovative and sustainable chemical engineering at Chalmers University of technology, Göteborg, Sweden. In this thesis, experimental and numerical evaluations (CFD simulations) have been performed in order to describe the capture of an inert particle (sodium chloride - NaCl) in an open substrate (monolith channel). These have been done in conjunction and such a systematic approach has thus improved the quality of the experimental evaluation. The thesis has been carried out from January 2013 to June 2013.

The thesis has been executed under the supervision of Dr. Jonas Sjöblom (Assistant professor at the Division of Combustion) and Dr. Henrik Ström (Post-doctoral researcher at the Division of fluid dynamics) at Chalmers University of technology. We would like to thank both Jonas and Henrik , who have been our mentors, for their constant guidance and support. This thesis would not have materialized without their vision. We would also like to thank our examiners Sven Andersson (Associate professor at the Division of Combustion) and Srdjan Sasic (Associate professor at the Division of fluid dynamics) for their for their guidance and technical insights during the course of our research. All experimental trials have been carried out in the research laboratories of the Division of combustion at Chalmers University of Technology, Göteborg. We would like to extend our heartfelt gratitude towards all the support staff at the labs - Alf Magnusson, Eugenio De Benito Sienes and Daniel Härensten for providing pragmatic and rapid solutions to some of the problems encountered during the experimental trials.

Finally, we would like to thank our family and friends who have stood by us through the entire period and have made this experience a memorable one.

Göteborg June 2013

Ananda Subramani Kannan

Houman Ojagh

ABBREVIATIONS

CE	Capture efficiency
DL	Diffusion losses
DOC	Diesel oxidation catalyst
DPF	Diesel particulate filter
EATS	Exhaust after treatment system
HC	Hydrocarbon
EC	Elemental carbon
NO_x	Nitrous oxide and Nitrogen dioxide
PE	Penetration efficiency
PM	Particulate matter
PN	Particulate number
TWC	Three way catalyst

Nomenclature list

A	Parameter vector for secondary dilutor losses	$[m^2s^{-1}]$
A’	Coefficient	[-]
α_c	Condensation coefficient	[-]
α, β and γ	Experimentally determined coefficients	[-]
A_S	Surface area (channel)	$[m^2]$
A_w	Area (pocket wall)	$[m^2]$
C	Cunningham correction factor	[-]
C_D	Drag coefficient	[-]
CE	Capture efficiency	[%]
D_{ab}	Diffusion coefficient	$[m^2s^{-1}]$
D_p	Particle diffusivity	$[m^2s^{-1}]$
d_h	Channel hydraulic diameter	[m]
d_p	Particle diameter	[m]

d_t	Tube diameter	[m]
E	Uncertainty measure for CE	[%]
g_i	Acceleration due to gravity	[ms^{-2}]
h_m	Average mass transfer coefficient	[ms^{-1}]
J_i	Diffusion flux of species 'i'	[cm^{-2} s^{-1}]
k_B	Boltzmann constant	[J]
Kn	Knudsen number	[-]
L	Characteristic pipe Length	[m]
Λ	Mean free path	[nm]
M	Molecular mass	[kg/mole]
m_{in},m_{out}	Mass in and mass out over a differential volume	[kg]
μ	Dynamic viscosity	[Pas]
N_{in}, N_{out}	Number of particles	[Ncm^{-3}]
N_A	Avogadro's number	[$mole^{-1}$]
p_∞, p_d	partial pressure in bulk, at particle surface	[Pa]
PE	Penetration efficiency	[%]
PSD	Particle size distribution	[$dN/dlog(d_p)$]
Q	Volumetric flow rate	[m^3s^{-1}], [dm^3min^{-1}]
Re, Re_p	Reynolds number and particle Reynolds number	[-]
R_i	The net rate of production of species 'i' by chemical reaction	[$mols^{-1}$]
ρ_g, ρ_p	Density for gas, particle	[kgm^{-3}]
Sh	Sherwood number	[-]
T	Temperature	[K], [°C]
$\overline{U}$, Ui, Uj	Average linear (pipe) velocity	[ms^{-1}]
V	Volume	[m^3]
V_d	Deposition velocity	[ms^{-1}]
X, Y_i	Mass fraction	[-]
x, y	Space coordinates	[m]

1 Introduction

This section gives the background to this work and describes the primary objectives that are to be achieved. The aim is defined together with a brief review of relevant works which put the current study into perspective.

1.1 Background

There is growing concern in the world with regard to pollution and climate change. The relation between air pollution and climate change in particular is strong but complex (EEA, 2012). There is thus a shift towards greener technologies and a large amount of resources have been allocated to research and develop such technologies.

Vehicles that run on carbon based fuels are the primary contributors to many different air pollutants such as carbon monoxide (CO), various hydrocarbons (HC), nitrogen oxides (NO_x), particulate matter (PM) and finally carbon dioxide (CO_2). The presence of CO and HC is due to incomplete combustion, whereas NO_x is mainly formed from nitrogen in the air due to the high temperatures inside the engine and at the end carbon dioxide (CO_2) is formed as the final product of fossil fuel combustion. The particulate matter (PM) emissions from engines are composed predominantly of elemental carbon (EC or soot), organic carbon (HC) and sulphates. The elemental fraction stems from fuel droplet pyrolysis, while the organic fraction originates from unburned fuel, lubricating oil, and combustion by-products (Shah, Cocker, Miller, & Norbeck, 2004). These PM emissions from diesel engines are a significant source of small (< 2.5 μm) particles in urban areas, and epidemiology has demonstrated that susceptible individuals are being harmed by ambient particulate matter (Lighty, 2004). Reducing these emissions may warm or cool the atmosphere because several of these pollutants demonstrate a positive or a negative climate-forcing impact, either directly or indirectly (EEA, 2012). The direct climatic impacts include effects of sulphate aerosols which reflect solar radiation leading to net cooling and the effects of EC aerosols which absorb solar radiation leading to warming. Indirect impacts include aerosols altering cloud properties and NO_x promoting tropospheric O_3 formation that warms the atmosphere and acid rain (Balkanski et al., 2010).

In addition, higher emission of carbon dioxide (CO_2) as a greenhouse gas leads to higher concentrations in the atmosphere that affects the biological carbon cycle. In other words, CO_2 contributes to global warming (Cox, Betts, Jones, Spall, & Totterdell, 2000).

In order to meet the challenges from upcoming legislation and to contribute to a sustainable future, emissions and the contents of particulate matter in engine exhaust must be reduced in terms of both mass and number. In conventional stoichiometric gasoline engines, the three-way catalyst (TWC) can be used to oxidize CO and HC and reduce NO_x simultaneously. However, CO_2 cannot be converted over this catalyst. If emissions of CO_2 are to be reduced, there must instead be a change of fuel, an increase in fuel efficiency and/or an overall change of engine technology (e.g. from combustion engine to fuel cell or electrical battery) (Ström, 2011).

Over the past decade there has been a substantial increase in the computational power available to researchers. This increase of available computational resources has shifted the prime focus of research from time-consuming and expensive construction of pilot-scale prototypes towards simulation-driven development of new after treatment solutions. Not only are there huge savings

to be made on cutting the design and development time (Oberkampf & Trucano, 2002), but also computational simulations can often provide more information than what is available from traditional experimental techniques. Hence the use of experimental investigations in conjunction with mathematical modelling (using say computational fluid dynamics (CFD)) would provide a comprehensive insight into any system being studied.

The following master thesis aims to describe the capture of an inert particle Sodium Chloride (NaCl), in a monolith channel. Monoliths are configurations that contain several types of interconnected or divided channels (straight, wavy or crimped) in one single chunk of material (e.g. honeycombs, foams or interconnected fibres). The channels of the most common honeycomb monoliths normally have circular, square or triangular cross sections. The capture efficiency of the channel is estimated using PM measurements of the flow entering and leaving the channel. In addition, numerical modelling (using CFD) of the same capture phenomenon is also detailed in order to supplement the experimental findings. This co-dependency between the two afore-mentioned strategies forms the crux of the work being presented in this dissertation.

1.2 Problem description

An extensive investigation of capture phenomena (including experimental trials and numerical simulations) of diesel particulate matter in open substrates has recently been performed at the research labs in the Division of combustion, Department of Applied mechanics, Chalmers University of Technology, Göteborg (Sjöblom & Ström, 2013). The aim of this work was to compare theoretical models for PM capture (achieved using CFD simulations) with experimental results in order to correlate theory with experiments. However, due to inherent complexities encountered during their study, there were strong dissimilarities between experiments and simulations. These dissimilarities were later attributed to the model used for the simulations, which assumed that diesel particulate matter is inert in nature (which is not necessarily true). A simple conceptual model was therefore constructed to explain the experimental findings and fit it closely with the simulations. This model accounted for loss of material by total evaporation (of particles that are entirely made out of HCs) as well as by shrinkage (by evaporation from particles with condensed HCs on their surface). It must be noted that, this model is valid only if it can be confirmed that the CFD simulations and experimental trials are indeed comparable for an inert substance. Thus a new study project to investigate the capture phenomena of inert solid particles (instead of diesel particulate matter) in open substrates was proposed.

1.3 Objectives of this work

Capture efficiency experiments and simulations were planned in order to achieve congruence between theory and experiments. The size dependent capture efficiency is evaluated and compared with numerical simulations, showing how various transport processes (diffusion, evaporation etc.) influence the capture results. In addition, the other goals of this work can be summarized as follows –

- Examine the possibility to generate and measure inert particles using an aerosol generator.
- Design and conduct experiments that will enable a close comparison with computational fluid dynamics (CFD) simulations as well as produce a robust methodology for PM measurements (including the design of thermo couple probe positions, sample flow conditions and PM instrument settings (dilution factors)).

- Identify appropriate operating conditions while performing studies on open substrates
- Simulate flow and PM motion in a single monolith channel.

1.4 Theory

As explained earlier, the primary objective of this work is to describe the capture phenomena in open substrates. This would thus entail a brief description of particulate matter capture in conventional exhaust after-treatment systems and a general outlook on PM measurements. A brief description of numerical modelling approaches for PM capture in monoliths is also provided in order to elucidate the fundamental concepts behind the simulations which would be presented later in this work.

1.4.1 Particulate matter (PM)

Particulate matters from diesel engines (PM) are generally defined as solid or liquid particles made of elemental carbon (EC), adsorbed hydrocarbons (HC) and inorganic compounds such as sulphates, metallic compounds and water formed during exhaust dilution and cooling (Hinds, 1999). Yet, the most common definition of PM states everything that is collected on a filter paper in exhaust that has been diluted and cooled to 52°C (SAE, 1993). Figure 1.1 illustrates idealized number and mass weighted size distributions for diesel particulate matter. PM follows a lognormal, tri-modal size distribution with the concentration in any size range being proportional to the area under the corresponding curve in that range.

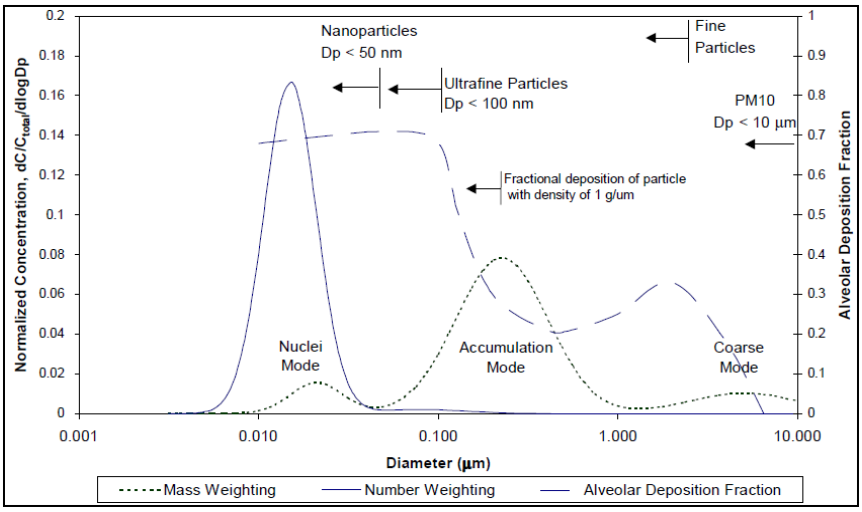

Figure 1.1- Illustration of the size distribution of diesel particulate matter (figure adapted from - (Kittelson, 1998))

Nuclei-mode, which are the smallest and primary particles formed during the combustion in the engine cylinder, range in diameter from about 5 to 50 nm. The nuclei-mode (refer Figure 1.1 above) also includes droplets that nucleate upon cooling of the exhaust. These usually contain 1-20 % of the particle mass and more than 90 % of the total particle number. The accumulation mode ranges in size from roughly about 30 to 500 nm. Most of the mass is composed primarily

of carbonaceous agglomerates and adsorbed materials. Finally, the coarse mode consists of particles larger than about 1 (μm) and typically contains 5-20 % of the diesel particulate matter mass (Kittelson, 1998).

1.4.2 Exhaust after-treatment systems

As emission regulations are becoming stricter, there is a concerted effort from all fronts in the EU to design and develop an optimal exhaust after-treatment system which would concur with current emission regulations imposed by Euro V and Euro VI (0.005 g/km of PM and PN 6.0×10^{11}) for both gasoline and diesel powered drives)(Euro-5/6-Standards, 2009). The design of such a system is complex and would require the combined effect of several individual emission abatement technologies. The most commonly employed emission control technologies in a diesel driven system are – diesel oxidation catalyst (DOC), diesel particulate filter (DPF) and diesel NO_x reduction filter (DeNOx). A schematic figure of an after-treatment system employing these three filters is presented in the figure below.

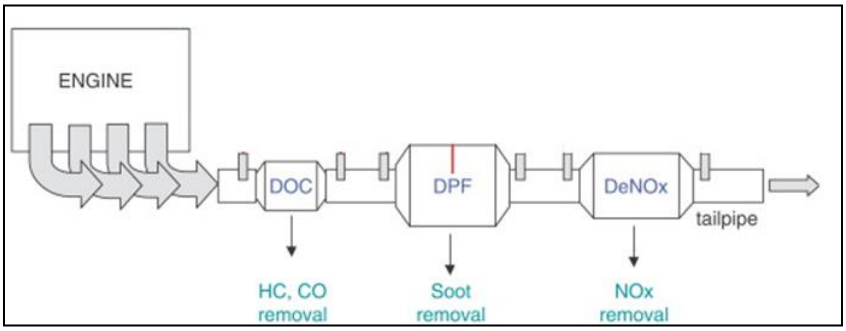

Figure 1.2- An integrated soot-NO_x emission control system (Figure adapted from Konstandopoulos et.al 2004)

The DOC (diesel oxidation catalyst) is a monolithic reactor which is designed to effectively oxidize gaseous pollutants. In this way, the usual products of incomplete combustion, carbon monoxide (CO) and various hydrocarbons (HC) , are finally converted into carbon dioxide (CO_2) and water (H_2O). Since the diffusion of particulate matter to the catalytically active walls of the standard monolithic reactor is very slow and ineffective, the monolithic reactor has not been successful at reducing the particulate matter content and comply with legislation in its original design (Ström, 2011). The wall-flow diesel particulate filter (DPF) is instead the most commonly used reactor for removal of particulate matter in diesel applications (Konstandopoulos & Kostoglou, 2004).

Since the current work focuses particularly on PM capture, the DPF would be the most apt system to describe in order to put this work in perspective. There are a variety of DPFs available. For example, the DPF could be made of composite fibrous materials which utilize fine fibres as a means of particle filtration. The DPF may also be an extruded wall-flow monolithic filter, which is commonly made of cordierite or silicon carbide material. A wall-flow monolith is the most common type of filtration element employed. In such a DPF, every second channel in the ceramic monolithic reactor is plugged in either end, creating a chessboard-like appearance of the monolith front and back (Adler, 2005). The exhaust gas is therefore only allowed to enter the channels which are open towards the inlet side, the so-called inlet channels. The gas is then forced to flow through the porous wall into the four adjacent outlet channels. The DPF accumulates particles on the inside and on the porous walls of the inlet channels (Liu, Berg,

Swor, & Schauer, 2008). The main technical challenge for DPF systems in automotive applications is their regeneration from the soot they retain from the exhaust gases (Vaaraslahti, Virtanen, Ristimäki, & Keskinen, 2004).

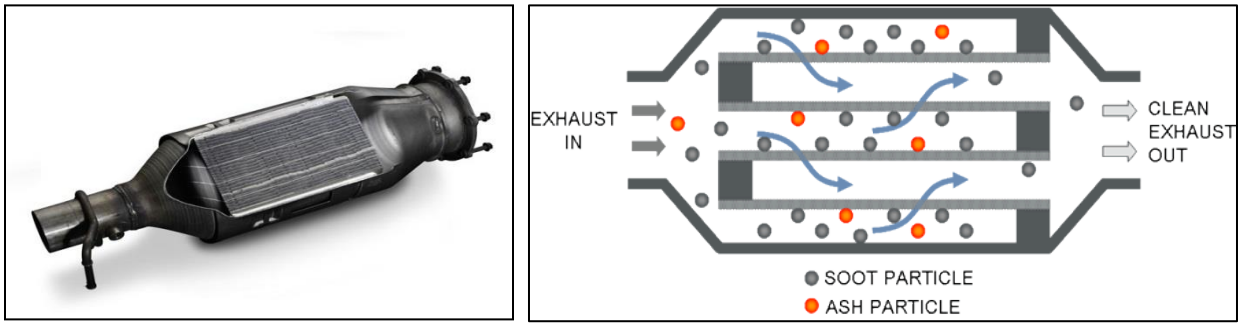

Figure 1.3 – Standard DPF (left) (Figure courtesy of Northeast remaps Durham DPF removal). DPF design (right)- The channels are plugged in either end (grey), forcing the gas to flow through the walls (arrows) and the soot (black) is deposited along the inlet channels.(Figure courtesy of Castrol Lubricants, Division of BP EUROPA SE - BP NETHERLANDS)

The work described here pertains to exhaust flow through open filters. This filter is very similar to a DPF in its design and operation, the only difference being that no channels are plugged. This would mean that the exhaust gas would flow through each and every channel unhindered. Such open filters (with low pressure drop) have potential for efficient reduction of particulate matter from diesel driven systems. The core component of both the DPF and open filter is the monolith channel alone, as it is along the wall of these channels that PM trapping is achieved.

Monolithic reactors are either made of porous catalytic material or channels that are filled with layers called washcoat which contain catalytic material in the empty space (porous zone). In both arrangements, the channels provide the space for the flow of gas and/or liquid. Presently, ceramic and metallic monoliths are the two major types of monolith supports that are used in both industry and research. In the case of the square-channel monolith, the monolith geometry is fully defined by three parameters: channel size (d_h), wall thickness (W_t) or cell density (n) and the channel length (L). If the monolith is extruded from a catalytic material, the amount of catalyst in the unit volume of the reactor is fully determined by the monolith (Tomašić & Jović, 2006). The channels of the substrate have square cross-sections, which are rounded by the washcoat as it is deposited onto the channel walls. Among these parameters, channel size and shape affect the pressure drop across the channel and the hydrodynamics of the flow. A typical ceramic substrate design is illustrated in the figure below –

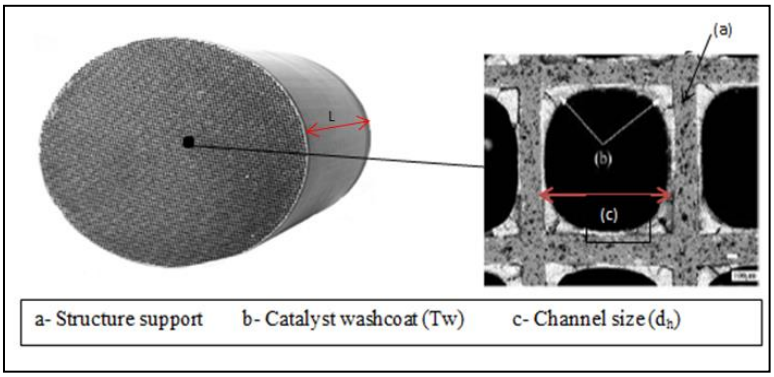

Figure 1.2- Illustration of the monolith channels (Figure courtesy of (Creaser, 2013))

1.4.3 Numerical aspects of modelling PM capture in open substrates

The capture of PM in open substrates is very complex to model. These complexities stem from the wide variety of time and length scales that need to be independently resolved by a computational grid in order to adequately describe the phenomenon. In addition, due to the simultaneous interaction between the two phases (solid particles and exhaust gases) within the system, the solution to such a numerical problem is complicated further. There are several strategies that have been described in literature in order to model and simulate these complex multiphase phenomena. Such simulations of multiphase and multicomponent flows pose greater challenges than that of single-phase and single-component flows primarily due to the interfaces between phases and the large or discontinuous property variations across these interfaces between the phases and/or components (Hanratty et al., 2003). The strategies adopted to model such a system (a dispersed gas-solid system) are described below.

The continuum framework and Navier-Stokes equations

The concept of the continuum is important in the development of equations for multiphase flows. A fluid is regarded as consisting of continuous matter for which properties such as density and velocity vary continuously from point to point. This idea is important in the development of the differential forms of the conservation equations (Crowe, Schwarzkopf, Sommerfeld, & Tsuji, 2011). A fluid is typically composed of a vast number of molecules. There are for example more than 10^{25} molecules in one cubic meter of air at room temperature and atmospheric pressure. It is therefore not realistic to predict the individual motion of all the molecules contained within a system. However, if the smallest volume of interest in an analysis still contains a sufficient number of molecules, it is possible to obtain meaningful statistical averages. The molecules are then treated as a continuous distribution of matter, i.e. as a continuum.

The Navier-Stokes equations (basic governing equations for a viscous, heat conducting fluid) are generally applied only to such a continuum framework. These equations are derived from two fundamental principles: the conservation of mass and Newton's second law of motion. These equations describe how the velocity, pressure, temperature, and density of a moving fluid are related. The Navier-Stokes equations consist of a time-dependent continuity equation for conservation of mass, three time-dependent conservation of momentum equations and a time-dependent conservation of energy equation.

Newton's law of conservation of matter states that – '*Matter can neither be created nor be destroyed*' (Milton & Willis, 2007). This law in the differential form for an incompressible fluid would be represented as follows -

$$\frac{\partial u_i}{\partial x_i} = 0 \qquad (1.1)$$

Equation (1.1) is referred to as the continuity equation (for an incompressible fluid). Newton's second law of motion for a fluid control volume states that the time rate of change of momentum within the control volume is given by the sum of the external forces acting on the control volume minus the net rate of momentum efflux. In differential form, the momentum balances for a Newtonian fluid in the three coordinate directions are represented as follows (Navier, 1822; Stokes, 1845):

$$\rho\left(\frac{\partial u_i}{\partial t}+u_j\frac{\partial u_i}{\partial x_j}\right)=-\frac{\partial p}{\partial x_i}+\frac{\partial}{\partial x_j}\left(\mu\frac{\partial u_i}{\partial x_j}\right)+\rho g_i \qquad (1.2)$$

Two fundamental fluid properties appear in these equations: the density (ρ), which is defined as the mass per unit volume, and the viscosity (μ), which is a measure of the fluid resistance to the rate of deformation when acted upon by shear forces. The solution to equations (1.1) and (1.2) under appropriate initial boundary conditions would yield the entire velocity and pressure field in a given domain. Analytical solutions of the above equations do not exist in many cases as they are non-linear partial differential equations. Numerical analysis is the only way to find solutions of these equations and this can be achieved using computational fluid dynamics simulations (CFD).

Computational fluid dynamics is, in part, the art of replacing the governing partial differential equations of fluid flow with numbers, and advancing these numbers in space and/or time to obtain a final numerical description of the complete flow field of interest. In a CFD approach, the bounding geometry is first defined and is then discretized into fine computational grids. This fine discretization of the computational domain into 'finite volume cells' is performed so as to apply the fundamental physical principles to the fluid inside the control volume, and to the fluid crossing the control surface (if the control volume is fixed in space) (Wendt, 2009). Thereafter, the equations governing the flow field must also be discretized. In the current work, the well-established finite-volume method has been employed for this purpose.

Lagrangian Particle Tracking (LPT)

In fluids there are two important vantage points from which a flow problem can be analysed i.e. '*The Eulerian framework*' and '*The Lagrangian framework*'. The Eulerian framework examines changes in velocity or acceleration at a constant point in space. Such a description could be generically represented as: $v(x,y,z,t)$; where the velocity depends on the location and time at which it is observed. The Lagrangian framework is useful when the flow is followed along with the particles of fluid. In this case the velocity is analysed as a function of time for individual parcels of fluid, identified by their starting position (x_0, y_0, z_0); where $x(x_0, y_0, z_0, t)$ are the locations of the fluid parcels as they flow through the system (Guo, Fletcher, & Langrish, 2004).

The LPT approach is used to denote a family of modelling and simulation techniques wherein droplets or particles are represented in a Lagrangian reference frame while the carrier–phase flow field is represented in an Eulerian frame. This methodology is sometimes referred to as '*The point particle approach*' in which the dispersed phase is represented as a point process in the Lagrangian frame and the carrier phase represented as a continuous field in the Eulerian frame (Daley & Vere-Jones, 1988).

The motion of particles in the carrying fluid is described in a Lagrangian way by solving a set of ordinary differential equations along the trajectory. The change of particle location and the particle velocity are estimated by solving these equations. The relevant forces acting on the particle need to be accounted for. The differential equations for calculating the particle location and velocity are given by Newton's second law (the rate of change of the particle's linear momentum is equal to the net sum of the forces acting on the particle) given by –

$$m_p\left(\frac{dv}{dt}\right)=F_{body}+F_{surf}+F_{coll}+F_{mol} \quad (1.3)$$

The right hand side (RHS) includes the forces associated with these temporal changes. Body forces (F_{body}) are those proportional to the particle mass, surface forces (F_{surf}) are those proportional to the particle surface area and related to the surrounding fluid stress, collision forces (F_{coll}) includes the effects of other particles or walls which may come in contact with the particle and the molecular forces (F_{mol}) whose effects appear at the molecular abstraction level.

The body forces are assumed to be represented solely by the gravitational force (F_g) which acts in the direction of the gravity acceleration vector (g), such that

$$F_{body}\approx F_g=m_p g \quad (1.4)$$

This assumes that other body forces (such as electromagnetic forces) are negligible. The surface force for a spherical particle can be written in terms of the pressure and viscous stresses acting over a differential surface area. These can be represented as a linear sum of various decomposed fluid dynamic forces related to certain flow properties. This can be represented as –

$$F_{surf}=F_D+F_L+F_V+F_H+F_S \quad (1.5)$$

These individual components include forces due to:

drag (F_D) which resists the relative velocity, lift (F_L) which arises due to particle spin or fluid shear, virtual-mass (F_V) which is related to the surrounding fluid that accelerates with the particle, history (F_H) which takes into account unsteady stress over the particle, fluid-stress (F_S) which stems from the fluid dynamic stresses in the absence of the particle,

The surface molecular forces consist primarily of the Brownian motion (F_{Br}) i.e. random motion from discrete molecular interactions, and a thermophoresis (F_T) force due to molecular interactions along a temperature gradient (Loth, 2009).

$$F_{mol}=F_{Br}+F_T \quad (1.6)$$

The system described in this dissertation would consist of an inert particle (dispersed phase) in the nano-scale traversing in air (carrier phase). Thus, several of the aforementioned decomposed fluid dynamic force components are not applicable due to the inherent nature of such a system. The particles tracked are significantly smaller than 1 μm hence they would not alter the continuous phase in any manner.

Furthermore, there are a variety of interactions which can occur between the two phases (particle-fluid interactions) and among the dispersed-phase (particle-particle interactions). Particle-fluid interactions encompass both the effects of the continuous-phase on the particle trajectories and the effect of the particles on the continuous-phase flow distribution. Particle-particle interactions can refer to two separate mechanisms: fluid-dynamic interactions and collisions. Particle-particle fluid-dynamic interactions occur when the presence of one particle directly affects the fluid dynamic forces of a neighbouring particle (such as by drafting). In contrast, particle-particle collisions occur when particles come into direct contact with each other (when particles rebound, shatter, or coalesce). There are several regimes which describe the degree and type of coupling which occurs between particle motion and that of its surroundings. Four different coupling regimes have been widely described in literature, these are –'one-way coupling': particle-phase motion affected by the continuous-phase but not vice-versa, 'two-way

coupling': particle-phase also affects the continuous-phase through fluid coupling, 'three-way coupling': flow disturbances caused by particles affect the motion of nearby particles and 'four-way coupling': contact collisions also influence the overall particle motion (Crowe et al., 2011).

In the current work, due to the inherent size and nature of the particles being discussed, only the 'one-way coupling' regime is of significance. Moreover, in order to simplify the system, low particle loading is assumed which would mean that the inter-particle collision effects ('four-way coupling') can be neglected. In addition, due to the significant density difference between the particle and the surrounding fluid ($\rho_f/\rho_p <<< 1$), the lift and the history force components in equation (1.5) can be neglected. The added mass force component is neglected ($\rho_p <<< \rho f$). The molecular Brownian forces on the other hand are very critical in such nano-scale particulate flows (F_{Br} affects any particle smaller in size than a micron) and have thus been included in the particle's equation of motion (eq. 1.7) along with the drag (F_D) and body forces (F_g). The thermophoretic forces have not been modelled due to the negligible temperature gradients within the system described here (in the monolith channels the best operating conditions would be adiabatic). Thus the final particle equation of motion would have the following form –

$$m_p\left(\frac{dv}{dt}\right)=F_D+F_g+F_{Br} \tag{1.7}$$

A more detail account of how the drag and Brownian forces are modelled is provided in the sections below.

Rarefied gas dynamics and steady state drag

Rarefied gas dynamics is based on the kinetic approach to gas flows. In 1859 Maxwell abandoned the idea that all gaseous molecules move with the same speed and introduced the statistical approach to gaseous medium, namely, he introduced the velocity distribution function and obtained its expression in the equilibrium state. The principal parameter of rarefied gas dynamics is the Knudsen number (Kn) which characterizes the gas rarefaction. It is defined as follows –

$$Kn=\frac{\lambda}{L} \tag{1.8}$$

Where, λ is the molecular mean free path and L is the characteristic length scale of the flow. Maxwell's expression is generally used to estimate molecular mean free path. This expression is given as –

$$\lambda=\frac{\mu_g}{0.499\rho_g\left(\frac{8P}{\pi\rho_g}\right)^{\frac{1}{2}}} \tag{1.9}$$

Where, μ_g and ρ_g are the viscosity and the density of the surrounding air and P is the pressure of the gas. At ambient conditions, λ is about 67 nm (Ström, 2011).

Based on the Knudsen number, we may distinguish the following three regimes of gas flow. If the Knudsen number is small (Kn<<1), the gas can be considered as a continuous medium and the hydrodynamic equations (Navier stokes equations) can be applied. This regime is called hydrodynamic. If the Knudsen number is large (Kn>>1), the mean free path is very large

compared to the spatial scales of the fluid flow thus the continuum concept is no longer valid. Under this condition we can neither consider the gas as a continuous medium nor discount the intermolecular collisions. In this case the kinetic equation should be solved and this regime is called transitional. The work described here (nanoparticles of size 20-100 nm → 2.5 <Kn<13.35) would involve this free transition regime primarily. As the size of the particle becomes comparable to the mean free path of the gas, the particle will no longer face the gas as a continuum, but rather collide with a large number of individual molecules. Therefore, continuum fluid mechanics has to be modified in order to obtain accurate predictions of particle motion (Sharipov, 2007). The geometry of the flow discussed in this work is large when compared to the size of the particles. It is then possible to account for rarefaction using a simple correction to the usual drag coefficient (as the size of the computational mesh for resolving the flow field is much larger than the particle) and also, model Brownian motion. The expression for steady state drag along with the afore-mentioned correction is discussed in the sections below.

Steady state drag force is defined as a force that is imposed by the carrying fluid on droplets or particles when there is no acceleration due to relative velocity between particles and the carrier phase (Loth, 2009). The steady state drag is formulated as-

$$F_D = \frac{1}{2}\rho_c C_D A \left|u_c - u_p\right| (u_c - u_p) \tag{1.10}$$

Where ρ_C is the carrier phase density, C_D is the drag coefficient, A is the area of the particle (the projected area of particle in the direction of flow) and finally (u_c- u_p) represents the relative velocity between the phases (particle and fluid). The drag coefficient can be affected by a number of factors such as particle shape, particle Reynolds number (Re_p), Mach number, turbulence level etc. It is thus essential that the drag coefficient is accurately determined based on the system conditions. The shape characteristics of a solid particle exert a profound influence on its ability to absorb momentum from a moving fluid stream and therefore can greatly affect the drag force (Carmichael, 1982). As mentioned earlier, the system described in this work would primarily consist of spherical particles. Hence, the treatment of such a particle will only be discussed in this section.

There are many equations in literature relating the drag coefficient to the Reynolds number for particles (Re_p) falling at their terminal velocities. For a spherical particle, these empirical relations are available as drag coefficient curves (C_D vs Re_p) which can be used to accurately estimate the drag coefficient. The variation of the drag coefficient with Reynolds number for a non- rotating sphere is shown in Figure 1.5 below.

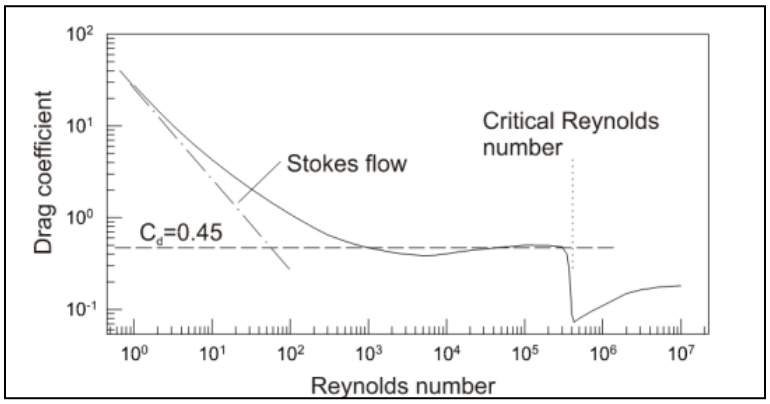

Figure 1.5 – Drag coefficient (C_D) as a function of Particle Reynolds number (figure adapted from Crowe et.al. 2011)

For lower values of Reynolds numbers ($Re_p < 1$), also known as Stokes flow or the creeping flow regime, the inertial tem in the Navier-Stokes equation is negligible and the drag coefficient can be approximated as 24/Re. As Reynolds number gets higher (Re ~ 5) the inertial forces become more significant and the flow around particle begins to separate.

Under the creeping flow conditions (refer Appendix I) , Stokes solved the equations of motion in radial coordinates for a rigid sphere of radius, R, moving at a constant velocity (v) in a stagnant fluid and obtained an expression for the fluid drag force (F_D) (Stokes, 1845). The expression is as follows -

$$F_D=-6\pi\mu Rv \tag{1.11}$$

Where μ is the viscosity of the fluid and the negative sign indicates the opposite directions of v and F_D. Stokes law is a solution for the drag force (F_D) of a rigid sphere obtained by solving the Navier-Stokes equations in the viscous limit of $Re_p << 1$. The solution imposes no-slip at the particle surface and, therefore, assumes that the relative velocity of the fluid is zero at the surface. This assumption begins to break down for particle diameters several times the gas mean free path when such particles experience 'slip' at their surface (as is the case in the current work) (Kim, Mulholland, Kukuck, & Pui, 2005). Cunningham was the first to recognize the existence of 'slip' at the sphere's surface and proposed a simple form of slip correction factor C(Kn) for Stokes law known as the 'Cunningham correction factor'. The expression for C(Kn) is as follows –

$$C(Kn)=1+A'Kn \tag{1.12}$$

Where, Kn is the Knudsen number of the sphere and A' is a constant. Equation (1.12) is thus altered as follows –

$$F_D=-\frac{6\pi\mu Rv}{C(Kn)}=\frac{6\pi\mu Rv}{1+A'Kn} \tag{1.13}$$

The coefficient 'A' in the above expressions depends on the way the molecules rebound from the surface of the sphere for either large or small values of Kn. The drag forces depend on the nature of the collisions between the particles and air molecules. The Cunningham factor always reduces the Stokes drag force. Using this correction application of Stokes law can be extended to the particle sizes comparable to or less than the mean free path of the gas molecules (Kim et al., 2005).

For $0.25 < Kn < 100$, the following empirical interpolation formula for 'A'' was proposed by Knudsen and Weber.

$$A'=\alpha+\beta\, e^{\gamma/Kn} \tag{1.14}$$

Where α, β and γ are experimentally determined constants (refer Appendix II).

Brownian diffusion

Brownian motion is an intricate and erratic motion which is conceded when a small particle (size of > 1 μm) is submerged in a carrying phase (fluid or gas) as a result of the collisions it goes through with the molecules of carrying phase (Einstein, 1905).

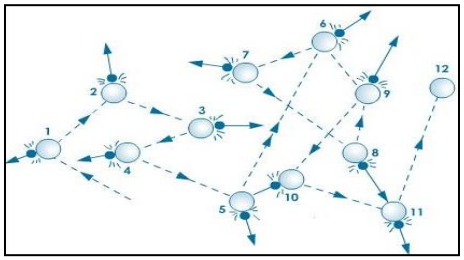

Figure 1.6 –A random movement of particle in all directions (Brownian motion)

The Brownian force is modelled as a white noise Gaussian random process. In a continuum framework, this is accounted with the introduction of a fictitious Brownian force to the particle equation of motion (Li & Ahmadi, 1992). Moreover, according to Chandrasekhar, the motion of a Brownian particle can be regarded as one of random flights. Hence this motion can be described as one of diffusion and is governed by the 'diffusion equation' (Chandrasekhar, 1943). Thus, while simulating the Brownian deposition of particles in a single monolith channel, a simple 'convection-diffusion' simulation of the species (species transport) involved would provide an accurate estimate of the deposition efficiency. The diffusion equation predicts the change in concentration of a diffusing mass over time at a point. This equation can be derived using the law of conservation of mass (Equation (1.15)).

$$\frac{\partial M}{\partial t} = \sum m_{in} - \sum m_{out} \tag{1.15}$$

The mass diffusing in and out are individually summed over a chosen control volume (CV), with the diffusive mass fluxes in and out of the CV computed using the Fick's law of diffusion.

$$q_i = -D_{ab}\frac{\partial C}{\partial x_i} \tag{1.16}$$

Where, C is the concentration of the species and D_{ab} is the diffusivity. After substitution of the concentration C and net fluxes m in the x, y and z directions in the CV and some mathematical treatment the general three-dimensional diffusion equation of the form below is obtained –

$$\frac{\partial C}{\partial t} = D_{ab}\left(\frac{\partial^2 C}{\partial x^2} + \frac{\partial^2 C}{\partial y^2} + \frac{\partial^2 C}{\partial z^2}\right) \tag{1.17}$$

The equation (1.17) is modified further to form the convection-diffusion equation as presented below.

$$\frac{\partial}{\partial x_i}(\rho Y_i)+\nabla.(\rho\vec{v}Y_i)=-\nabla.(\vec{J_i})+R_i+S_i \quad (1.18)$$

Where R_i is the net rate of production of species 'i' by chemical reaction and S_i is the rate of creation by addition from the dispersed phase plus. An equation of this form will be solved for N-1 species where N is the total number of fluid phase chemical species present in the system, $\mathbf{J_i}$ is the diffusion flux of species 'i', which arises due to gradients of concentration.

Theoretical capture efficiency in a single channel

In most industrial applications concerning deposition of small aerosol particles on surfaces, such as particulate matter capture in open substrates, considerations of both turbulent dispersion and Brownian diffusion are required. However due to the laminar flow conditions prevalent in the work described here, deposition due to Brownian forces are the principal mechanism of deposition (assuming uniform temperature gradients within the channel and thereby neglecting thermophoretic effects) (Ounis, Ahmadi, & McLaughlin, 1991)From a hydrodynamic and mass transfer standpoint, the substrate channels are short relative to their cross-sectional dimension, hence using the appropriate correlations for the Sherwood (Sh) and Schmidt (Sc) numbers, the deposition efficiency ($CE_{channel}$) due to Brownian diffusion (described in the previous section) can be found using the simple exponential equation (1.19). This equation is applicable when the concentration near the surface is equal to zero (Johnson & Kittelson, 1996).

$$CE_{channel} = 1-\exp\left(\frac{-h_m A_s}{Q}\right) \quad (1.19)$$

Where A_s is the surface area of the channel, Q is the volumetric flow rate through channel and h_m is the average mass transfer coefficient of the channel calculated as –

$$h_m = \frac{D_{ab} Sh}{d_{ch}} \quad (1.20)$$

Where D_{ab} is the (size dependent) particle diffusivity, d_{ch} is the monolith channel hydraulic diameter and Sh is the Sherwood number based on the channel diameter. The Sherwood number is given using the semi-analytical equation for the average Sherwood number in square channels using Equation (1.17) (Hawthorn, 1974).

$$Sh=2.98\left(1+0.095ReSc\frac{d_h}{L_c}\right)^{0.45} \quad (1.21)$$

Here, Re is the channel Reynolds number which is a dimensionless number and is defined as the ratio of inertia forces to viscous forces ($Re = \rho d_h u_c/\mu$), where ρ the gas phase density and μ is the gas phase viscosity, and Sc is the Schmidt number ($Sc = \mu/\rho D_{ab}$), where D_{ab} is the species dependent diffusivity of particles moving with Brownian motion (the intensity (energy and freedom of motion) of these Brownian motions controls the value of D_{ab}), d_h and L_c are the

channel hydraulic diameter and length respectively. D_{ab} is estimated using the following expression –

$$D_{ab} = \frac{k_b T}{F_D} \tag{1.22}$$

Where, k_b is the Boltzmann constant ($1.38e^{-23}$ m^2 kg s^{-2} K^{-1}), T is the channel temperature, F_D is the drag acting on the particle (Equation (1.11)).

The subsequent sections would describe the experimental trials performed along with the simulation set up in details. These would be followed by the results of this work.

2 Experimental set-up

2.1 Related apparatus

The experimental part includes several key apparatus such as-

- TOPAS-ATM230 (Aerosol generator)
- DMS500 (fast particulate spectrometer)
- EATS rig (emission after treatment system)

A very brief description of these devices and their applications is described in the following sections. This would provide better understanding of the experimental results and discussions.

2.1.1 TOPAS-ATM230

The aerosol generator ATM 230, manufactured by TOPAS Gmbh, is a device purposed to produce aerosols with highly constant particle size distribution and high reproducibility with known properties. A schematic of The ATM 230 and its mechanism is illustrated in the Figure 2.1 below-

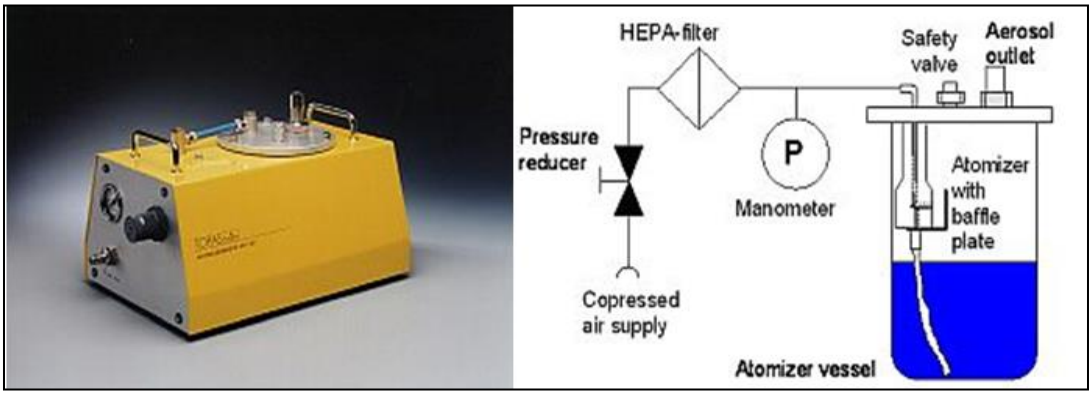

Figure 2.1 - Schematic illustration of the standard ATM 230 design (Figure adapted from TOPAS Gmbh ATM-230 Instruction manual)

Compressed air (not more than 8 bar) is fed into the machine from the front panel and creates its operating pressure. The production rate can be adjusted in a wide range by changing the operating pressure (which can be regulated by a pressure reducer at the front panel).This operating pressure is measured by a manometer. The internal HEPA filter removes impurities from compressed air before entering the atomizer nozzle. The atomizer vessel is filled up to a maximum 500 ml with liquid solutions and is capped. The aerosol outlet, a safety valve and an atomizer which is connected to compressed air are mounted on the cap. The heart of the ATM 230 is its stainless steel atomizer which operates as a two-stream nozzle based injection system with a baffle plate attached closed to the spray outlet. The coarse droplets with higher inertia fall down into the solution and the smaller ones with lower inertia flow up and form a layer of mist just under the cap and enter the aerosol outlet. The recirculation ratio has been calculated as 300 (the calculation of the recirculation time is presented in Appendix III). The maximum aerosol flow rate produced from this aerosol generator depends on the nozzle size and operating pressure. A smaller injector hole can be utilized for low pressure-high flow output conditions for

e.g. a nozzle size of 1.1 mm and upstream pressure of 1 bar produces a volumetric flow rate of 13 LPM and a nozzle size of 1.3 mm at a pressure of 4 bar results in a flow of 16 LPM (For more details refer to Appendix III).

2.1.2 DMS500

The DMS500 fast particle analyser (manufactured by CAMBUSTION) provides the fastest time response ($T_{10\text{-}90\%}$ 200ms) available for real-time measurement of the particulate size range from 5nm to 2500nm. It is widely used for gasoline and diesel engine development, aerosol science research and ambient aerosol monitoring. A schematic of the DMS500 is illustrated in the Figure 2.2 below-

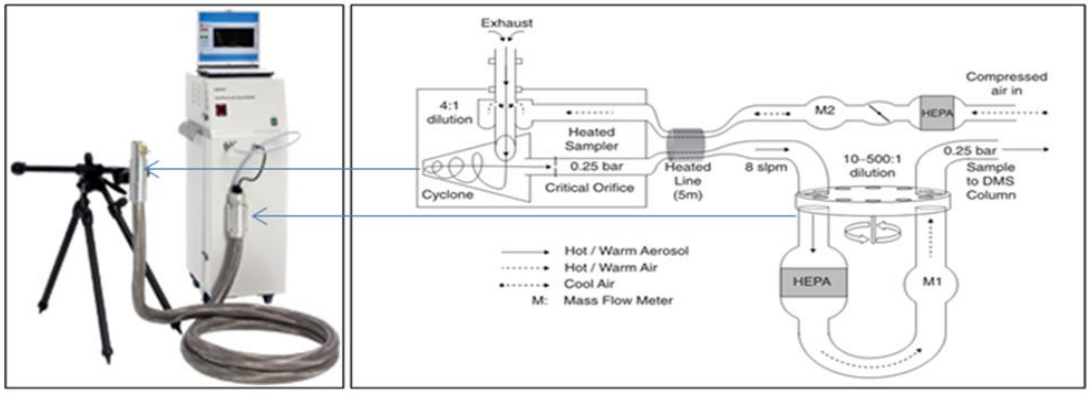

Figure 2.2-DMS500 CAMBUSTION (a). Mechanism of the attached tube (1st and 2nd dilution) is illustrated (b) (Figure adapted from Symonds(2013))

The sampling pipe in the DMS500 system integrates two stages of dilution which is illustrated in the Figure 2.2 above. The 1st dilution stage which occurs at the inlet part of the DMS tube, utilizes compressed air to provide low dilution ratio. This is done in order to reduce the dew point of sampling gas and avoid condensation (prevent damage). Nevertheless, different sampling gases require different dilution ratios for e.g. raw exhaust sampling gas normally requires a ratio of 4:1.Also, there is a cyclone to remove the large particles (>1 µm) from the sampling flow. A restrictor (an orifice) is placed after the cyclone which is to maintain a flow rate of approximately 8 LPM (standard LPM) in the sampling line. Moreover, the sampling pipe temperature is maintained at 75°C (in accordance with the instructions from the manufacturer). In the 2nd stage, however, a rotating disc creates different dilution ratios. This is done to minimise the cleaning requirement and maintain a good signal for the instrument. The dilution ratio could be varied (12-500:1) and adjusted to the value that provides and maintains a good signal.

2.1.3 The EATS (emission after treatment system)

The EATS (emission after treatment system) is responsible to create systematic variation of the emissions with respect to residence time, temperature and gas phase compositions by using different set-ups e.g. adding air (upstream dilution) or different types of substrate (monolithic catalysts). A schematic of the EATS is illustrated in the Figure 2.3.

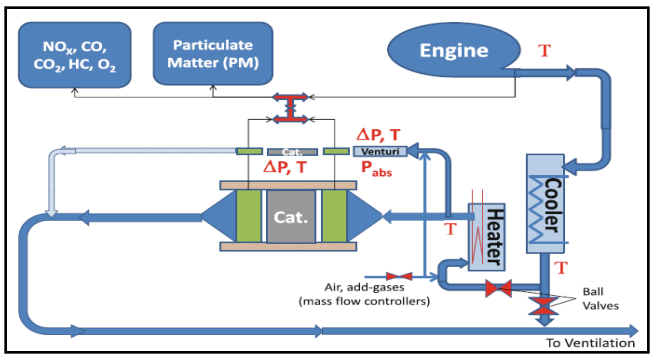

Figure 2.3-A schematic picture of the EATS [Figure adapted from Sjöblom, J (2013)]

The EATS consists of a cooler (if cooling is needed), a heater (to provide different upstream temperature and also avoid condensation of cooled exhaust gases), three mass flow controllers (to measure and regulate the flow in the system) and a catalyst section. The system communication is controlled by a Lab view system. All relevant conditions e.g. absolute and differential pressures, pressure in the switching system, gas flows from mass flow controllers and temperature from temperature sensors placed at different positions (positions were assessed by CFD calculations) for both catalyst and pipes are logged in a log file for post-processing. However, in the current set up, inlet flow to the EATS is a mixture of sodium chloride (solid particles,) water vapour and air (exhaust is not used), therefore the EATS has been slightly modified as shown in the Figure 2.4 below -

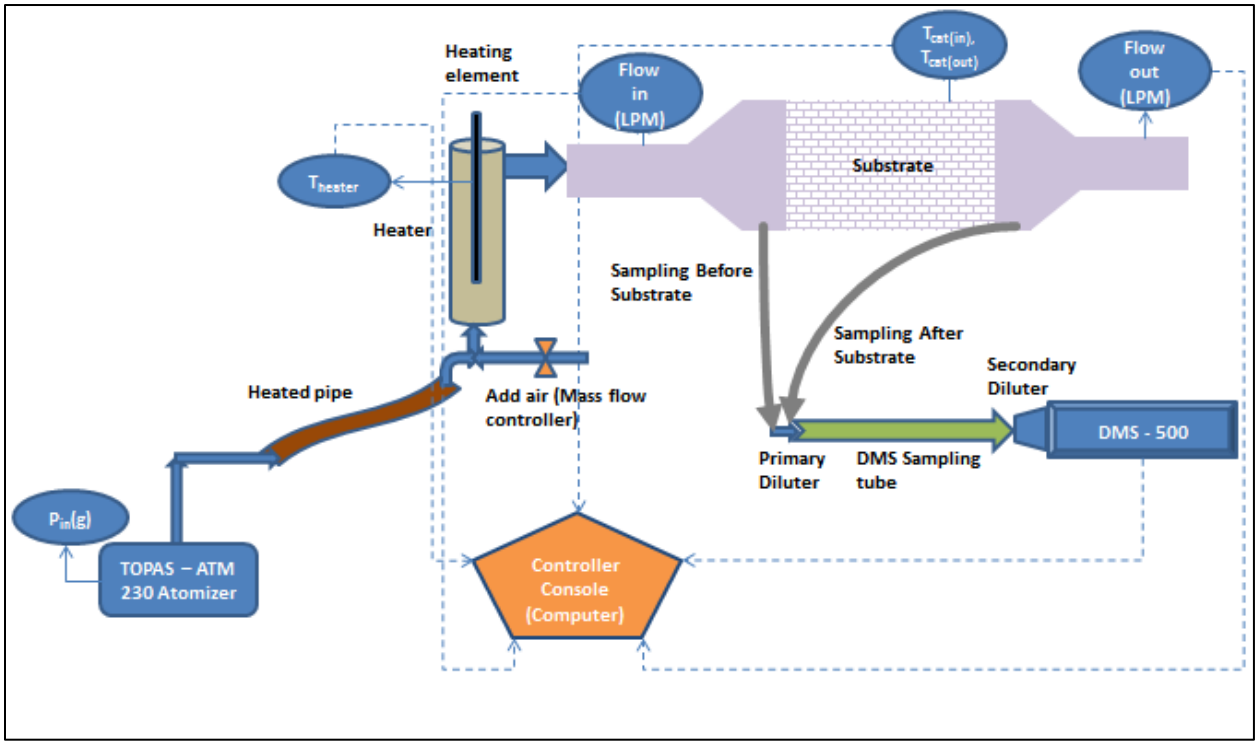

Figure 2.4-The modified EATS (Emission after treatment system)

In the current modified EATS, the cooler has been eliminated since cooling of the inlet flow is not needed, therefore, to prevent further pressure and particle losses the inlet flow is directly connected to the heater. In addition, only inactive and uncoated substrates were placed in the EATS. This was done to minimize the effect of disturbing phenomena that could occur in the presence of a chemically active catalyst and would result extreme complexity. The monolith geometry has been described in detail in the later sections (section 3.2.1)

2.2 Initial trials

Several initial trials were performed in order to establish some principal procedural tenets for particle generation using the TOPAS – ATM230 atomizer. However, this atomizer is capable of generating droplet aerosols and not solid particles. Therefore, sodium chloride (NaCl) droplet aerosols were generated from their aqueous solutions first and then these droplets were heated to produce solid particles. The desired particle sizes in the range of 10-150 nm were chosen in order to draw close parallelisms with actual diesel particulate matter emitted from engine exhaust.

The sodium chloride solution concentrations used in the atomizer were determined using the instructions provided by the manufacturer (TOPAS–Gmbh). Standard particle size measures were provided with the corresponding solution concentration. This data was empirically derived, and was used to make the initial estimates (refer Appendix IV). Based on this data five different concentrations of the salt were chosen –

- 10 ppm
- 100 ppm
- 5000ppm
- 10000 ppm
- 15000ppm

2.2.1 Preparation of salt solutions

The salt solutions were prepared based on weight % estimates. For instance, to make the 10 ppm solution, 0.001 g of NaCl (Sigma Aldrich -lab grade salt - 99% pure) was dissolved in 1 litre of distilled water. In a similar manner, the 100 and 10000 ppm solutions were made by dissolving, 0.01g and 1 g of NaCl in 1 litre distilled water respectively. The solutions were prepared prior to the execution of each experimental trial in order to ensure that fresh stock was employed each time.

2.2.2 Preliminary trials and experimental design (1st and 2nd sets)

The first sets of experimental trials were performed in order to characterize the particle generation set-up. A schematic representation of the set-up employed is shown in Figure 2.5.

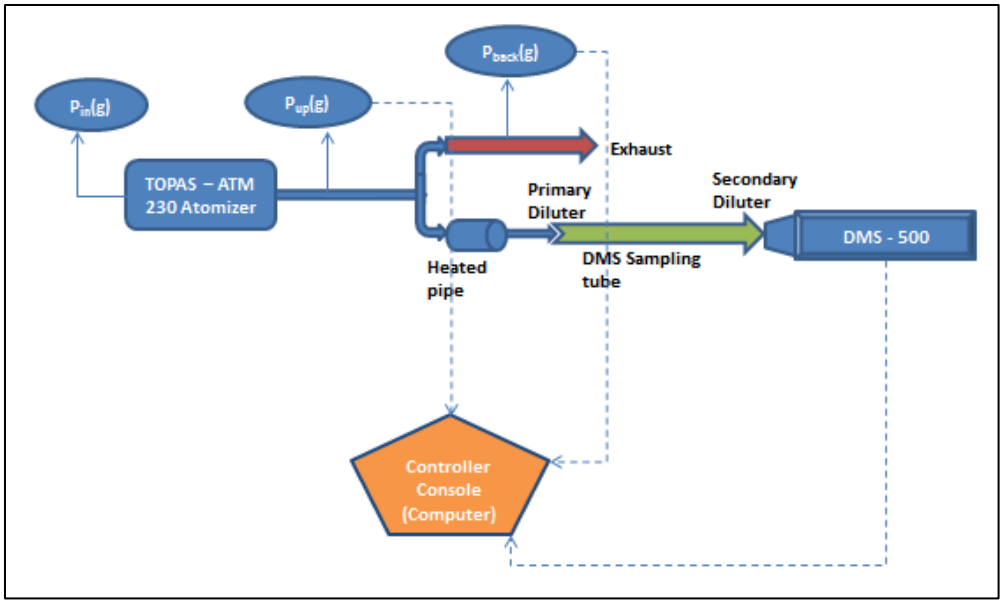

Figure 2.5 – A schematic picture of preliminary experimental set-up

The atomizer generates droplet aerosols (containing particles of size <1µm). In order to obtain solid particles, these droplets need to be evaporated completely. This is achieved by using a heated pipe (2m long). The temperature in this pipe is maintained at 190 °C. Such a high temperature would ensure that all the droplets produced would evaporate leaving behind the solid particles. Pressure sensors are mounted at the outlet of the atomizer (P_{up} (g)) in order to measure the pressure upstream. In addition there is also an inbuilt pressure gauge (P_{in} (g)) in the atomizer which records the pressure within the instrument (essentially P_{up} and P_{in} would measure the same pressure). The outlet from the atomizer is connected to a T-junction, where a part of the flow is sampled and the rest is directed towards an exhaust line. A pressure sensor is mounted in this exhaust line in order to measure the back pressure generated (P_{back} (g)). This back pressure was varied using tubes of different length. The sampled flow is first passed through the heated pipe and then finally enters the DMS – 500 via a sampling tube. The pressure sensors and the DMS-500 are controlled and monitored using a console.

The preliminary trials including two different sets of experiments (1^{st} & 2^{nd}) were performed in order to get some fundamental procedural insights into generating particles in a desired range using the aerosol generator. In the 1^{st} set of experiments, a viable 2-level experimental design gives critical information about the variables that could significantly affect the particle size distribution (PSD) and measurement process. In addition, this design would also help in identifying the appropriate levels of the variables in order to generate a desired particle size distribution. The variables and their corresponding levels (for the 1^{st} sets of experiments) chosen in order to generate such a 3-level design were as follows –

- Upstream Pressure (1 bar, 2 bar (centre point), 3 bar)
- Salt solution concentration (10 ppm, 100 ppm (centre point), 10000 ppm)
- Primary dilution (1X, 3X (centre point), 5X)
- Secondary dilution (Low signal (-1), Medium signal (0), High signal(1))
- Back pressure (Low backpressure (-1), High backpressure(1))

Clearly, a full factorial design for 5 variables at 3 levels would be implausible. A D-optimal design is thus chosen. A D-optimal design is a computer aided design which contains the best subset of all possible experiments. These designs are straight optimizations based on a chosen optimality criterion. The statistical software MODDE was used to generate the requisite D-optimal design of 49 experiments (see Appendix IVa for more details).

Based on the assessment of the data obtained from the first sets of experiments a second set of conclusive experimental trials were performed in order to finalize the particle generation procedure. The upstream pressure and the salt solution concentrations were identified as the most critical variables in the first sets of experiments. These were thus chosen as design factors again in order to optimize their levels. In addition, the heated pipe temperature (fixed to 190ºC repeatedly in the first sets of experiments), a new variable, whose affect was not investigated earlier was also chosen as a design factor. It was hypothesized that the heated pipe temperature would affect the drying time which would in turn affect the PSD. Thus the heated pipe temperature was included as a design factor in order to verify the above hypothesis. The design variables and their corresponding levels employed in order to generate a full factorial design (3^3 designs) were as follows –

- Upstream Pressure (1 bar, 2 bar and 3 bar)
- Salt solution concentration (5000ppm, 10000 ppm and15000 ppm)
- Heated pipe temperature (40,70 and 100ºC)

The design used in the second sets of experimental trials is a 3^3 full factorial design with centre points repeated (30 experiments) shown in Appendix IVb.

2.2.3 Particle size measurements

The particle size distribution measured by the DMS500 fast spectrometer are subject to some diffusion loss estimates.This is due to the fact that prior to the spectral measuremnet, the sample passes through a heated pipe, followed by the DMS samping pipe. The DMS sampling pipe, in addition, contains a primary diluter, that adds a specific amount of air based on a set dilution (based on chosen conditions) and secondary diluter ,just before the sample enters the DMS-500, which would in turn dilute the flow to a higher extent (The dilution is obtained by moving a small portion of the flow into the pockets of a rotating disc and not directly by air) .Thus it can be assumed that, the total number of particles leaving the atomizer are not being measured at their actual state, but are instead measured after some diffusion losses due to the flow through the tubes (heating pipe and sampling tube) and also due to the secondary diluter section. Moreover, in the measurements of the capture efficiency (fully discused in the next section), since measurements are different between samplings from two different positions (upstream and downstream of the substrate), if the sampling is done at different points then it is very imortant to consider the diffusion losses in order to draw valid conclusions.The diffusion loss calculations can be summarized in the expression below .

$$PSD_{measured} = PSD_{real} * PE_{tot} \quad (2.1)$$

Where the diffusion loss are calculated as-

$$DL_{diffusion\ losses} = 1 - PE_{tot} \quad (2.2)$$

A total "PE*tot*", known as the total penetration efficiency, is calculated for each experiment conducted as-

$$PE_{tot} = PE_{hp} * PE_{2nd\ dil} * PE_{DMS\_samp} \quad (2.3)$$

Where PE_{DMS_samp},$PE_{2nd\ dil}$ and PE_{hp} are the calculated penetration efficiencies for the DMS sampling pipe, secondary diluter and heated tube respectively.

The penetration efficiency for both the heated and the DMS sampling pipes are calculated as-

$$\frac{N_{out}}{N_{in}} = \exp\left(\frac{-4V_d L}{d_t \bar{U}}\right) \quad (2.4)$$

$$V_d = \frac{0.04\bar{U}}{\mathrm{Re}^{1/4}}\left(\frac{\rho_g D_p}{\mu}\right)^{2/3} \quad (2.5)$$

L is the pipe length, d_t is the pipe diameter, $\bar{U}$ is the average linear velocity, V_d is the deposition velocity, ρ_g is the gas density and μ is the dynamic viscosity. The expression for V_d has been evaluated by (Kumar, Fennell, Symonds, & Britter, 2008). The equation (2.5) is generally applicable for turbulent flows alone. However, experimental observations revealed that this equation can also be used at laminar flow conditions (Kumar et al., 2008).

The penetration efficiency for the secondary diluter was obtained by fitting parameters to CFD calculations (Sjöblom & Ström, 2013). The corresponding equation is as follows -

$$\alpha = \frac{b_1}{d_p^2}\left(1 + b_2 e^{-b_3 d_p}\right) \quad (2.6)$$

Where, A_W is the pocket wall area, V is the pocket volume, τ is the residence time in the pocket. The particle diffusivity (D_P) was then replaced by a size dependent vector (α) that takes into account both the effects of the specific geometry of the secondary diluter pockets and the effect of a varying bulk concentration as well as the effective diffusivity. b = [b1 b2 b3] = [1.71e-23; 1.05; 1.89e11] (Sjöblom & Ström, 2013). Therefore, it is possible to back calculate the real particle size distribution from equation (2.1).

2.2.4 The capture efficiency trials (3rd set)

In the final set of experiments, time-averaged capture efficiency of two different set ups (adiabatic and non-adiabatic) were evaluated. The reason for considering time-averaged capture efficiency was to ensure that steady state conditions prevail. This was achieved by taking samples before and after the substrate repeatedly by the use of pneumatic valves. In each case, samples were taken at three different temperatures (150, 200 and 250°C) and three different flow rates (150, 236 and 473 LPM at the existing conditions of temperature and pressure). Temperatures were monitored and maintained by the temperature sensors that were placed in different locations in the substrate. The positions of the temperature sensors were obtained from CFD calculations (These assessments are fully explained in the subsequent sections (Section 3)). The volumetric flow rates in the substrate were calculated using the pressure drop across the substrate (ΔP was measured using the pressure sensors placed along the substrate.) under

specific conditions. The volumetric flow rate increased due to increase in temperature by expansion (reduction of density). However, in order to fix the volumetric flow rate at a constant value (chosen initially –Refer Appendix XI), the inlet flow was reduced (via regulating ball valves at the EATS). The flow viscosity (μ) and density (ρ) (at the same conditions), are then substituted in the equation (2.7) below in order to calculate the channel velocity (*U*) (correlation given by (Ekström & Andersson, 2002)) -

$$\Delta P = \frac{28.4\mu UL}{dh} + \frac{0.42\rho U^2}{2} \qquad (2.7)$$

From the substrate specifications, the open flow area (OFA) of the substrate (about 0.0126 m^2) was obtained (the substrate size: 5.66" x 6", 400 cpsi. Using the OFA and the channel velocity (U) the volumetric flow rates across the substrate were calculated. (For more details refer Appendix V).These conditions were chosen so as to mimic engine exhaust conditions.

The capture efficiency trials were planned in the following manner -

***Case 0 (EATS temperature dependency study)*-**In this case, the EATS is run with just air (no particulate flow). The substrate area plus some part of its inlet section were insulated by glass wool (5 cm thickness). Furthermore, heat conduction rates for different flow conditions were calculated. The objective of this evaluation was to validate the CFD calculations of temperature gradients at different positions in the substrate.

Case A (adiabatic) **-** In the adiabatic set up, the substrate area plus some part of its inlet section were first covered by a heating tape and then insulated by glass wool (as shown in the Figure 2.6 below). This was done to compensate for the heat loss in the substrate area, thereby ensuring adiabatic conditions (all channels in the substrate had the same temperature). The particulate flow from the aerosol generator (ATM230) was first connected to a 2 m heated tube (at 190°C), and subsequently fed to the EATS via a T-junction attached at the beginning of the heater. This flow was then diluted by adding air. The sampling was done before and after the substrate at fixed positions using a mixed cup sampling probe. These samples were then fed into two 1 m heated pipes (positioned at before and after sections at 200°C). The sampling switching was achieved using tubes fitted with pneumatic valves that finally connected with the DMS sampling tube. The data points for this case are tabulated in the Appendix XI (Table 7.7)[1]

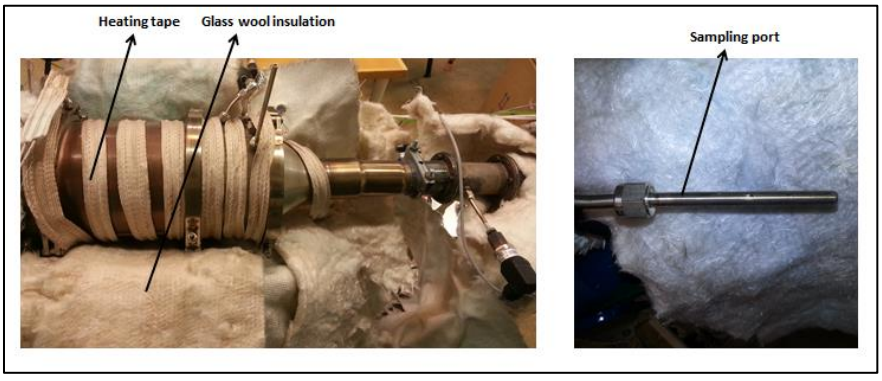

Figure 2.6 – Heating tape and insulation along the substrate (left), mixed cup sampling probe (right)

[1] All CE trials were done in triplicates

Case B (non-adiabatic)- In the non-adiabatic set up, the same procedures as in the adiabatic case were followed, but in this set up, the heating tape was switched off in order to establish non-adiabatic conditions (heat loss to the surroundings). Therefore, allowing temperature gradients to develop both in axial and radial directions in the substrate.

The time averaged capture efficiency (*CE*) is estimated by using PM measurements of the flow entering and leaving the substrate as-

$$CE_{time-averaged} = \frac{PSD_{before\_timeaveraged} - PSD_{after\_timeaveraged}}{PSD_{before\_timeaveraged}} \tag{2.8}$$

Where, $PSD_{before\_time\ averaged}$ and $PSD_{after\_timeaveraged}$ are the time-averaged particle size distributions upstream and downstream to the substrate respectively. Yet, to tackle time related disturbances within the system, one should calculate the uncertainty of the *CE*. In order to do this, the standard deviation must be estimated first. But, it was noted that direct calculation of the standard deviation is not possible due to the denominator (division by zero). Therefore, the expression for *CE* was reformulated as the product of two quantities, X and Y given as:

$$CE_{time\_averaged} = (PSD_{before\_timeaveraged} - PSD_{after\_timeaveraged}) * \frac{1}{PSD_{before\_timeaveraged}} = X * Y \tag{2.9}$$

$$X = (PSD_{before\_timeaveraged} - PSD_{after\_timeaveraged}) \text{ and } Y = \frac{1}{PSD_{before\_timeaveraged}} \tag{2.10}$$

Then the variance is calculated as_

$$\varepsilon = t_{N-1,96\%} \sqrt{X^2 \mathrm{var(Y)} + \mathrm{Y}^2 \mathrm{var(X)} + \mathrm{var(X)} * \mathrm{var(Y)}} \tag{2.11}$$

Where, $t_{N-1,96\%}$ is 1.96 (from Student's t statistic tables) and this variance has been shown as error bars on the $CEtime\_averaged$ curves.

2.3 Strategy adopted in this study

As mentioned earlier, experiments and simulations would be done in conjunction. This systematic approach would improve the quality of the experimental evaluation. The following iterative procedure had been proposed and was carried out in this study .

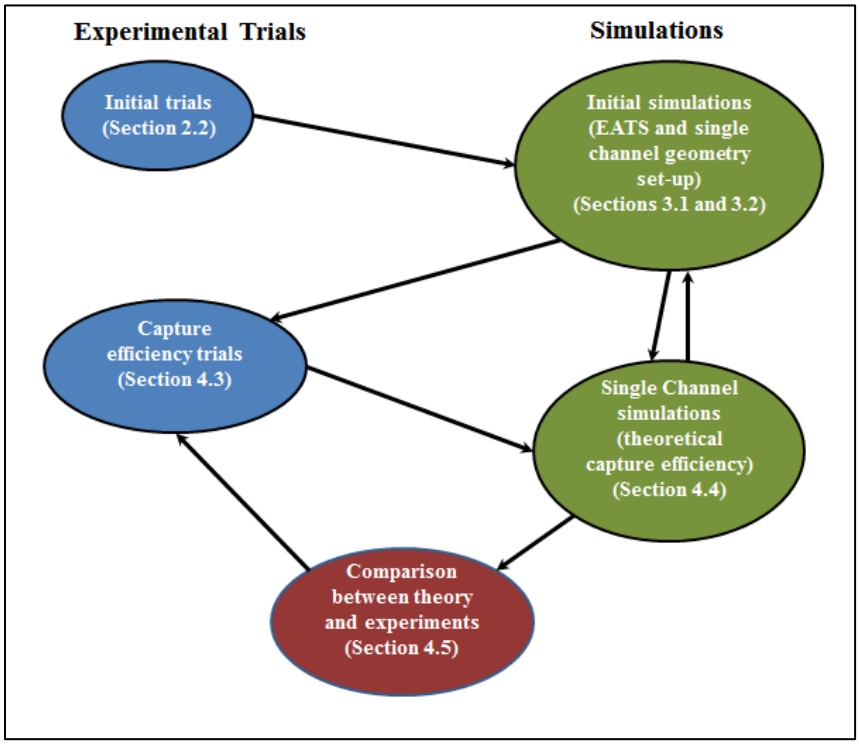

Figure 2.7 – Strategy to combine experimental trials and CFD assessment

This project was aimed at developing a methodology to combine experimental trials with CFD analysis in order to plan and perform better experiments. In the beginning, the generation of inert PM using the TOPAS ATM 230 atomizer was evaluated in order to establish a standardized methodology to produce PM of a desired size (10 -150 nm) and number concentration ($>10^4$ particles/cc). This was then followed by the initial simulations where the EATS and a single channel were set up and meshed. This was followed by some test simulations in the corresponding geometries under the chosen operating conditions. The EATS simulations were more extensively assessed in order to optimize and design the final capture efficiency trials (discussed extensively in sections 3.1 and 4.2). Based on the inputs from the initial simulations the final capture efficiency trials were planned and executed. Simultaneously, single channel simulations were run in order to predict theoretical capture efficiencies. The results from these simulations were compared with the experimental capture efficiency trials to observe if there were any congruencies between the two. In addition, if huge deviations are noted in these comparisons, the experiments and or simulations would have to be re-evaluated. Finally, if the trends match, these results are extrapolated to predict the CE of active PM evaporating in a channel.

3 Simulations

This section describes the schematic order in which the numerical experiments (simulations) have been carried out. As mentioned in the earlier sections, the aim of these simulations is to model theoretical as well as experimental conditions (EATS operating conditions) in order to supplement experimental findings. The simulations have been accomplished at two specific geometric scales, i.e.

- The entire EATS geometry (from the outlet of the heater to the outlet of the catalyst)
- Single monolith channel

All the simulations have been done using the 'ANSYS Fluent 14.0' computational fluid dynamics package. The corresponding geometry, meshing and boundary conditions of the above mentioned cases would be described in the succeeding section.

3.1 EATS simulations

The first sets of simulations that were set up involved the entire EATS geometry. These simulations would help in determining the boundary conditions for the single channel cases as well as aid in selecting the most appropriate locations for the temperature sensors that would be used to control the EATS operating conditions. Since the flow in the vicinity of the substrate was of importance, only the sections of the EATS that would represent this flow sufficiently well were chosen. The chosen geometry thus contained the section of the EATS from the outlet of the heater to the outlet section of the EATS (the section just after the substrate). A more detailed account of this chosen geometry is provided in the section below.

3.1.1 EATS geometry

The geometry of the EATS can be subdivided into 4 major sub-sections, these are –

- Inlet section
- A flow straightener section
- Substrate
- Outlet section

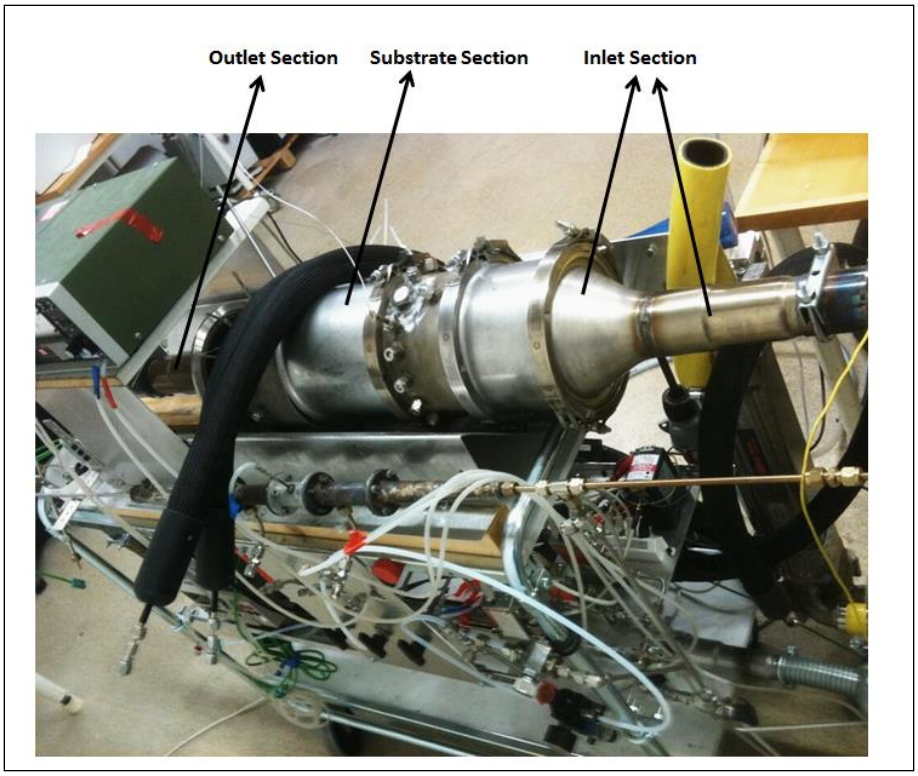

Figure 3.1 -The EATS

The inlet section consists of a steel pipe with a radius of 3.15 cm which expands into a larger section of radius 7.2 cm by means of a diverging skin. Just prior to this inlet section, is a mixing section with two stationary blades. This section would ensure a homogenous distribution (of flow and of the particles) at the inlet section. The inlet section is followed by a flow straightener section (about 14 cm long and of radius 7.2 cm). This section consists of evenly distributed channels each of hydraulic diameter ≈ 1.7 cm. This channelled section of the geometry would help in minimizing the changes due to sudden increase in flow area (recirculation and wake formations in the diverging section). The flow-straightener section can be completely detached as well. There is a short flow section of about 8 cm just before the substrate begins, the ultimate objective of having all these afore mentioned sections is to have uniform temperature and velocity profile at the inlet of the substrate. The substrate is about 15.24 cm long and has a radius of 7.2 cm. The outlet section is a mirror of the inlet section consisting of a pipe of radius 7.2 cm constricting into a pipe of radius 3.15 cm via a converging skin. Since, there is rotational symmetry, thus by modelling a cross-section about this axis of revolution, the entire EATS geometry can be simulated to a good degree of accuracy, using a 2D axis-symmetric solver. The above geometry was slightly modified as well in order to motivate the utilization of the flow straightener section. Hence, a second 2D axis-symmetric geometry, with the flow straightener section removed was also modelled. The final 2D axis-symmetric geometries (generated using 'Design modeller' in the ANSYS Workbench) which have been modelled are shown in figure 3.1.

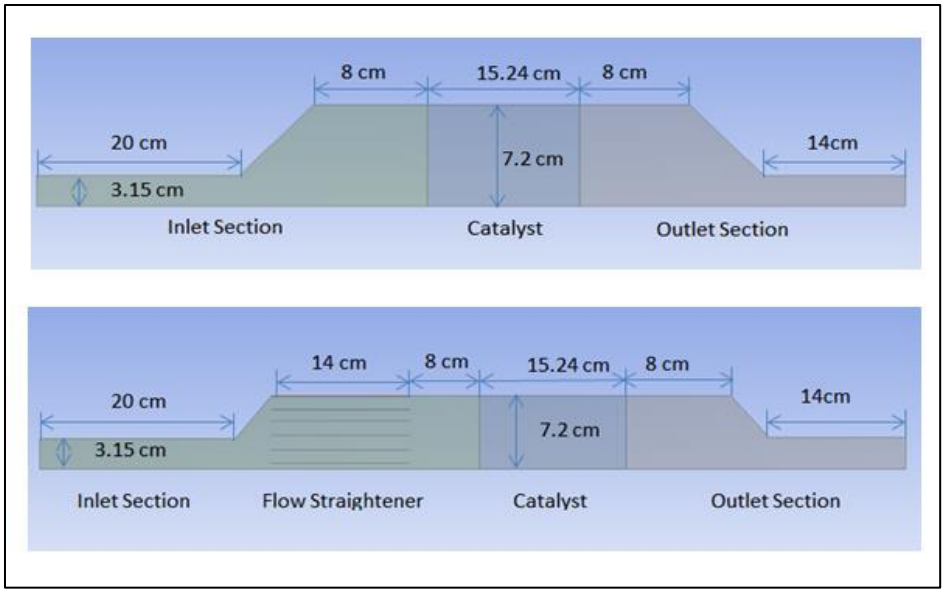

Figure 3.2 – 2D axis-symmetric geometry of the EATS without flow straightener section (top) and with flow straightener section (bottom).

3.1.2 EATS meshing

Mesh generation is one of the most critical aspects of an engineering simulation. Too many cells may result in long solver runs, and too few may lead to inaccurate results. Hence, extreme care was adopted while choosing the right mesh. The mesh for the above geometry was generated using the ANSYS in-built meshing software. First a coarse mesh was generated in the program (with a maximum computational cell face size of 8.63 mm). This mesh is further refined in 'ANSYS Fluent' using the '*Adapt region'* feature. (Refer Appendix VIIIa for mesh quality assessment studies)

3.1.3 Set-up and Boundary conditions

The boundary conditions were set based on some of the assumptions employed while modelling this system. The main assumptions utilized to model this system were –

- Symmetry along axes (2D-axis symmetric)
- Laminar flow ($Re_{inlet} \approx 650$) (Refer Appendix V)
- Monolith modelled as a porous zone
- 3 mm thick insulation at walls (k=0.93 (J/m^2-Kfor) for T = 150°C from material manufacturer)
- Stationary boundaries

The main objectives of the EATS simulations were to resolve the flow and temperature fields within the EATS under the experimental operating conditions. These operating points have been shown in Appendix XI (Table 7.6 and 7.7). The boundary conditions for a generic operating point are summarized in the table 3.1.

Table 3.1 – Generic boundary conditions for the EATS simulations

Velocity Inlet	
Inlet Velocity	Based on flow rates of ***150, 236 or 473 LPM (at the corresponding conditions of T and P)***
Temperature	***150, 200 or 250°C***
Pressure across monolith	***≈ 18.5 Pa, 28.5 Pa or 57 Pa***
Pressure outlet	
Stationary wall	

Three specific cases were studied in these simulations. These are –

- EATS under adiabatic conditions (at temperatures 150, 200 and 250°C and flow rates of 150, 236 and 473 LPM)
- EATS under non-adiabatic conditions with insulation (at temperatures 150, 200 and 250°C and flow rates of 150, 236 and 473 LPM)
- EATS under non-adiabatic conditions without insulation (at temperature 250°C and flow rate of 150 LPM)

For the adiabatic cases, the wall boundaries were set with zero heat flux (no heat loss in the system). In order to model the cases with and without insulation, a wall heat transfer coefficient is calculated based on natural convection of heat through a thin air film. This heat transfer coefficient was then set as the wall boundary condition. Only one case was simulated for the EATS without insulation, i.e. at a temperature of 250°C and a flow rate of 150 LPM, as this would represent the worst possible operating conditions for the EATS (maximum heat losses).

Porous zone model of the monolith

The monolith is represented with the continuum-equivalent method (porous brick/zone). The porous media model incorporates an empirically determined flow resistance in the region of the model defined as "porous". In essence, the porous media model adds a momentum sink in the governing momentum equations (refer to equation (1.2)). This source term is composed of two parts (see Equation (3.1) below): a viscous loss term (Darcy's resistance, the first term on the right-hand side of Equation (3.1), and an inertial loss term (the second term on the right-hand side of Equation (3.1)) (Gray & O'Neill, 1976).

$$S_i = \sum_{j=1}^{3} D_{ij} \mu \mathbf{v_j} + \sum_{j=1}^{3} C_{ij} \frac{1}{2} \rho |\mathbf{v}| \mathbf{v_j} \qquad (3.1)$$

Where S_i is the source term for the i^{th} (x, y, or z) momentum equation $|\boldsymbol{v}|$ is the magnitude of the velocity and D and C are prescribed matrices based on empirical relations. This momentum sink contributes to the pressure gradient in the porous cell, creating a pressure drop that is proportional to the fluid velocity (or velocity squared) in the cell. For a simple homogenous porous media, equation (3.1) can be simplified as follows –

$$S_i = \sum_{j=1}^{3} \frac{\mu}{\alpha} v_i + \sum_{j=1}^{3} C_2 \frac{1}{2} \rho |v| \mathbf{v_i} \qquad (3.2)$$

Where α is the permeability and C_2 is the viscous resistance factor. The operating monolith pressures are obtained by manually adjusting this inertial resistance factor. Typical values of C_2 along with the corresponding monolith pressure drops are listed in Appendix VI.

3.2 Single channel simulations

The single channel simulations are set up with the sole objective of modelling theoretical capture of particles in an open substrate. As elucidated earlier, the primary mechanism for particle (size range 4 nm to 250 nm) deposition in the monolith channel is Brownian deposition and hence 'Convection-Diffusion' simulation of the different particles would represent the theoretical capture efficiency of the substrate. The geometry, mesh and the boundary conditions of this simulation are described in the following sections.

3.2.1 Channel geometry

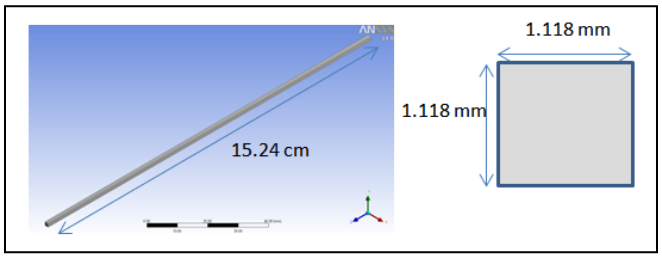

Figure 3.3 - 3D Square monolith channel (right) and Inlet cross-section of channel (right)

A simple square monolith channel of dimensions 1.118 mm X 1.118 mm and length 15.24 cm has been modelled (standard dimensions for a 400/6 monolith channel). A schematic of the geometry employed in these simulations (obtained using ANSYS Design modeller) is shown in figure 3.3 above.

3.2.2 Single channel meshing

The mesh for the above geometry was generated using the ANSYS in-built meshing software. First a coarse mesh was generated in the program (with a maximum computational cell face size of 7.03 mm). This mesh is further refined in 'ANSYS Fluent' using the '*Adapt region'* feature. An additional 'wall refining' operation is also carried out on this mesh in order to resolve the near wall region (where steeper gradients are noticed) accurately. The refining is successively

done till a mesh independent solution is obtained. (Refer Appendix VIIIb for mesh quality assessment studies)

3.2.3 Channel Set-up and Boundary conditions (Theoretical capture efficiency)

The boundary conditions were set based on some of the assumptions employed while modelling this system. The main assumptions utilized to model this system were –

- Laminar flow ($Re_{inlet} \approx 1000$) (Refer Appendix V)
- Particle deposition in channel only due to Brownian effects
- The gas phase properties are modelled as air (with same properties)
- Stationary boundaries
- Zero concentration at the walls (for all particles)
- Ideal gas behaviour

As mentioned earlier, the main objectives of the channel simulations were to obtain the theoretical capture efficiency for the substrate under the experimental EATS operating conditions (Appendix XI Table 7.6 and 7.7). 27 different particle sizes are chosen (based on the capabilities of the experimental PSD measurements of the DMS-500) in order to provide similar operating points for comparing experimental results with results from simulation. The 'species transport' mode within the 'ANSYS Fluent solver' is activated in order to solve the diffusion equation for the different particles.

The size dependent mass diffusivity for the particles (Equation (1.18) based on Brownian deposition under rarefied flow conditions) is coded into a user defined function (UDF's) written and compiled in Visual C (refer Appendix 6.7 for UDF snippet). This UDF (*DEFINE_DIFFUSIVITY*) is then hooked to the 'ANSYS Fluent solver', which would then use the appropriate mass diffusivities (based on the particle size) in order to solve the 'Convection-diffusion' equation (eq.(1.22)) and yield the corresponding theoretical capture efficiencies. The inlet mass fraction for each of the chosen species is arbitrarily set to 0.01. The final theoretical capture efficiency is obtained using the 'mass weighted average' of the 'mass fraction' of a species at the inlet and outlet of the channel. This expression for CE is given in equation (3.3) below.

$$CE_{theoretical} = \frac{(\text{Mass fraction})_{in} - (\text{Mass fraction})_{out}}{(\text{Mass fraction})_{in}} \tag{3.3}$$

Equation (3.3) corresponds to number based capture efficiency since only a single particle of size 28 nm was considered initially.

The boundary conditions for a generic case are summarized in the Table 3.2 below.

Table 3.2 – Generic boundary conditions for the channel simulations

Velocity Inlet	
Inlet Velocity	***0.2 m/s, 0.3m/s or 0.6 m/s***
Temperature	***150, 200 or 250°C***
Mass fraction of species at walls	***0***
Mass fraction of each species at inlet	***0.01***
Pressure outlet	
Stationary wall	

The specific cases and their corresponding sub-cases that were studied in these simulations are described below.

- Channel under adiabatic conditions (at temperatures 150, 200 and 250°C and flow rates of 150, 236 and 473 LPM)
- Channel under non-adiabatic conditions with insulation (at a temperature of 250°C and a flow rate of 150 LPM)
    - *Case a* – Channel close to walls
    - *Case b* – Channel quarter way from the walls
    - *Case c* – Channel at the centre (half way from the walls)

- Channel under non-adiabatic conditions without insulation (at a temperature of 250°C and a flow rate of 150 LPM)
    - *Case a* – Channel close to walls
    - *Case b* – Channel quarter way from the walls
    - *Case c* – Channel at the centre (half way from the walls)

For the adiabatic cases, the wall boundaries were set with zero heat flux (no heat loss in the system). In order to model the non-adiabatic cases with and without insulation, an axial wall temperature profile is applied. This temperature profile is obtained for the corresponding cases from the 2-D axis-symmetric EATS simulations (for the experimental operating points Appendix XI – table 7.6 and 7.7). Using this profile, a linear wall temperature function (temperature as a function of z position) is generated (using the 'polyfit[2]' function in MATLAB). This function is then coded into a UDF (*DEFINE_PROFILE*). This UDF is then hooked to the 'ANSYS Fluent

[2] `polyfit'` finds the coefficients of a polynomial `p(x)` of degree '`n`' that fits the data, `p(x(i))` to `y(i)`, in a least squares sense.

solver', and the corresponding temperature profile is set for the wall boundaries (refer Appendix 6.7 for UDF snippet). All the boundary conditions for these simulations are set based on the experimental operating points (refer Appendix XI).

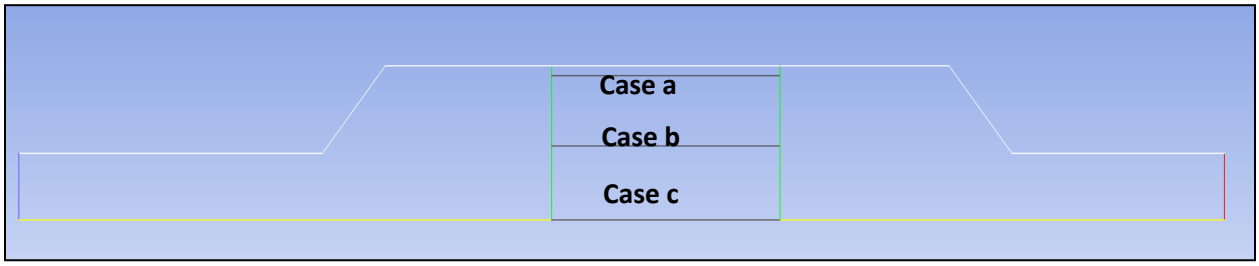

Figure 3.4 - Channel positions for the insulated and non-insulated cases

4 Results and discussion

4.1 Results of the initial trials (1st & 2nd sets)

4.1.1 Effect of concentration

The effect of concentration on particle size distribution for the 1st set of trials has been presented in the Figure 4.1 below.

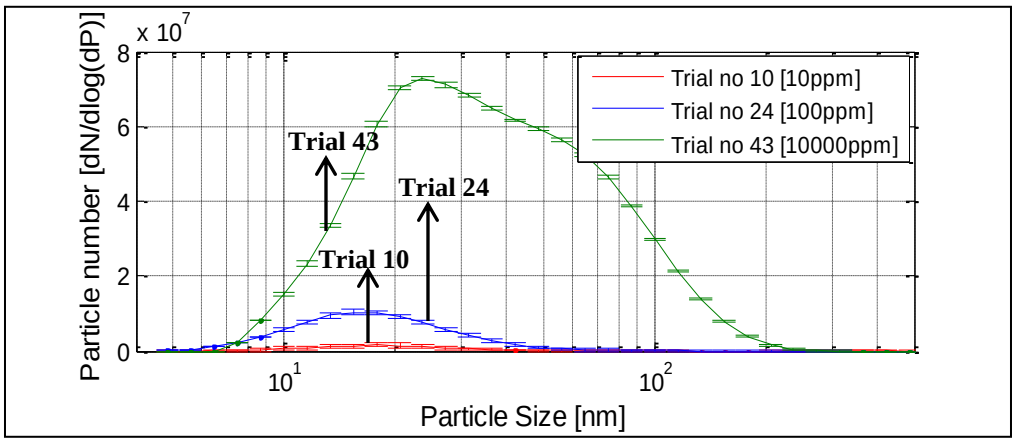

Figure 4.1 -The effect of concentration on PSD (1st set) at an upstream pressure of 3.5 bar

These specific trials (10, 24 and 43) from the 1st set of experiments have different concentrations (10, 100 and 10000 ppm of sodium chloride solution) while the other inspected variables like upstream pressure induced by the atomizer, dilution sets from the DMS and heating pipe temperature were all kept the same. From the figure above, it is very evident that higher concentration results in higher particle number concentrations (bigger area under the curve) with a broader particle size range. The same trend was also observed in the 2nd set of experiments for trials (23, 26 and 29 see Figure 4.2 below)

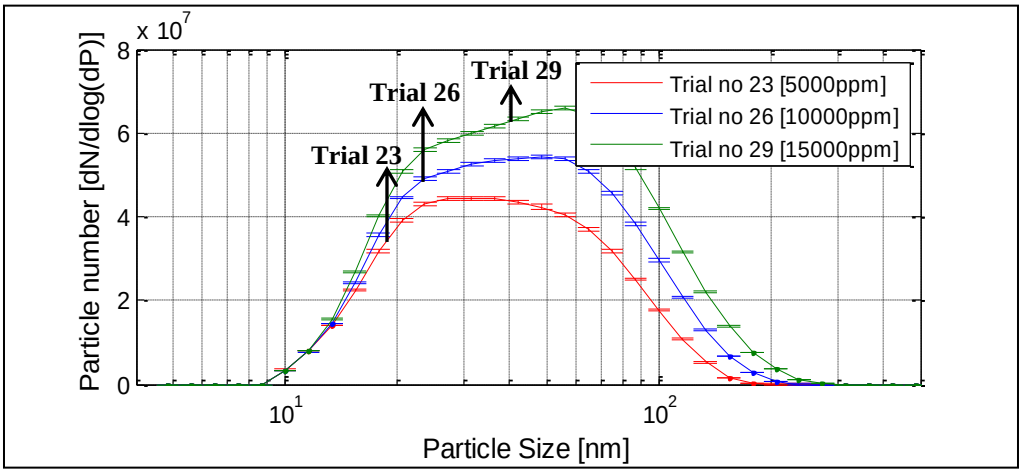

Figure 4.2 - The effect of concentration on PSD (2nd set) at an upstream pressure of 2.5 bar

4.1.2 Effect of the atomizer pressure (up-stream pressure) on PSD

Another important parameter that affected the particle size distribution was the pressure at the atomizer (P_{up}). As specified earlier (Section 2.1.1), higher atomizer pressure yields higher flow rates which results in higher particle number concentration. This is depicted in the Figure 4.3 below.

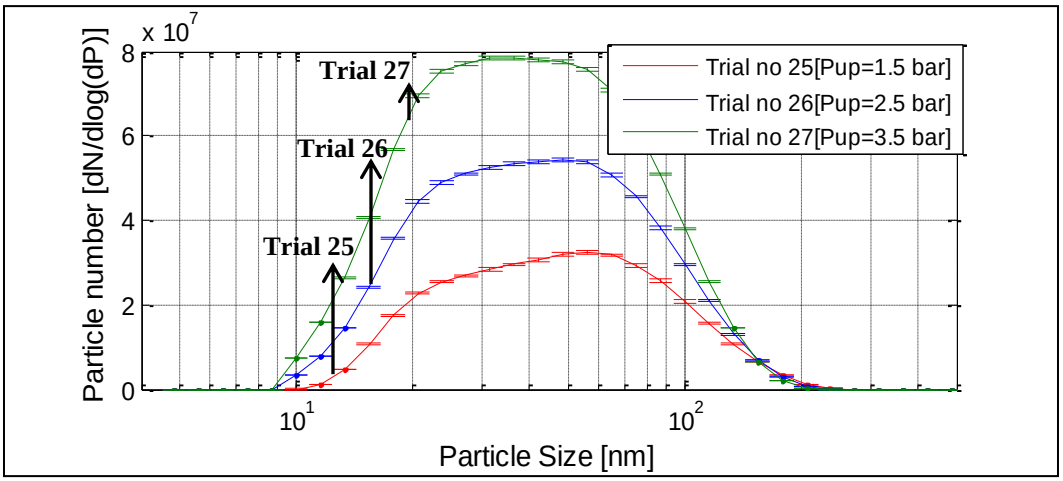

Figure 4.3 - The effect of atomizer pressure on PSD (2nd set) at a concentration of 10000ppm

These findings clearly indicate that higher concentrations and higher atomizer pressures yield particle size distribution (range from 10 to 150 nm) and particle number concentration of 10^7 which is suitable in this study.

However, based on the current experimental observations, solution concentrations of higher than 10000 ppm were noted to clog the restrictor in DMS pipe system. In addition, upstream pressure of more than 4 bar created severe instabilities in the atomizer. Thus, the concentration of 10000 ppm and P_{up} of 4 bar was chosen as the optimal condition to generate PM for the final sets of experiments (the capture efficiency evaluation).

4.1.3 Particle size measurement evaluation

The total number of particles leaving the atomizer are subject to some difusion losses due to their passage through several sections (heated pipe, DMS sampling tube and secondary diluter). In order to verify that the expressions employed in equation (2.3) account for the total diffusion losses, a comprehensive evaluation of the obtained data was carried out. The calculation results for PM diffusion losses in terms of penetration efficiencies for the heated pipe, DMS sampling tube and the secondary diluter at the DMS for a chosen trial (no 43) from the 1st sets of trials are presented in the Figure 4.4.

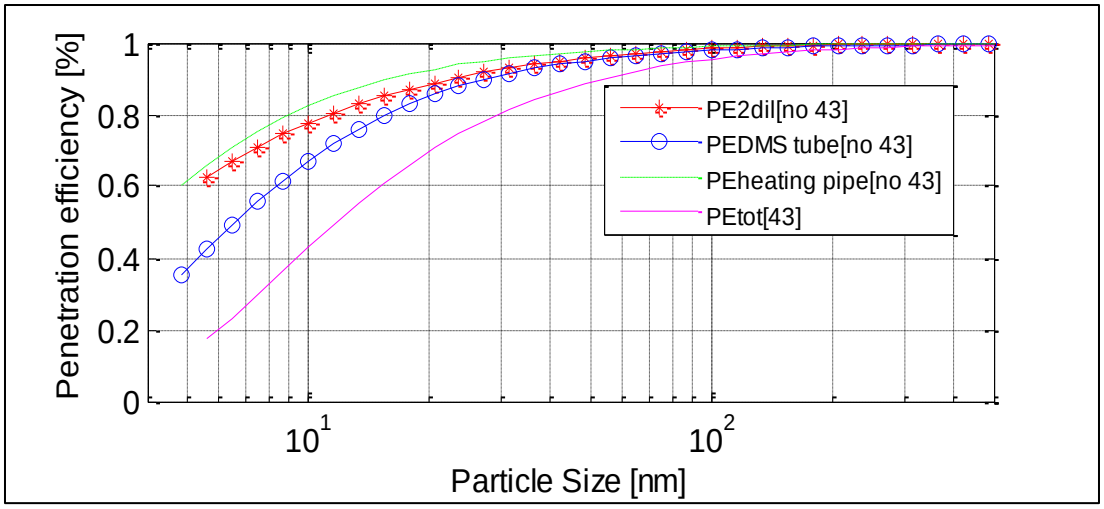

Figure 4.4 - Penetration efficiency for different sampling parts (sample pipes and 2nd dilutor)

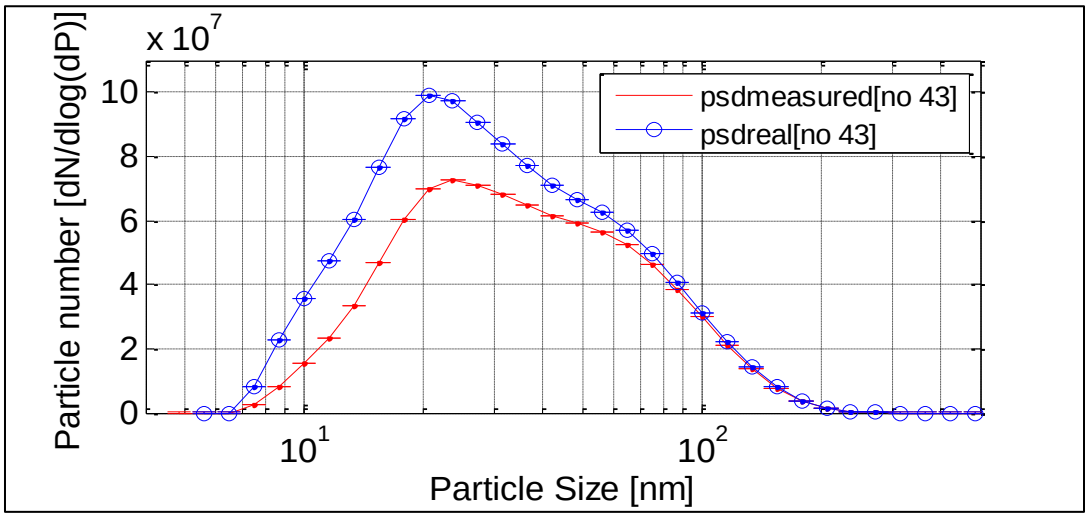

Figure 4.5 - Effect of diffusion losses

PSD_{real} is back-calculated and obtained from dividing the $PSD_{measured}$ by total penetration efficiency (equations (2.1), (2.2) and (2.3)). This result is presented in the Figure 4.5 above. In addition, it is very evident that the diffusion reduces with increase in particle size (Refer Figure 4.4 above) i.e. penetration efficiency increases. For instance, the diffusion loss for 100 nm particles is less than 0.5 % and that for particles larger than 30 nm is less than 20 %. Hence, it can be concluded that even with the inclusion of the afore-mentioned diffusion losses in the PM measurements, there would still be a significant number concentration of particles to draw valid conclusions ($>10^4$ particles/cc). In addition, as mentioned in earlier sections (Section 2.2.2) the diffusion loss calculations play a very essential role while calculating the capture efficiencies. However, since the sampling is done at two fixed points the losses are cancelled out[3].

[3] Note – Refer Appendix IVfor more details about the trials (conditions).

4.2 Results from the initial simulations

This section describes the relevant results that have been obtained from the several numerical analyses that were performed initially, i.e. the EATS and single channel simulations with preliminary set-ups. The results from the EATS geometry are described in detail in the following sections. It must be noted that, the results from the simulations is used to optimize the experimental trials and would thus have a significant bearing on their outcome.

4.2.1 Results from the EATS simulations

Studies on the flow field within the EATS under two different geometrical configurations (with and without the flow straighteners)

The effect of including the flow straightener in the EATS geometry was assessed. As explained in the earlier sections (Section 3.1.1), the flow straightener serves the primary objective of minimizing 're-circulation zone' effects. This would have an effect on the temperature profile within the geometry. The vectors of velocity magnitude for two particular non-adiabatic cases with insulation (250°C and 150 LPM - maximum heat losses) are compared in order to motivate the inclusion of a flow straightener in the EATS geometry. The case with the flow straightener would have hardly any recirculation effects (see figure below), thus there would be very poor mixing within the fluid streams at the inlet of the substrate leading to a higher axial temperature gradient along the EATS (412 to 523 K from the walls to the centre – refer figure 4.6 below) . The case without the flow straightener, however would have much better mixing of the air streams (due to recirculation) and would thus have a lower axial temperature gradient (503 to 523 K from the walls to the centre – refer figure 4.6 below). It is desired to have a temperature gradient as low as possible at the inlet of the substrate in order to obtain as close to adiabatic conditions within the substrate (which are the best operation conditions) as possible. Thus the flow straightener clearly does not permit such conditions (due to the higher temperature gradients it forms) and is hence removed from the EATS geometry.

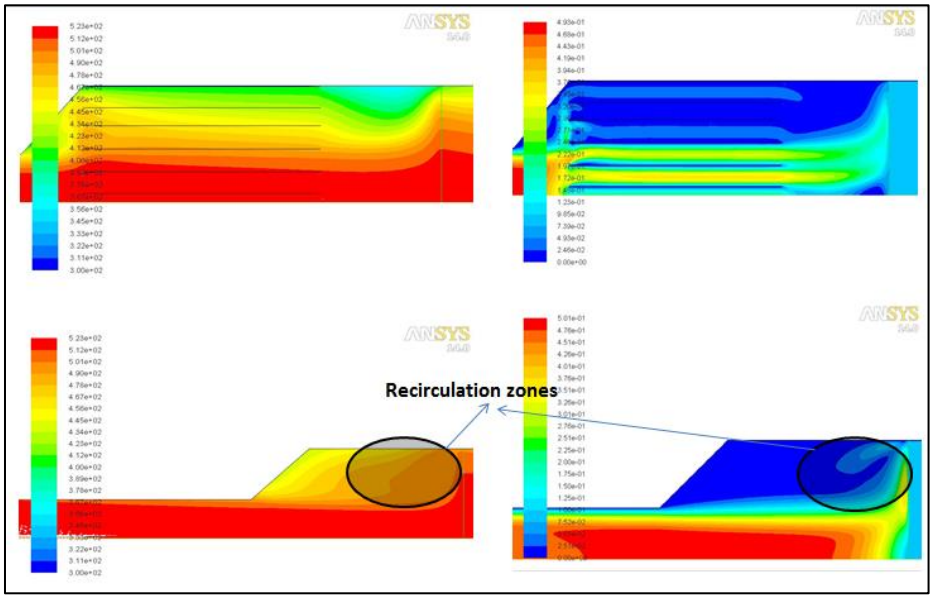

Figure 4.6 - Contours of temperature for the case with a flow straightener (Top-left), Contours of velocity for the case with a flow straightener (Top-right), Contours of temperature for the case without a flow straightener (Bottom-left) and Contours of velocity for the case without a flow straightener (Bottom-right)

4.2.2 Studies on the temperature profile within the EATS (without the flow straighteners)

The energy equation is solved in the 'ANSYS fluent solver' to give the requisite temperature distribution within the EATS. These solutions are obtained on the basis of the inlet and wall boundary conditions. These temperature profiles that were generated were utilized in order to determine the most appropriate locations for placing the thermocouples in the substrate. These thermocouples would provide real time temperature readings (while performing the capture efficiency studies on the EATS) and would thus aid in maintaining as close to adiabatic conditions as possible in the substrate (control the heater settings). In addition, as mentioned earlier (Section 2.2.4)), a heating tape has been used in order to maintain the adiabatic conditions within the substrate, the power to this tape would be controlled by a thermocouple which would detect the temperature within the system and accordingly supply heat or shut off. This thermocouple needs to be placed at the coldest possible region within the substrate (this is done so as to compensate for the higher heat losses in this region). The EATS temperature profiles generated from the CFD simulations were thus instrumental in determining the apt location to place this thermocouple as well. The temperature contour for the EATS operating under non-adiabatic conditions of 250°C and at a flow rate of 150 LPM, devoid of any insulation is shown in the figure 4.7 below. These conditions would represent the worst operating conditions for the EATS (maximum heat losses - due to higher temperatures and lower flow rates). An examination of this plot would provide a good insight into the appropriate thermocouple placement locations (Figure 4.7 below).

The Figure 4.7 below clearly indicates that, under these specific operating conditions, there is a huge temperature gradient across the substrate (as expected). There is also a significant radial temperature gradient (from the centre of the substrate to the walls) with the regions closest to the wall colder than the centre by about 160°C. This would mean that, the coldest zones within the substrate would be the regions closest to the walls. Thus the thermocouple controlling the heating tape would have to be placed in the vicinity of this region. The additional thermocouples which would provide real time information about the temperature within the substrates would have to be placed in the following key locations (shown in the Figure below) in order to have a measure of control over the adiabatic nature of the system.

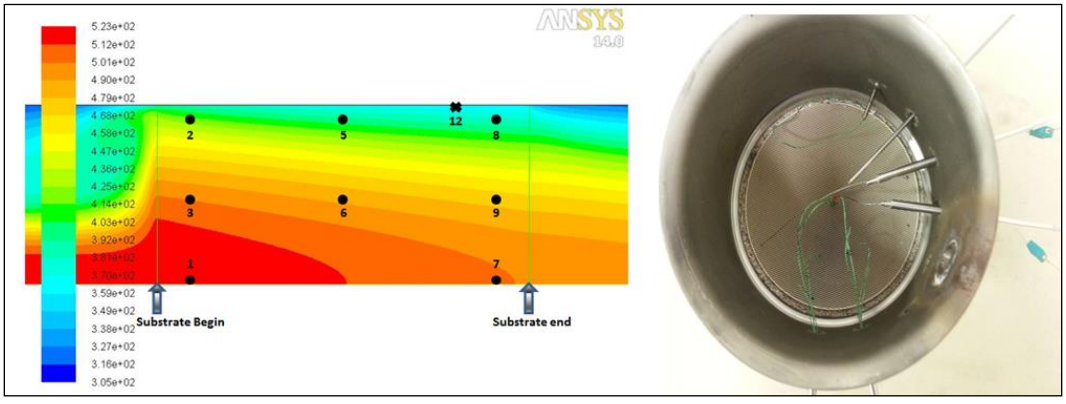

Figure 4.7 – Contours coloured by temperature (over the substrate) overlaid with a thermocouple map (based on a substrate at 250°C (at the point '*substrate begin*'), 473 LPM and No insulation)

Ten thermocouples were available in total, out of these; two were needed to monitor the heater outlet and the pre-substrate region respectively. The remaining 8 thermocouples were placed in the locations within the substrate as shown in the map above. Thermocouples 2, 3 and 1 were placed 2.5 cm away from the beginning of the substrate; thermocouples 5 and 6 were placed 7.5 cm away from the beginning of the substrate and thermocouples 7, 8 and 9 were placed 12.5 cm from away from the beginning of the substrate. The axial positions of the thermocouples are as follows – 2, 5 and 8 were placed 0.5 cm away from the wall; 3, 6 and 9 were placed 3.5 cm away from the walls and 1 and 7 were placed at the centre of the substrate (7.5 cm away from the walls). The thermocouple controlling the heating tape (12) was placed closed to the walls (near the insulation mat at the rear end of the substrate) so that it would compensate for the heat losses and accordingly regulate the power supplied to the heating tape. A photograph of the actual thermocouple placement within the substrate is also shown in the Figure 4.7.

The temperature profile within the catalyst at 250°C (523K) under two different flow rates (150 LPM and 473 LPM) was also assessed. The simulations clearly demonstrate the effect of increased flow rate on the temperature profile developed within the substrate (see figure 4.8 below). The shorter residence time (higher flow rate – 473 LPM) would mean that the fluid has lesser time to transfer heat to its surroundings (lesser heat losses). This would mean that there would be a lower temperature gradient developed within the substrate (as demonstrated in the figure below). The lower flow rate, on the other hand would mean that there would be higher heat loses from the flow (longer residence time) leading to a larger temperature gradient within the substrate. This fundamental concept of residence time and temperature gradient development in a non-adiabatic system would have a significant bearing on the capture efficiency of the substrate. The CFD simulations thus provide a very good insight into the overall flow conditions aiding in preparing and performing better experimental trials. (Refer Appendix IX for comparison between temperature profiles obtained in experiments and simulations)

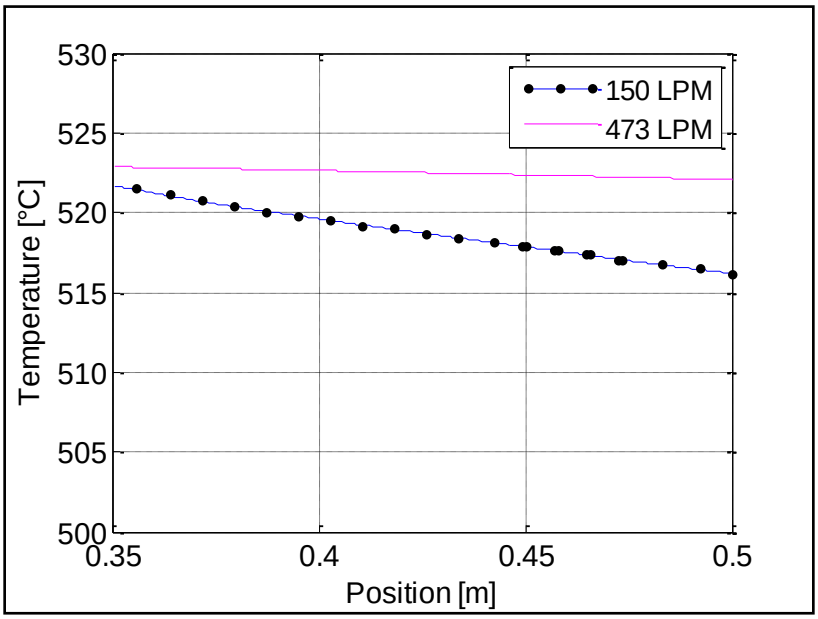

Figure 4.8 – Effect of flow rate on the temperature profile across the catalyst (at 250 °C)

4.3 Experimental CE trials

The effects of different experimental conditions on capture efficiency have been assessed and some specific cases are presented in the following sections (the rest are presented in the Appendix XII and XIII). Subsequently, these specific cases are compared to make the final conclusions. These cases are-

- ***Case A*** – Substrate under non-adiabatic conditions with insulation
  - *Case A1*-Effect of residence time at the highest temperature (150, 236 and 473 LPM at 250°C)
  - *Case A2* - Effect of temperature at the lowest flow rate (150, 200 and 250°C at 150 LPM)
- ***Case B*** – Substrate under adiabatic conditions
  - *Case B1* – Effect of residence time at the highest temperature (150, 236 and 473 LPM at 250°C)
  - *Case B2*– Effect of temperature at the lowest flow rate (150, 200 and 250°C at 266 LPM)
- ***Cases C***- The comparison between adiabatic and non-adiabatic capture efficiencies (case A & B)
  - *Case C1*- Both cases are assessed at the highest temperature of 250°C and lowest flow rate of 150 LPM
  - *Case C2* - Both cases are assessed at the lowest temperature of 150°C and highest flow rate of 473 LPM

4.3.1 Capture efficiency for the non-adiabatic conditions (Case A)

Effect of residence time (Case A1)

In this set of experiments, the inlet temperature at the substrate was fixed and maintained at 250°C. Three different volumetric flow rates of 150, 236 and 473 LPM were chosen to evaluate the effect of residence time on capture efficiency. The red, blue and black lines correspond to experiment number 20, 23 and 26 respectively.

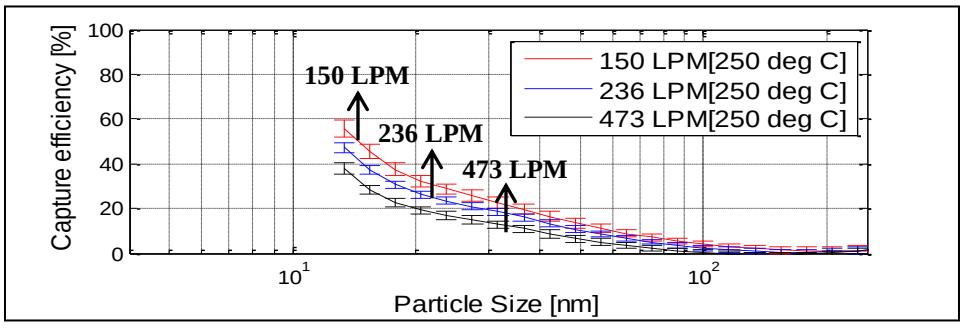

Figure 4.9 - Effect of residence time on capture efficiency at 250°C (Experiment no 20, 150 LPM, Channel Re = 5.61, Sh (at 27nm) = 8.06 and CE (at 27 nm) = 25.65 %), (Experiment no 23, 236 LPM, Channel Re = 8.11, Sh (at 27nm)=9.75 and CE (at 27 nm) = 21.27 %),(Experiment no 26, 473 LPM, Channel Re=15.13, Sh (at 27nm) = 13.09 and CE (at 27 nm) = 15.55 %)

From the Figure above (4.9), it is very evident that the capture efficiency increases with increase in residence time. The rate of increase in capture efficiency for a reduction in flow rate from 236

to 150 LPM is around 14.11% (for the particle size of 27nm) and that for a reduction from 473 to 236 LPM (an increase by 1.49) is around 26.89%.

Effect of temperature (Case A2)

In this set of experiments, the volumetric flow rate was fixed and maintained at 150 LPM. Three different inlet temperatures of 150, 200 and 250 °C were chosen in order to evaluate the effect of temperature on capture efficiency. The volumetric flow rate increased due to increase in temperature by expansion (reduction of density). However, in order to fix the volumetric flow rate at a constant value (chosen initially –Refer Appendix XI), the inlet flow was reduced (via regulating ball valves at the EATS). The red, blue and black lines correspond to experiment number 2, 10 and 19 respectively.

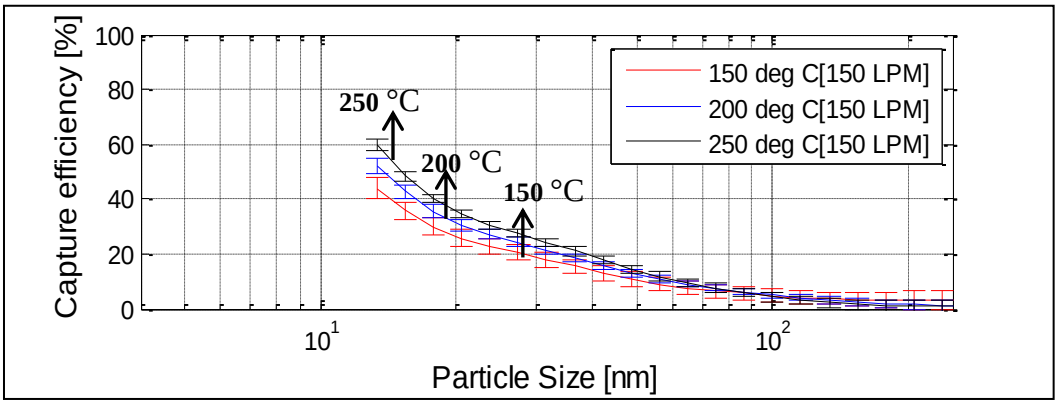

Figure 4.10 - Effect of temperature on capture efficiency at 150 LPM (Experiment no 2, 150°C, Channel Re = 7.76, Sh (at 27 nm) = 10.37 and CE (at 27 nm) = 23.94 %), (Experiment no 10, 200°C, Channel Re = 5.70, Sh (at 27 nm) = 8.79 and CE (at 27 nm) = 25.65 %),(Experiment no 19, 250°C, Channel Re = 5.61, Sh (at 27 nm) = 8.06 and CE (at 27 nm) = 27.38 %)

According to this result, it is very apparent that capture efficiency increases with an increase in temperature. Yet, the rate of increase in capture efficiency from an inlet temperature of 150 to 200 (an increase of 50°C) is around 6.67% (for the particle size of 27 nm) and from an inlet temperature of 200 to 250 is around 6.32% (only a very small percentage difference).

4.3.2 Capture efficiency for the adiabatic conditions (Case B)

In this section, the effect of temperature and residence time on capture efficiency for an adiabatic set up is separately evaluated under two specific cases (B1 & B2). In each trial, the temperatures in all the channels within the substrate were maintained constant.

Effect of temperature (Case B1)

In this case (B1), the flow rate is fixed at 150 LPM for all three temperatures (150, 200 and 250°C). The lines that correspond to experiment numbers 29, 38 and 47 respectively are marked in the Figure 4.11.

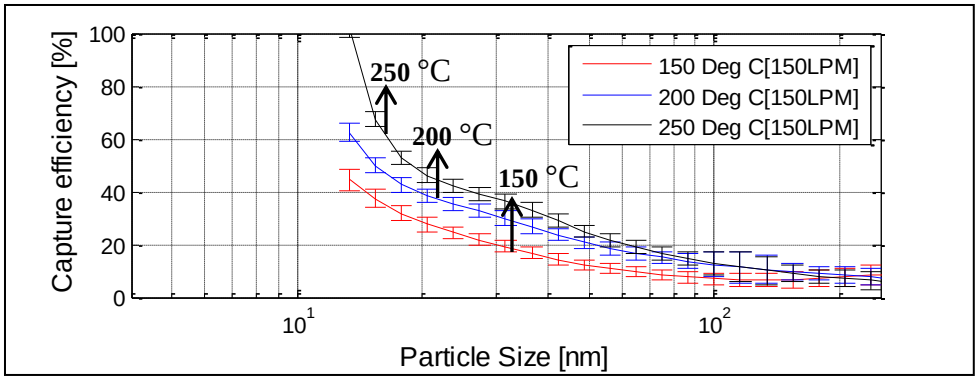

Figure 4.11 - Effect of residence time on capture efficiency at 150°C, adiabatic (Experiment no 29 , 150 LPM, Channel Re = 7.78, Sh (at 27 nm) = 10.37 and CE (at 27 nm) = 25.87 %), (Experiment no 38, 236 LPM, Channel Re = 12.36, Sh (at 27 nm) =17.10 and CE(at 27 nm)=18.51 %),(Experiment no 47, 473 LPM, Channel Re = 24.65, Sh (at 27 nm) = 17.10 and CE (at 27 nm) = 14.41 %)

The effect of residence time on capture efficiency follows the same trend as presented in the non-adiabatic cases (reduction in residence time would increase the capture efficiency and vice versa.)

Effect of residence time (Case B2)

The lines that correspond to experiment numbers 48, 51 and 51 respectively are represented in the Figure 4.12 below.

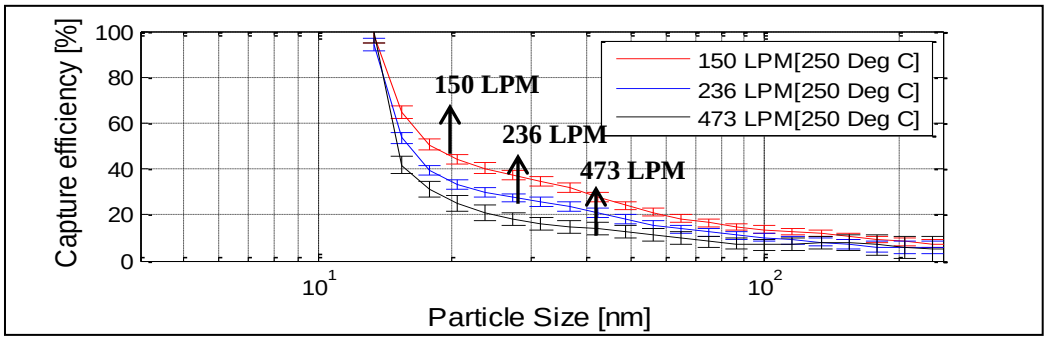

Figure 4.12- Effect of temperature on capture efficiency at 473 LPM, adiabatic case (Experiment no 48, 150°C, Channel Re = 24.65, Sh (at 27 nm) = 17.10 and CE (at 27 nm) = 14.41 %), (Experiment no 51, 200°C, Channel Re = 16.95, Sh (at 27 nm) = 14.36 and CE (at 27 nm) = 19.04 %),(Experiment no 54, 250°C, Channel Re = 15.49, Sh (at 27 nm) = 13.09 and CE (at 27 nm) = 22.99 %)

The results from cases B1 and B2 further confirm the trends noticed in the non-adiabatic trials (Case A1 and A2) in the sense that effect of residence time is higher than effect of temperature e.g. the capture efficiency results obtained from two cases (A1 & A2) showed that an increase of 100°C in temperature results in a 12.56 % increase in capture efficiency while a decrease of 86 LPM (increase in residence time) still results in a higher capture efficiency increase of 14.11 %. Therefore, it is very evident that residence time has a higher effect on capture efficiency compared to temperature. This finding is also explained by the correlations presented in (Johnson & Kittelson, 1996)(eq : (1.19), (1.20), (1.21) and (1.22)) where, capture efficiency is exponentially related to the average mass transfer coefficient (h_m) and residence time. This coefficient (h_m) increases due to increase in temperature leading to an increase in deposition

efficiency. Therefore it can be concluded that temperature has a secondary effect and residence time has a direct effect on capture efficiency.

4.3.3 Comparison between non-adiabatic and adiabatic conditions (Case C)

High residence time & high temperature (Case C1)

The capture efficiency of different cases with the same flow but under different conditions (adiabatic & non-adiabatic) was evaluated. Two specific cases are presented in this section (The rest are presented in Appendix XIV). Based on the results from the previous cases, low flow rate (high residence time) and high temperature scenarios were chosen in order to produce the highest capture efficiencies. The results are presented in the Figure 4.13 below. The adiabatic and non-adiabatic curves correspond to trial numbers 47 and 26 respectively.

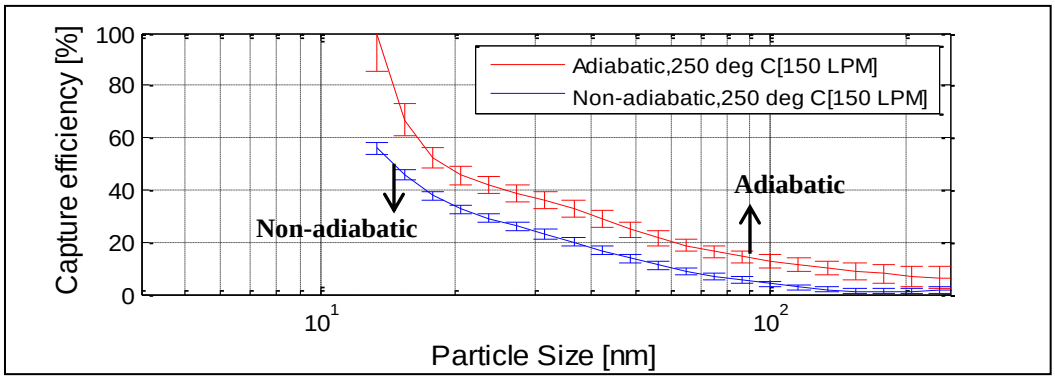

Figure 4.13 - Experiment no 47 at 250°C and 150 LPM, Channel Re =4.47, Sh (at 27 nm) = 8.06 and CE (at 27 nm) = 39.21 %, The experiment no 26, the non-adiabatic conditions at 250°C and 150 LPM, Channel Re = 5.61, Sh (at 27 nm) = 8.06 and CE (at 27 nm) = 25.65 %

The higher capture efficiency of the adiabatic case is due to its higher average channel temperature (most channels were kept at 250°C). In the non-adiabatic case however, the average temperature is lower as channels closest to the periphery of the substrate are at temperatures lower than 250°C (due to un-compensated heat losses to the surrounding) thereby leading to a lower capture efficiency.

Low residence time & low temperature (Case C2)

In Figure 4.14, the adiabatic and non-adiabatic curves correspond to experiment numbers 35 and 8 respectively. However, it is very apparent (similar to the pervious case (C1)) that the adiabatic set up has the higher capture efficiency. Furthermore, the difference between the two CEs is much lesser than the trend noticed in the previous case (C1).This could be due to the high flow rate (low residence time) and low temperature that reduces the heat loss (lower temperature gradient - Section 4.2.2) increasing the average substrate temperature in the non-adiabatic case. This means that both set ups (adiabatic and non-adiabatic in case (C2)) have very close average temperatures. Moreover, since the residence for both cases were kept the same, they showed very close capture efficiency profiles. The radial temperature gradient for non-adiabatic condition in both cases (C1 & C2) was also calculated by using CFD to validate this finding (refer Appendix XV).

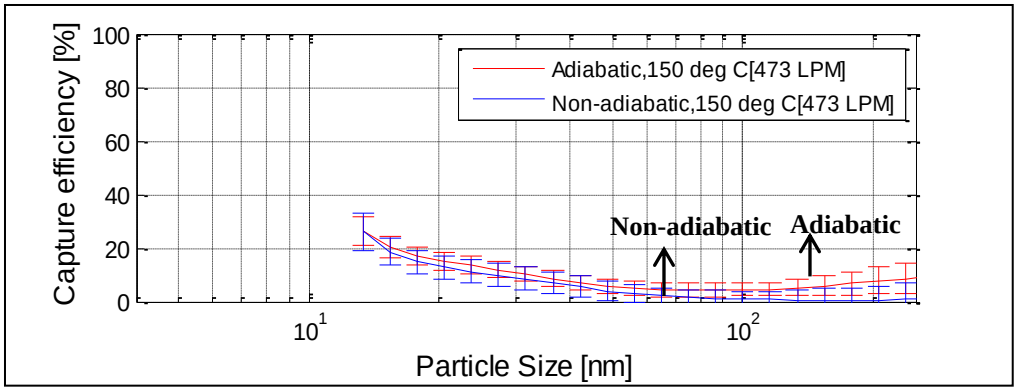

Figure 4.14 - Experiment no 35, adiabatic at 150°C and 473 LPM, Channel Re = 24.65, Sh (at 27 nm) = 17.10 and CE (at 27 nm) = 14.41 %. The non-adiabatic conditions experiment no 8 at 150°C and 473 LPM, Channel Re = 24.16, Sh (at 27 nm) = 17.10 and CE (at 27 nm) = 13.29 %

4.4 Results from single channel capture efficiency simulations (theoretical CE)

The channel simulations were the primary tool to establish the theoretical capture efficiencies. These simulations thus provided a valuable insight into the capture phenomenon within open substrates. The channel was studied under two conditions – non-adiabatic and adiabatic (in a similar manner as detailed in the section on experimental capture efficiency trials Section 4.2). There were two primary effects assessed in these simulations, these were-

- Effect of temperature
- Effect of residence time

4.4.1 Adiabatic channel simulations

The effect of residence time was studied by comparing simulations that had the same operating temperature but differ in flow rates (150 LPM, 236 LPM and 473 LPM). The result of increasing flow rates at constant temperatures of 150 and 250°C are shown in the figure below (Figure 4.15). The theoretical CE reduces with increasing flow rates. This trend is very similar to the one observed while doing experimental trials. As elucidated in the previous sections, increasing the flow rate reduces the residence time of the inert particulates in the monolith channel. The residence time is inversely correlated with the Brownian deposition (as explained in Section 4.3.1), resulting in the observed trend.

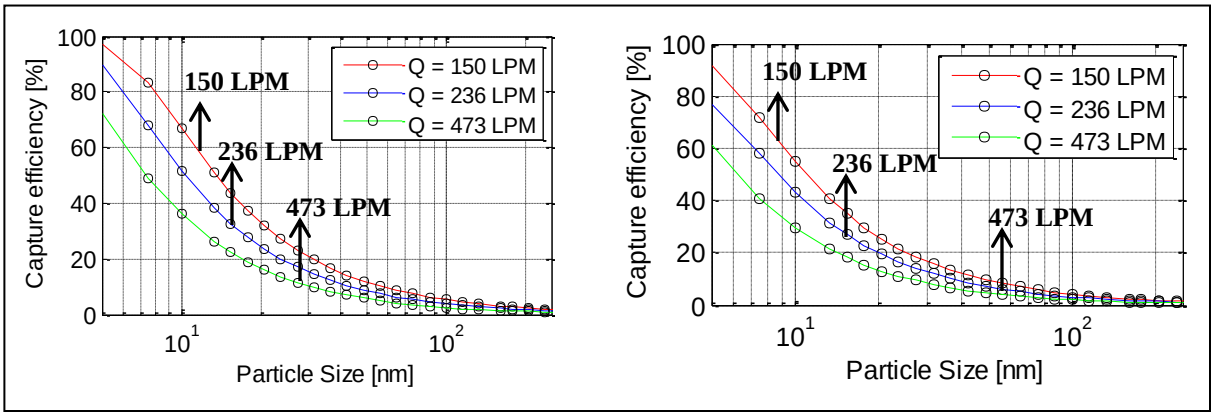

Figure 4.15 – Effect of flow rate on theoretical capture efficiency at a constant temperature of 250°C (left) and 150°C (right)

The effect of temperature on capture efficiency was studied by comparing simulations that had the same operating flow rates of 150 LPM and 437 LPM but differ in temperature (150°C, 200°C and 250°C).

The figure below clearly demonstrates the trend that increasing temperatures increases the capture efficiency. This is primarily attributed to the reduction in diffusivity (within the channel) as we all as corresponding increase in diffusivity of the particles at higher temperatures (as explained in Section 4.3.1).

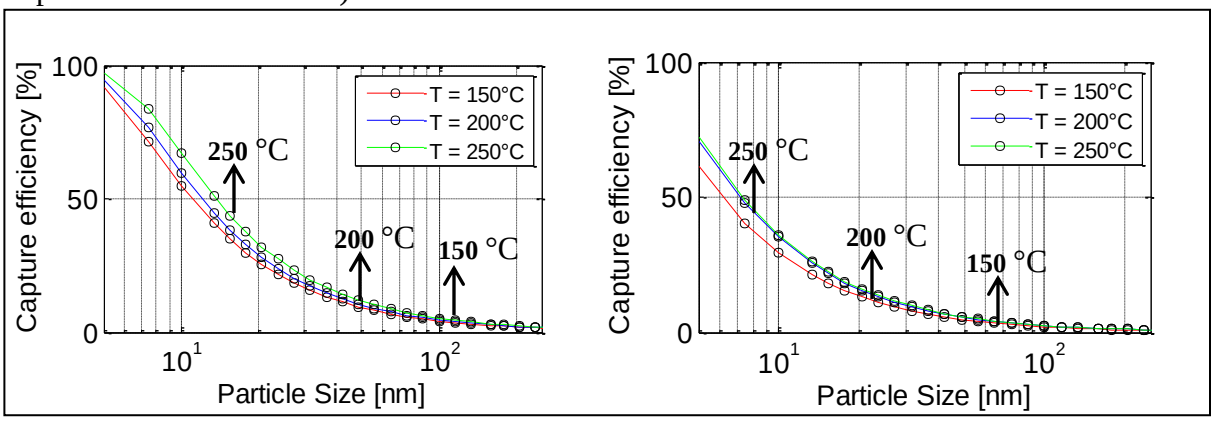

Figure 4.16 – Effect of temperature on theoretical capture efficiency at constant flow rate of 150 LPM (left) and at constant flow rate of 473 LPM (right)

Figures 4.15 and 4.16 clearly indicate the general trend that the residence time (flow rate) brings about a greater spread in CE than the temperature. This trend is discussed more in detail in section 4.3.3.

4.4.2 Non-Adiabatic channel simulations

Channel in an insulated substrate

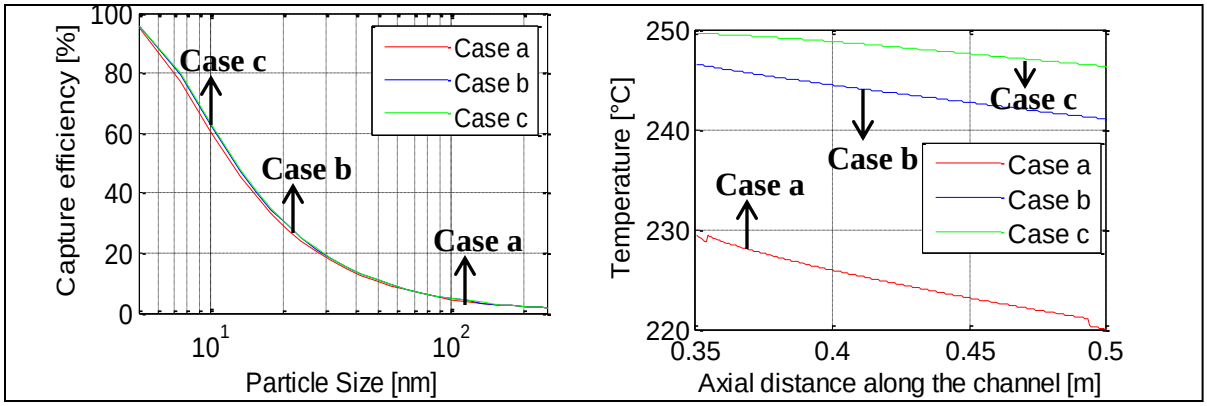

Figure 4.17 – Effect of channel location on theoretical capture efficiency at constant flow rate of about 150 LPM and 250°C – channels in an insulated substrate (left), Axial temperature profile along the channel (right)

The non-adiabatic channel simulations give an insight into the impact of an external temperature gradient (along the channel) on the variation in capture efficiency. The channel studied in a substrate with insulation demonstrated a very important trend with respect to location of the channel within the substrate. As mentioned earlier (section 3.2.3 Figure 3.3), three different channel positions were simulated i.e., *Case a* – Channel close to walls, *Case b* – Channel 0.5 r away from the walls and *Case c* – Channel at the centre, at the same flow rate and inlet temperature in the EATS (250 °C and 150 LPM) . The axial temperature profiles (Figure 4.17 (right)) clearly show that the temperature gradient in the channels close to the walls is much steeper (from about 230 to 220°C) than the corresponding gradients in the channels at quarter distance from the walls (from about 247 to 242°C) and the channels at the centre (from about 250 to 248°C). Thus, the CE's vary as well, with the channel in the centre (Case c) having the highest CE when compared to the CE's at the other two positions. However, the similar gradients in temperature between cases b and c entails that the corresponding difference in CE between these two cases must be almost negligible (change in an absolute magnitude of 10°C in temperature would not bring about such a drastic difference in CE) as shown clearly in the Figure 4.17 above. Moreover, there is no drastic difference in the CE between the three cases, indicating that the insulation being employed is able to maintain as close to adiabatic conditions possible. Thus, if the EATS is operated even without the heating tape (section 2.2.4), the temperature conditions that could prevail within the substrate would ensure that there are no large differences in CE between channels located in the periphery of the substrate and the centre.

Channels in a non-insulated substrate

The channels studied in a non-insulated substrate under the same EATS operating conditions (250°C and 150 LPM, the worst possible operating conditions) also demonstrated the similar trend as in the channels in an insulated substrate. The main difference between the two operating conditions (insulated and non-insulated) would be that, the cases a, b and c have successively and clearly decipherable change in CEs with the channel in the centre (Case c) .The CE dispersion with temperature variation this time is more apparent even between cases b and c.

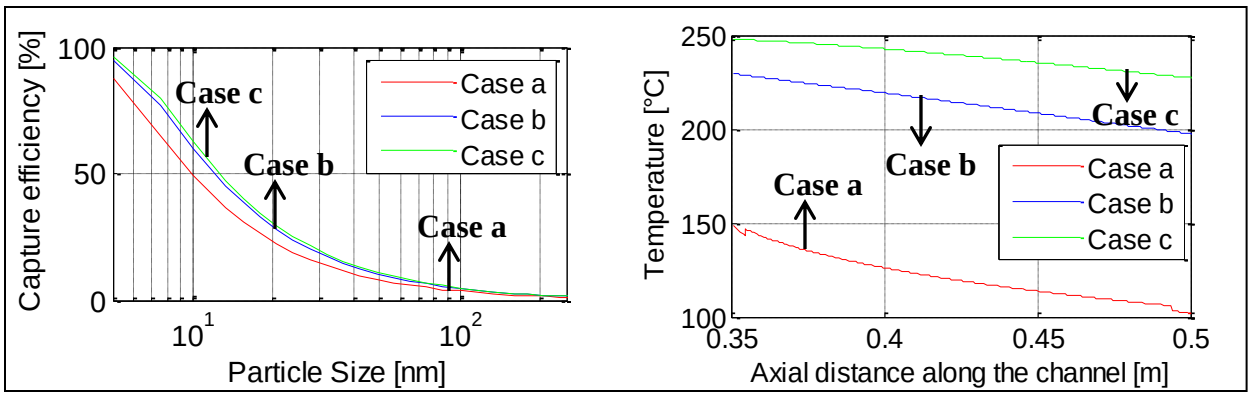

Figure 4.18 – Effect of channel location on theoretical capture efficiency at constant flow rate of about 150 LPM and 250°C – channels in a non-insulated substrate (left), Axial temperature profile along the channel (right)

The axial temperature profiles (Figure 4.18 (right)) are more pronounced in these non-insulated cases (higher heat loss to the surroundings) with the temperature gradient in the channels close to the walls much steeper (from about 150 to 100°C) than the corresponding gradients in the channels at quarter distance from the walls (from about 228 to 198°C) and the channels at the centre (from about 248 to 227°C). Thus, the CEs vary as well, with the channel in the centre (Case c) having the highest CE when compared to the CEs at the other two positions.

These two non-adiabatic channel simulations clearly indicate that, insulation of the substrate does play a vital role in the CE measured across it. Clearly, on using insulated substrates, there are no marked changes in the CE along channels located at different locations within the channel (case a, b and c). This would mean that a mixed cup sampling probe (as employed to sample the exhaust leaving the substrate in this work – Section 2.2.4) would give a reasonably accurate estimate of the CE across the substrate (as long as the system is insulated). No additional work would need to be done by varying the sampling probe types (to say localized probe samplers such as sampling done very close to wall or sampling close to the centre etc.) as the simulations clearly depict that there would be no apparent effect on CE due to these variations.

4.4.3 Results from the Johnson and Kittleson correlations

Both EATS and ingle channel simulations performed were based on the correlations presented in Kittleson et.al (1996). Some simple results were obtained by using these correlations directly. The results from these correlations have been compared with the CFD simulations as well (showing good agreement – refer Appendix XIX). Thus, by directly employing the correlations, exact effects of residence time and temperature can be assessed under fictitious conditions, i.e. operational conditions that cannot be physically achieved in a real system. The only objective of these studies was to provide a pedagogical backing for the results obtained in the simulations and experimental trials.

A ‘pseudo-fluid (air with fictitious properties)’, was studied under the following 5 cases –

- Case A – Base case at 200°C (viscosity and density based on temperature of 200°C)
- Case B – Pseudo-fluid 1 (constant viscosity fluid) at 150°C (density based on temperature of 150°C and viscosity based on temperature of 200°C)
- Case C – Pseudo-fluid 1 at 250°C (density based on temperature of 250°C and viscosity based on temperature of 200°C)

- Case D – Pseudo-fluid 2 (constant density fluid) at 150°C (density based on temperature of 200°C and Viscosity based on temperature of 150°C)
- Case E – Pseudo-fluid 2 at 250°C (density based on temperature of 200°C and Viscosity based on temperature of 250°C)

In this fictitious set-up, the aim of employing a constant viscosity fluid (Pseudo-fluid 1) was to demonstrate the effect of residence time separately at constant particle diffusivities. Hence, the decrease in density of pseudo-fluid 1 on increase in temperature is attributed to decrease in residence time. It must be noted that the velocity of the pseudo-fluid (both 1 and 2) is constant (at 0.2 m/s which corresponds to the 150 LPM flow) in all the cases studied. The constant density fluid (pseudo-fluid 2) on the other hand, would be used to demonstrate the effect of temperature (diffusion coefficient of the particle) at constant residence times.

The Figure 4.17 depicts the results from this simple study. The Case A forms a reference line (blue line) to which the other cases are compared. The Cases B and C (magenta and black lines), which demonstrate the effect of residence time, clearly confirm the trend observed in the experimental as well simulation results. There is a marked decrease in capture efficiency as the residence time increases. This can be seen by reformulating equation (1.19) in the following manner –

$$CE_{channel} = 1 - \exp\left(\frac{-h_m A_s}{Q}\right) \tag{1.19}$$

$$\mathrm{CE}_{\mathrm{channel}} = 1 - \exp\left(\frac{-4\mathrm{ShDL}}{{d_h}^2 \mathrm{U}}\right) \tag{4.1}$$

By employing the pseudo-fluid 1 at constant velocities, equation (4.1) can be re-written as -

$$\mathrm{CE}_{\mathrm{channel}} = 1 - \exp(-C\tau) \tag{4.2}$$

Where 'τ 'is the residence time. Thus, there is an exponential relation between theoretical capture efficiency and residence time. 'C' is synonymous with 'h_m' (Equation (1.17)).Hence, on increasing residence time, capture efficiency increases and the opposite is observed on decreasing residence time.

The effect of temperature at constant residence time can be demonstrated by studying cases D and E (red and green lines). As the temperature is increased the molecular momentum transfer rate increases further which increases the viscosity of the gas. Moreover, at higher temperatures, the diffusion coefficient increases (refer equation (1.22)). The overall effect of these two parallelly acting influences would be an increase in capture efficiency from Case D to Case E as the temperature is increased (demonstrated in Figure 4.17)

Among these two factors, i.e., the residence time and the temperature, the effect of residence time is slightly more pronounced. This can be attributed to the direct exponential dependence of CE on τ (equation (4.2)). The effect of temperature is however slightly less pronounced, this can be attributed to the fact that temperature affects the CE indirectly via the Sherwood number and

diffusivity. Moreover, as the effect of temperature is by no means negligible. In conclusion, both temperature and residence time have a significant impact on the capture efficiency due to Brownian deposition along a monolith channel.

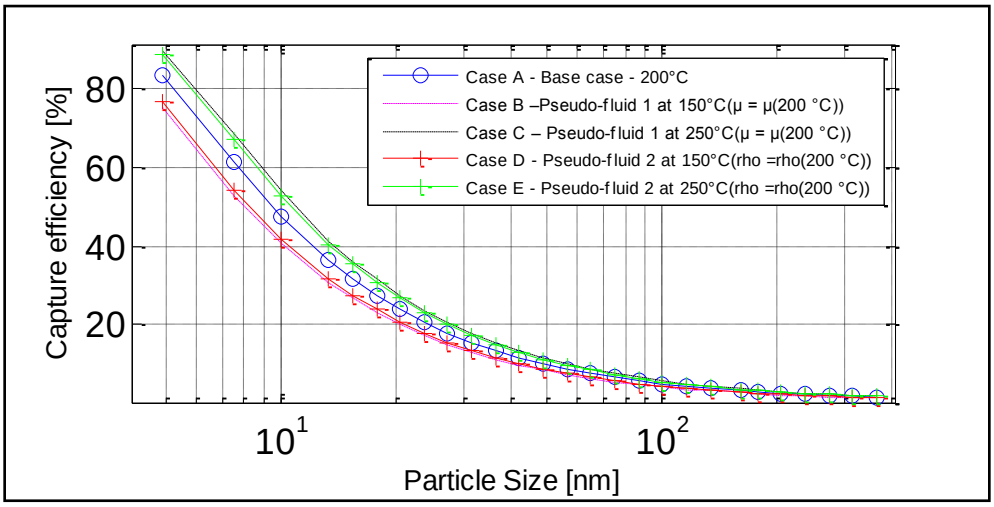

Figure 4.17 – Pseudo-fluid studies

4.5 Comparison between experiments and simulations

The primary objective of this work was to establish congruence between experimental trials and simulations for an inert particulate matter. Thus, the experimental results obtained (in Section 4.3) were compared with the corresponding simulations (in Section 4.4). It must be noted here that the conditions employed in the channel simulations mimicked closely the experimental operating conditions. Hence, any comparison between the two would represent a viable association between theory and experiments.

4.5.1 Comparison under adiabatic conditions

The monolith channel under adiabatic operation would represent the most ideal condition in a substrate. This was one of the primary reasons as to why these conditions have been discussed extensively in the earlier sections (Sections 4.2 and 4.3). Comparisons are thus made between the experiments and simulations at adiabatic conditions in order to verify that PM capture of inert particulate matter can indeed be modelled and simulated utilizing CFD. The CE obtained from the simulations at 150°C and at flow rates of 150 LPM and 436 LPM are compared with the corresponding experiments (Experiment No 29 and 36 in Appendix XI Table 7.6). These results are presented in the Figures 4.18.

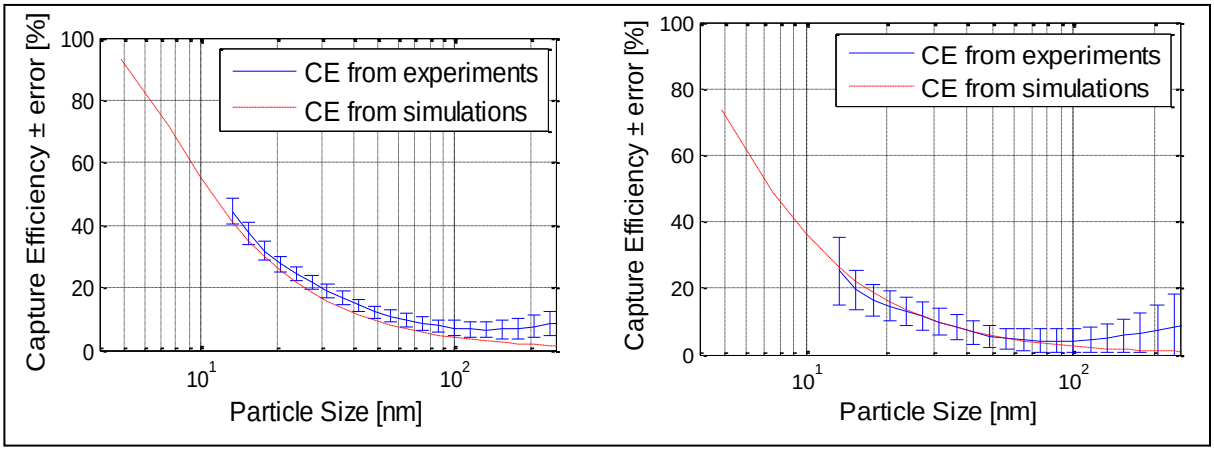

Figure 4.18 - Comparison of CE obtained from experiments and simulations at 150°C, 150 LPM (left) and 150°C, 473 LPM (right)

These figures clearly demonstrate the congruence between simulations and experiments. The CE from simulations fall within the error bars in the experimentally determined CE's indicating a strong agreement between the two. The same trend is also observed in almost all the adiabatic experimental operating points (refer Appendix XVIa).

4.5.2 Comparison under non-adiabatic conditions

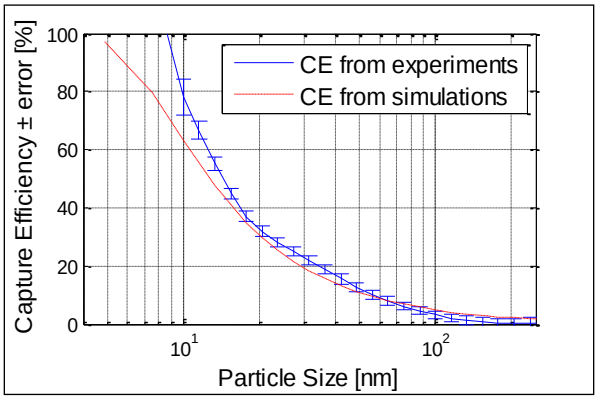

Figure 4.19 - Comparison of CE obtained from experiments and simulations (channel at the centre) at 250°C, 150 LPM

The comparison between experiments and simulations under non-adiabatic conditions also revealed a good agreement between theoretical and experimental findings. The above figure compares the simulation results from a channel at the centre with experimental CE's, at 250°C and 150 LPM. The same congruence is also observed when the channels at the other two positions (close to walls and quarter distance from the walls) are compared with the experimental findings (Refer Appendix XVIb). This further affirms the fact that the sampling methodology chosen in the experiments are able to measure the substrate CE accurately. However, it must be noted that, the experimental CE for smaller particle sizes (values determined from measurement at the DMS500) reaches 100 % as the signal (in these cases) gets below the limit of detection of the instrument, thus the value that gets measured at this size (for PSD) is zero.

5 Conclusions and recommendations

This section describes the final conclusions of this work. These are based on the initial objectives that were established before the start of this work. They are as follows -

5.1 Conclusions

1. *Developed a methodology to generate inert PM at the desirable size and number concentration:* Sodium chloride aerosols (inert) with the constant particle size distributions were produced from their aqueous solution by using the TOPAS ATM230 aerosol generator. The optimal solution concentration (10000 ppm) and atomizer operation pressure (4 bar) in order to produce a desirable size range (10-150 nm) and statistically significant number concentration of PM ($>10^4$ particles/cc - low signal to noise ratio at the DMS) were also obtained. The desirable size and number concentration range chosen in this study were able to draw close parallelisms with actual particulate matter emitted from engines. Therefore, it is possible to generate and measure inert PM using the set up described in this study (section 2.2).

2. *Identified appropriate operating conditions while performing studies on open substrates in order to examine the CE of inert PM*: The chosen experimental operating points (while performing experiments on the EATS) aided in evaluating specific trends pertaining to the capture efficiency of inert particulate matter in an open substrate. The operating flows of 150, 276 and 473 LPM are significantly lower than the nominal engine exhaust flows (about 7080, 12035 and 16990 LPM), however at these low flows, the channel capture efficiencies can be studied more in detail, i.e. trends are easily identified (due to higher capture efficiencies that are measured). (Refer Appendix XVII for detailed sensitivity analyses of CE at nominal engine operations). The chosen temperatures of 150, 200 and 250°C represent approximately the lower and upper boundaries of an operational monolith (in an automotive application) under standard conditions.

3. *Developed a methodology to combine CFD evaluations with experiments:* A strong interdependency between numerical simulations and experimental trials has been demonstrated throughout this work. CFD evaluations have been used as a basis to plan and perform better experiments. The complete 2D-axis symmetric evaluation of the EATS (done prior to the experimental evaluation) assisted in optimizing the EATS pilot set-up in the lab (by the removal of the flow straightener sections), enabling the development of a more uniform temperature distribution at the substrate. Moreover, the thermal profiles of the substrate generated from the simulations aided in establishing a thermocouple map, providing the apt locations to place the temperature probes, in order to monitor the substrate and maintain it at adiabatic conditions (the real time measurements from the temperature probes determined the power supply to the heater and the heating tape used to maintain the set temperature in the EATS). The temperature profiles generated from the EATS simulations without any insulation i.e. at the worst operating conditions (150 LPM and 250°C) also gave a valuable insight into the insulation requirements of the EATS.

4. *Accuracy and validity of the simulations:* The primary argument towards any simulation driven approach to examine a phenomenon, is the accuracy and validity of the results obtained. This validity of the set-up is established by comparing the simulation results

with results from corresponding experiments and or theoretical approximations (empirical correlations, such as Equation (1.17)). A good congruence between experimental results and simulations (Section 4.4) has been demonstrated throughout this work. In addition, the simulations when compared to theoretical correlations, slightly under predict the results (which should be the case). These two comparisons validate the numerical set-up proposed in this work (Refer Appendix XIX).

5. *Demonstrated the congruence between simulation and experiments for capture of inert PM in open substrates:* One of the primary objectives of this work was to evaluate the congruence between numerical simulations and experimental results. This congruence is evident throughout this work, with the simulations corresponding with the experimental results (simulations results are within the error limit of the experimental results as discussed in section 4.4 and in Appendix XVI). In addition the general trends with variation in residence time (flow conditions) and temperature are noticeably similar in both experiments and simulations. This indicates that the theory behind the description of capture efficiency in monolith channels (Brownian deposition) is able to explain the capture phenomena of inert particulates accurately. Moreover, this work also demonstrated the congruence between CFD and theory (Appendix XIX) and further validated the accuracy of the simulations. Thus, CFD analysis can be used when correlations from literature are not sufficient (particularly when there is a temperature or velocity gradient within the channel) to predict the capture efficiency of inert particulates in open substrates.
6. *Developed a methodology to evaluate the effect of residence time and temperature (individually) on the CE of inert PM in open substrates*. This work extensively described the capture efficiency of inert particulate matter (sodium chloride) in open substrates. The effect of different flow (mainly temperature and residence time) and operating conditions (adiabatic and non-adiabatic) were comprehensively investigated by means of both experimental trials and numerical simulations. As explained in the earlier sections (section 4.3.2), the expected capture efficiency variation trends were; increase in residence time and temperature increased the CE with the residence time having the slightly more dominant effect. Both experimental and numerical results have confirmed this trend.

5.2 Recommendations and future work

1. An alternate inert particulate matter system such as PSL (polystyrene) suspension of specific diameters should be evaluated in order to confirm the trends observed in this work.
2. This work should be advanced to the next level of complexity by performing experiments with material closer to engine particulates such as artificial soot in the form of 'Printex U' (carbon black pigment used in printers). Some reactive phenomena of the PM could be studied using this material.
3. The work on the substrate should be extended towards actual test bench studies, i.e. using the DOC, DPF and SCR after treatments in series in order to study the overall efficiency of the after-treatment system.

4. The simulations of CE in the channels must be extended towards reactive PM (including evaporation and mass transfer laws).

6 References

Adler, J. (2005). Ceramic Diesel Particulate Filters. *International Journal of Applied Ceramic Technology, 2*(6), 429-439. doi: 10.1111/j.1744-7402.2005.02044.x

Allen, M. D., & Raabe, O. G. (1982). Re-evaluation of millikan's oil drop data for the motion of small particles in air. *Journal of Aerosol Science, 13*(6), 537-547. doi: http://dx.doi.org/10.1016/0021-8502(82)90019-2

Balkanski, Y., Myhre, G., Gauss, M., Radel, G., Highwood, E. J., & Shine, K. P. (2010). Direct radiative effect of aerosols emitted by transport from road, shipping and aviation. *Atmospheric Chemistry and Physics, 10(10)*, 4477-4489.

Carmichael, G. R. (1982). Estimation of the drag coefficient of regularly shaped particles in slow flows from morphological descriptors. *Industrial & Engineering Chemistry Process Design and Development, 21*(3), 401-403. doi: 10.1021/i200018a009

Chandrasekhar, S. (1943). Stochastic Problems in Physics and Astronomy. *Reviews of Modern Physics, 15*(1), 1-89.

Cox, P. M., Betts, R. A., Jones, C. D., Spall, S. A., & Totterdell, I. J. (2000). Acceleration of global warming due to carbon-cycle feedbacks in a coupled climate model. *Nature* (408), 184-187.

Creaser, D. (2013). Coursework in advanced chemical reaction engineering. *Chalmers Univertsity of Technology, Department of chemical engineering*.

Crowe, C. T., Schwarzkopf, J. D., Sommerfeld, M., & Tsuji, Y. (2011). Multiphase flows with droplets and particles. *CRC Press, Second edition*.

Daley, D. J., & Vere-Jones, D. (1988). An Introduction to the Theory of Point Processes. *Springer–Verlag, New York.*

Donaldson. (2009). Calculating engine airflow. *Engine Horse power and exhaust flow guide, Donaldson Company Inc.*

EEA. (2012). The contribution of transport to air quality - TERM 2012: transport indicators tracking progress towards environmental targets in Europe. *European Environment Agency EEA Report No 10/2012*.

Einstein, A. (1905). Investigation of the theory of Brownian movement. *Dover Publications*.

Ekström, F., & Andersson, B. (2002). Pressure Drop of Monolithic Catalytic Converters Experiments and Modeling. *SAE TECHNICAL PAPER SERIES*(2002-01-1010).

Euro-5/6-Standards. (2009). Euro 5/6 standards (2009/2014): Regulation 715/2007 ("political" legislation) and several comitology regulations. *Official Journal of the European Communities*.

Gray, W. G., & O'Neill, K. (1976). On the general equations for flow in porous media and their reduction to Darcy's Law. *Water Resources Research, 12*(2), 148-154. doi: 10.1029/WR012i002p00148

Gulati, S. T., Cybulski, A., & Moulijn, J. A. (1998). Structured Catalysts and Reactors. *Taylor & Francis*, 501-541.

Guo, B., Fletcher, D. F., & Langrish, T. A. G. (2004). Simulation of the agglomeration in a spray using Lagrangian particle tracking. *Applied Mathematical Modelling, 28*(3), 273-290. doi: http://dx.doi.org/10.1016/S0307-904X(03)00133-1

Hanratty, T. J., Theofanous, T., Delhaye, J.-M., Eaton, J., McLaughlin, J., Prosperetti, A., . . . Tryggvason, G. (2003). Workshop Findings. *International Journal of Multiphase Flow, 29*(7), 1047-1059. doi: http://dx.doi.org/10.1016/S0301-9322(03)00068-5

Hawthorn, R. D. (1974). Afterburner catalysts—effects of heat and mass transfer between gas and catalyst surface. *AIChE Symp. Ser. 70 (137)*, 428-438.

Hinds, W. (1999). Aerosol Technology: Properties, Behavior, and Measurement of Airborne Particles. *Wiley Interscience*.

Johnson, J. E., & Kittelson, D. B. (1996). Deposition, diffusion and adsorption in the diesel oxidation catalyst. *Applied Catalysis B: Environmental, 10*(1–3), 117-137. doi: http://dx.doi.org/10.1016/0926-3373(96)00027-6

Kim, J. H., Mulholland, G. W., Kukuck, S. R., & Pui, D. H. (2005). Slip correction measurements of certified PSL nanoparticles using a nanometer differential mobility analyzer (Nano-DMA) for Knudsen number from 0.5 to 83. *Journal of research of the National Institute of Standards and Technology*, 31-54.

Kittelson, D. B. (1998). Engine and nanoparticles : A Review. *Journal of Aerosol Science., Vol. 29*(No. 5/6), 575 - 588.

Konstandopoulos, A. G., & Kostoglou, M. (2004). Microstructural Aspects of Soot Oxidation in Diesel Particulate Filters. *SAE Technical Paper 01-0693*.

Kumar, P., Fennell, P., Symonds, J., & Britter, R. (2008). Treatment of losses of ultrafine aerosol particles in long sampling tubes during ambient measurements. *Atmospheric Environment 42*, 8819-8826.

Li, A., & Ahmadi, G. (1992). Dispersion and Deposition of Spherical Particles from Point Sources in a Turbulent Channel Flow. *Aerosol Science and Technology, 16*(4), 209-226. doi: 10.1080/02786829208959550

Lighty, J. S., Veranth, J. M. & Sarofim, A. F. (2004). Combustion Aerosols: Factors Governing Their Size and Composition and Implications to Human Health. *J. Air Waste Manage. Assoc. , 50*, 1565-1618.

Liu, Z. G., Berg, D. R., Swor, T. A., & Schauer, J. J. (2008). Comparative Analysis on the Effects of Diesel Particulate Filter and Selective Catalytic Reduction Systems on a Wide Spectrum of Chemical Species Emissions. *Environmental Science & Technology, 42*(16), 6080-6085. doi: 10.1021/es8004046

Loth, E. (2009). Computational Fluid Dynamics of Bubbles, Drops and Particles. *Cambridge University Press*.

Milton, G. W., & Willis, J. R. (2007). On modifications of Newton's second law and linear continuum elastodynamics. *Proceedings of the Royal Society A: Mathematical, Physical and Engineering Science, 463*(2079), 855-880. doi: 10.1098/rspa.2006.1795

Navier, C. L. M. H. (1822). M´emoire sur les Lois du Mouvements des Fluides. *Mem.de l'Acad. d. Sci. 6 398*.

Oberkampf, W. L., & Trucano, T. G. (2002). Verification and validation in computational fluid dynamics. *Progr. Aerospace Sci., 38*, 209-272.

Ounis, H., Ahmadi, G., & McLaughlin, J. B. (1991). Brownian diffusion of submicrometer particles in the viscous sublayer. *Journal of Colloid and Interface Science, 143*(1), 266-277. doi: http://dx.doi.org/10.1016/0021-9797(91)90458-K

SAE. (1993). Chemical methods for the measurement of nonregulated diesel emissions *SAE Handbook. Engines, Fuels, Lubricants, Emissions, and Noise. 3*

Shah, S. D., Cocker, D. R., 3rd, Miller, J. W., & Norbeck, J. M. (2004). Emission rates of particulate matter and elemental and organic carbon from in-use diesel engines. [Research Support, Non-U.S. Gov't

Research Support, U.S. Gov't, Non-P.H.S.]. *Environ Sci Technol, 38*(9), 2544-2550. doi: 10.1021/es0350583

Sharipov, F. (2007). Rarefied gas dynamics and its applications to vacuum technology. *CAS - CERN Accelerator School and ALBA Synchrotron Light Facility: CERN document server*.

Sjöblom, J., & Ström, H. (2013). Capture of automotive particulate matter in open substrates. *Accepted for publication in - Industrial and Engineering Chemistry Research*.

Stokes, G. G. (1845). On the Theories of the Internal Friction of Fluids in Motion. *Trans. Cambridge Phys. Soc. 8.*

Ström, H. (2011). Particulate Flows in Aftertreatment Systems : Model Development and Numerical Simulations. *PHD thesis, Chalmers University of Technology*(ISBN 978-91-7385-490-0).

Tomašić, V., & Jović, F. (2006). State-of-the-art in the monolithic catalysts/reactors. *Applied Catalysis A: General*, *311*(0), 112-121. doi: http://dx.doi.org/10.1016/j.apcata.2006.06.013

Vaaraslahti, K., Virtanen, A., Ristimäki, J., & Keskinen, J. (2004). Nucleation Mode Formation in Heavy-Duty Diesel Exhaust with and without a Particulate Filter. *Environmental Science & Technology*, *38*(18), 4884-4890. doi: 10.1021/es0353255

Wendt, J. F. (2009). Computational Fluid Dynamics : An Introduction. *Springer., 3rd Edn.*

7 Appendices

Appendix I: Creeping flow calculations

The particle Reynolds number (Re_p) is given as –

$$Re_p = \frac{D_p v \rho}{\mu}$$

Where D_p is the particle diameter, v is the velocity of approaching stream, ρ and μ are the density and viscosity of the fluid respectively. A demonstrative calculation of Rep encountered in a monolith channel with regard to the conditions described in this work is shown below.

D_p = 100 nm (nominal value)

v = 0.63 m/sec (for max flow rate of 473 LPM)

ρ = 0.83 Kg/m^3 (for T = 150°C)

μ = 2.37e-05 Pa-s (for T = 150°C)

$$Re_p = \frac{100e^{-9} * 0.63 * 0.83}{2.37e^{-05}} = 0.002 \ll 1$$

This clearly shows that, Stokes law (Equation (1.11)) is clearly applicable under all the cases discussed in this work.

Appendix II: Published values of Knudsen-Weber slip correction parameters for the correction of stokes law)

Table 1 - Knudsen-Weber slip correction parameters (Adapted from (Allen & Raabe, 1982))

Author	Mean free path, λ (μm)	α	β	γ	$\alpha+\beta$
Knudsen and Weber (1911)	0.09417	0.772	0.40	1.63	1.172
Millikan (1923b)	0.09417	0.864	0.29	1.25	1.154
Langmuir (1942)	0.133	0.62	0.22	2.2	0.84
Davies (1945)	0.066	1.257	0.40	1.10	1.657
DeMarcus and Thomas (1952)	0.0655	1.25	0.44	1.09	1.690
Reif (1958)	0.0652	1.26	0.45	1.08	1.710
Fuchs (1964)	0.0653	1.246	0.42	0.87	1.666
Dahneke (1972)	0.066	1.234	0.414	0.87	1.648
Allen and Raabe (1982)	0.0673	1.155	0.471	0.596	1.626

In the work, the mean free path was estimated to be close to about 66 nm (25°C and 1 atm). Thus the highlighted values of slip corrections were chosen.

Appendix III: TOPAS ATM-230 operating pressure and recirculation ratio

The following diagram displays the link between the ATM 230 operating pressure (bar) and the produced aerosol flow rate (litre per minute) based on two different nozzle sizes (1.1 &1.3) as -

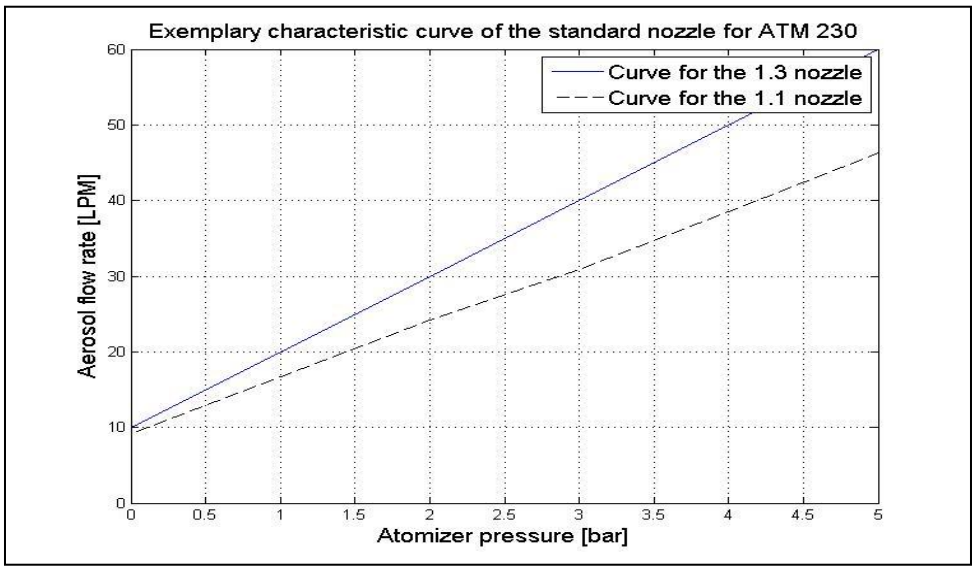

Figure 7.1a-The characteristic curve of the nozzles (1.1 &1.3)

More details regarding the expected particle size from the atomizer droplets (generated from DEHS) are presented in following sections.

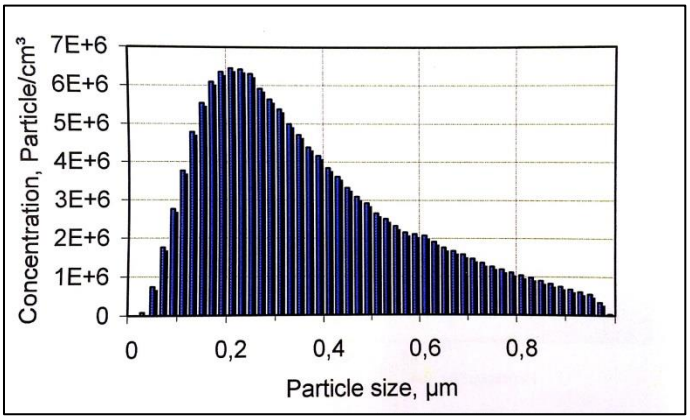

Figure 7.1b – PSD of DEHS (Di-Ethyl-Hexyl-Sebacat) measured by scanning mobility particle sizer

Di-Ethyl-Hexyl-Sebacat (DEHS) is a no soluble, colourless and odourless liquid which is suitable for producing steady aerosols. The main proportion of droplets generated by aerosol generators series ATM 230 can to be stated in the most penetration particle size (0.2...0.3µm). The produced DEHS aerosol features very high particle concentrations (>10^7 particles/cm^3) which is close to the aforementioned penetration particle size range.

The recirculation ratio of droplets in ATM 230 was also calculated as-

First, a plate was placed under the baffle plate in order to block the passage of coarse droplet stream from going back to the main solution container. In this way it was possible to calculate Q1 which is the volumetric flow rate of escaped fine droplets. It took 25 seconds to use up 15 ml salt solution. So, Q1 was calculated as: 15/25=0.65(ml/sec)

Then, the plate was removed and recirculation of coarse droplets into the system was allowed. This took nearly 3 hours to use 25 ml of salt solution .Therefore, Q2 was calculated as: 25/10800=0.002 (ml/sec).By considering a simple mass balance, Q3 was calculated as: (Q1-Q2) =0.65 (ml/sec) and finally the recirculation ratio was calculated as: Q3/Q2=300. This would mean that, about 97% of the droplets formed are coarse, which would mean that they impact on the baffle plate and fall back down into the main solution. The aerosol foam is formed by the remaining 3% of the solution. This would in turn mean that, small volumes of solutions can sustain for larger periods of time to provide the requisite PSD and number concentration desired.

A schematic flow sheet of this reaction is presented in the Figure below-

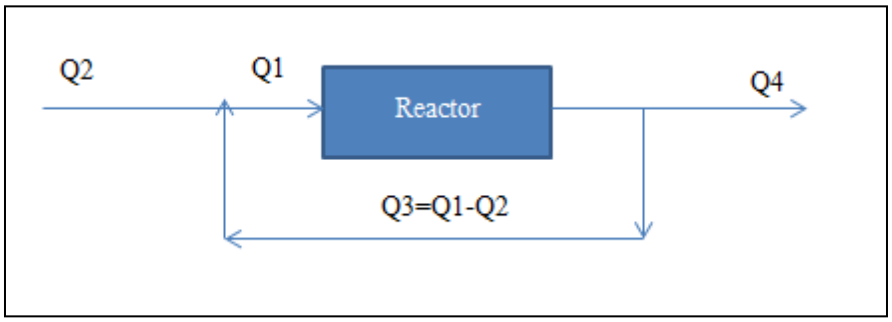

Figure 7.2 Recirculation ratio calculation of coarse particles produced at the TOPAS ATM-230 atomizer

Appendix IV: Preliminary trials

a) First sets of experiments

A D-optimal design with variable effects confounded is chosen. A D-optimal design is a computer aided design which contains the best subset of all possible experiments. These designs are straight optimizations based on a chosen optimality criterion. The design matrices are usually not orthogonal and effect estimates are correlated. The statistical software MODDE was used to generate the requisite D-optimal design. The design is as follows.

Table 7.3 Experimental design for preliminary trials (first set)

Exp No	Pupstr(bar)	Concentration(PPM)	1dil	2dil
1	3	10	1	-1
2	3	10	5	-1

3	1	10	1	1
4	3	10	1	1
5	1	10	5	0
6	1	10	3	-1
7	3	10	3	1
25	1	10	1	-1
26	3	10	1	-1
27	1	10	5	1
28	3	10	5	0
29	2	10	1	1
30	2	10	5	-1
8	1	100	1	-1
9	1	100	1	1
10	1	100	5	1
11	3	100	1	0
12	3	100	5	0
13	2	100	1	-1
14	2	100	5	-1
15	2	100	5	1
31	1	100	5	-1
32	3	100	1	1
33	3	100	5	1
34	1	100	1	0
35	1	100	3	1
36	3	100	3	-1
37	3	100	3	-1

16	1	10000	1	-1
17	3	10000	1	-1
18	1	10000	5	-1
19	3	10000	5	-1
20	1	10000	1	1
21	3	10000	1	1
22	1	10000	5	1
23	3	10000	5	1
24	2	10000	3	0
38	1	10000	1	-1
39	3	10000	1	-1
40	1	10000	5	-1
41	3	10000	5	-1
42	1	10000	1	1
43	3	10000	1	1
44	1	10000	5	1
45	3	10000	5	1
46	2	10000	3	0
47	2	10000	3	0
48	2	10000	3	0
49	2	10000	3	0

b) ***Second set of experiments***

Table 7.4 Experimental design (3^3) for preliminary trials (second set)

Exp No.	Concentration(PPM)	Up stream pressure(bar)	Heated pipe (°C)
1	5000	1.5	40
2	5000	2.5	40
3	5000	3.5	40
4	10000	1.5	40
5	10000	2.5	40
6	10000	3.5	40
7	15000	1.5	40
8	15000	2.5	40
9	15000	3.5	40
10	5000	1.5	70
11	5000	2.5	70
12	5000	3.5	70
13	10000	1.5	70
14	10000	2.5	70
15	10000	3.5	70
16	10000	2.5	70
17	10000	2.5	70
18	10000	2.5	70
19	15000	1.5	70
20	15000	2.5	70
21	15000	3.5	70
22	5000	1.5	100
23	5000	2.5	100
24	5000	3.5	100
25	10000	1.5	100
26	10000	2.5	100
27	10000	3.5	100
28	15000	1.5	100
29	15000	2.5	100
30	15000	3.5	100

Appendix V: EATS flow calculations (Reynolds number calculations for EATS inlet and monolith channel)

a) ***Re at the EATS inlet***

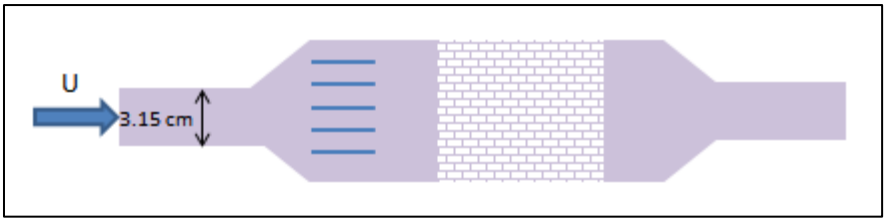

U = 2.56 m/sec

$$Re = \frac{d_h U \rho}{\mu}$$

$$Re = \frac{0.0315 * 2.565 * 0.83}{2.37e^{-05}} = 1983 < 2300$$

As the Re is lower than 2300 (laminar Re limit for pipes), the flow profile at the EATS inlet is laminar.

b) ***Re in the channel***

U = 0.63 m/sec

$$Re = \frac{d_h U \rho}{\mu}$$

$$Re = \frac{1.118e^{-3} * 0.63 * 0.835}{2.37e^{-05}} = 24.7 << 2300$$

As the Re is significantly lower than 2300 (laminar Re limit for a square channel), the flow profiles within the channels are clearly laminar

Appendix VI: Typical values of C_2 (viscous resistance factor) along with the corresponding monolith pressure drops

Table 7.5 – Inertial resistance factors used in the porous zone model

Pressure drop across the substrate	Inertial resistance factor(C_2)
18.6 Pa	1.00E+07
28.47 Pa	8.00E+07
57.01 Pa	9.00E+07

The operating monolith pressures are obtained by manually adjusting this viscous resistance factor. Typical values of C_2 along with the corresponding monolith pressure drops are listed in Table 7.5 above.

Appendix: VII UDF's

Diffusivity

The following UDF calculates the 'Brownian diffusion' co-efficient for particles of different sizes diffusing together in air.

```
#include "udf.h"
#include "dpm.h"
#include "math.h"

DEFINE_DIFFUSIVITY(Custom_diffusivity,c,t,i)
{

   real Cc,Dab,Fd,cmol,mean_free_path;
   real  Knp;
   real P_DIAM[27] ={4.87e-9,7.5e-9,10e-9,13.34e-9,15.4e-9,17.78e-9,20.54e-9,23.71e-
9,27.38e-9,31.62e-9,36.52e-9,42.17e-9,48.7e-9,56.23e-9,64.94e-9,74.99e-9,86.6e-9,100e-
9,115.48e-9,133.35e-9,159.99e-9,177.83e-9,205.35e-9,237.14e-9,273.84e-9,316.23e-
9,365.17e-9}; /* Particle size bins */
   if(i<27)
   {
   cmol = pow((8.0*101325.0/(M_PI*C_R(c,t))), 0.5);
    mean_free_path = C_MU_L(c,t)/(0.499*cmol*C_R(c,t));
Fd=3*M_PI*P_DIAM[i]*C_MU_L(c,t); /* Drag with Cunningham factor */
    Knp = 2.0*mean_free_path/P_DIAM[i];
       Cc = (1.0 + Knp*(1.257 + 0.406*exp(-1.1/Knp)));
       Dab = (1.3806488e-23)*C_T(c,t)*Cc/Fd;
   }
   else
   {
          Dab = 2.55e-5;  /* species i is the gas */
   }
       return Dab;

}
```

Wall temperature profile

The following UDF sets a temperature profile on the walls of the channel. This temperature profile is utilized primarily in the non-adiabatic simulations.

```
DEFINE_PROFILE(wall_ins_casea,thread,index)
{
   real x[ND_ND]; /* this will hold the position vector */
   real y,T;
   face_t f;
   begin_f_loop(f,thread) /* loops over all faces in the thread passed in the DEFINE
macro argument */
   {
      F_CENTROID(x,f,thread);
      y = x[2];

         T = (82.4579*((pow(y,2.0))))+(45.7558*y)+(493.7469);
      F_PROFILE(f,thread,index) =T;
   }
   end_f_loop(f,thread)

}
```

Appendix VIII: Mesh quality study

a) EATS

As elucidated in the earlier sections, the quality of the chosen mesh would have a significant impact on the nature of the results that can be obtained from a particular simulation. The effect of the mesh quality has been studied by solving the velocity field for four different meshes, each with successively larger number of computational cells. The velocity of the outlet is plotted as a function of the number of cells. The results of this study are as follows

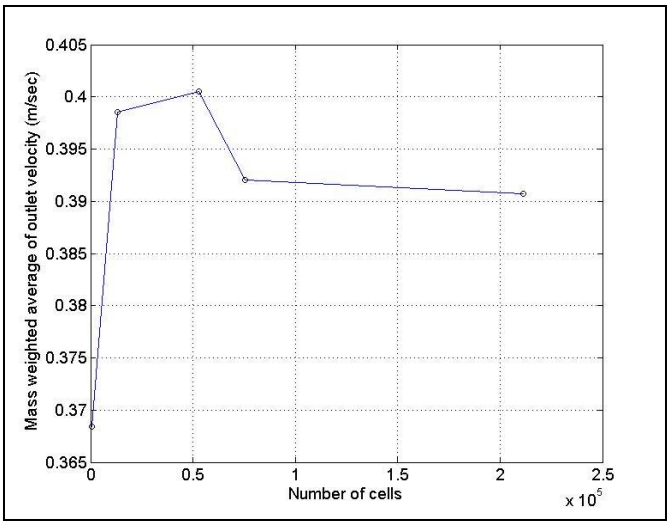

Figure 7.3 – Solution mesh independency study

The solutions (mass weighted average of outlet velocity) from 5 different meshes are compared in the Figure 7.3 above .The figure above confirms the fact that the solution to the EATS flow field becomes mesh independent when the minimum number of cells in the mesh exceeds about 100000 cells. Hence the mesh chosen for all the further computations had a size of about ***115000 cells***. The quality of the chosen mesh is also very apparent in the contour plot below.

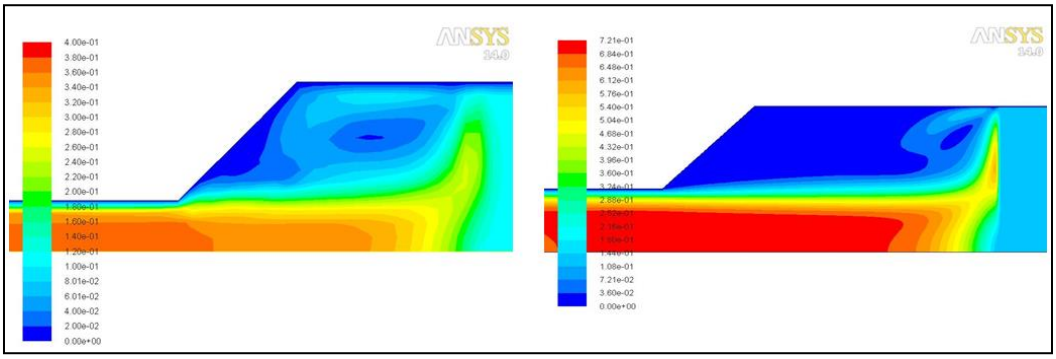

Figure 7.4 - Contours coloured by velocity magnitude coarse mesh (left) and fine mesh (right)

Clearly the finer mesh is able to resolve the flow in the recirculation zones (diverging section of the geometry) much better than the coarser one.

b) Channel

The quality of the mesh employ to simulate the single channel was assessed. This study is very critical in order to ensure that the solution can be trusted (well resolved) and at the same time is mesh independent. The effect of the mesh quality has been studied by solving the velocity field for four different meshes, each with successively larger number of computational cells. The velocity of the outlet is plotted as a function of the number of cells. The results of this study are as follows

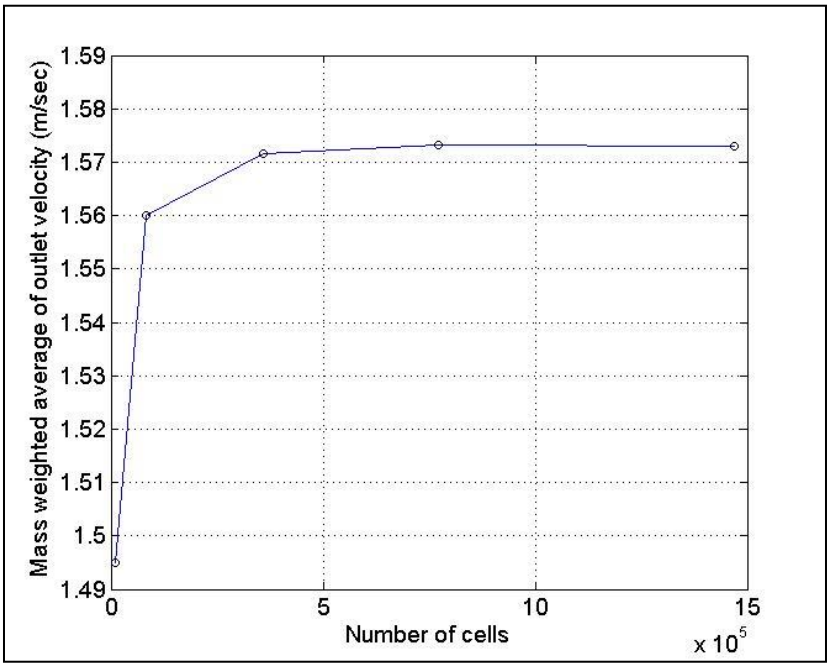

Figure 7.5 – Mesh independency studies

The solutions (mass weighted average of outlet velocity) from 5 different meshes are compared in the Figure 7.5 above .The figure above confirms the fact that the solution to the EATS flow field becomes mesh independent when the minimum number of cells in the mesh exceeds about 400000 cells. Hence the mesh chosen for all the further computations had a size of about ***927000 cells***. The quality of the chosen mesh is also very apparent in the contour plot below (velocity is well resolved in the finer mesh).

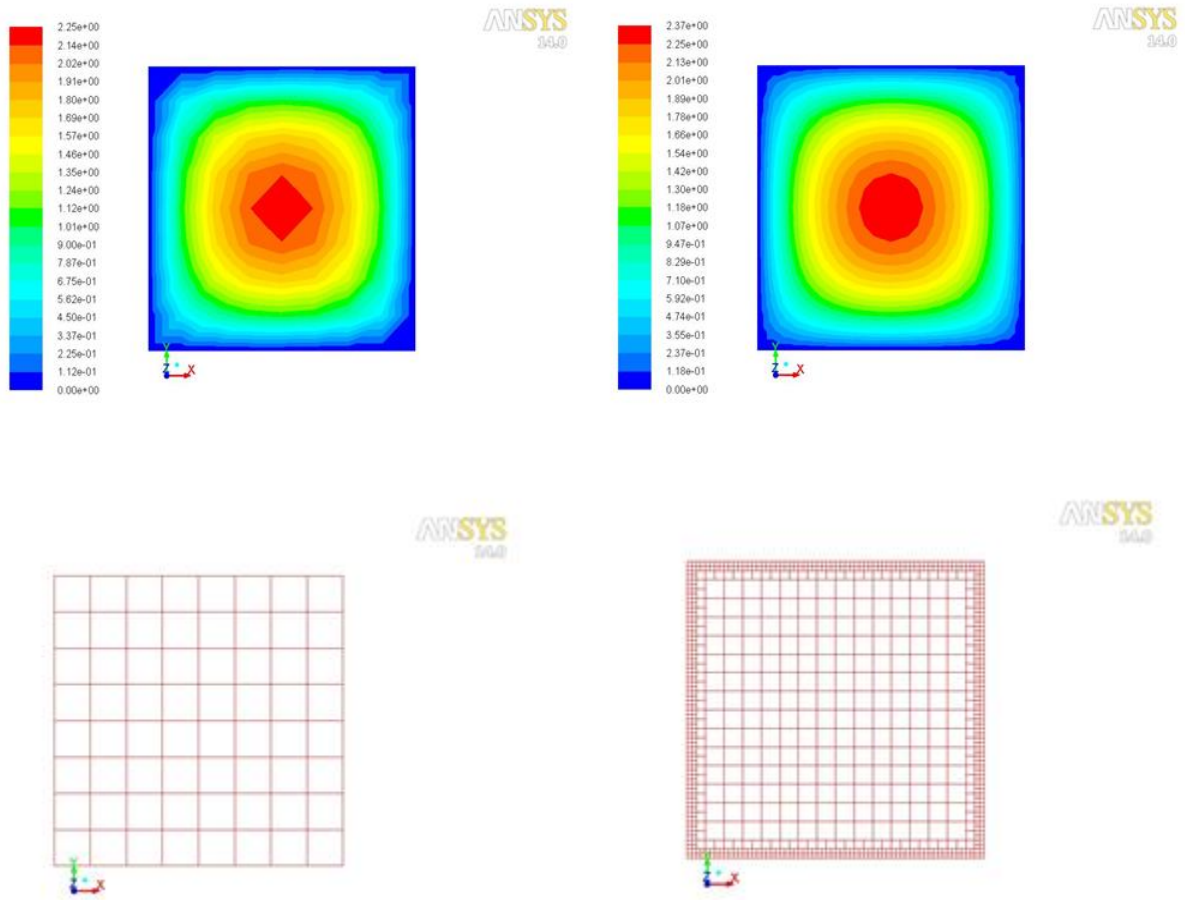

Figure 7.6 - Contours coloured by velocity magnitude coarse mesh (top left) , fine mesh with wall refine (top right), coarse mesh (bottom left) and wall-refined mesh (bottom right)

Appendix IX: Temperature profile comparison between experiments and simulations

As mentioned earlier, some preliminary studies were done in the EATS with just air (no particulate flow). These studies were done in order to establish whether the conditions predicted by the simulations were actually encountered in reality. A comparison between the temperature field measured in real time using the thermocouples (described above) and the field predicted by the CFD data would thus be a very good way to validate the simulations. The simulations done at a flow rate of 150 LPM and 250°C with insulation were chosen. The temperature profile corresponding to thermocouple positions 3, 5 and 8 were chosen from the EATS simulation. These were then compared with the data recorded by thermocouples 3, 5 and 8 during the experiment trials under the same conditions. This comparison is plotted in the Figure (7.7) below.

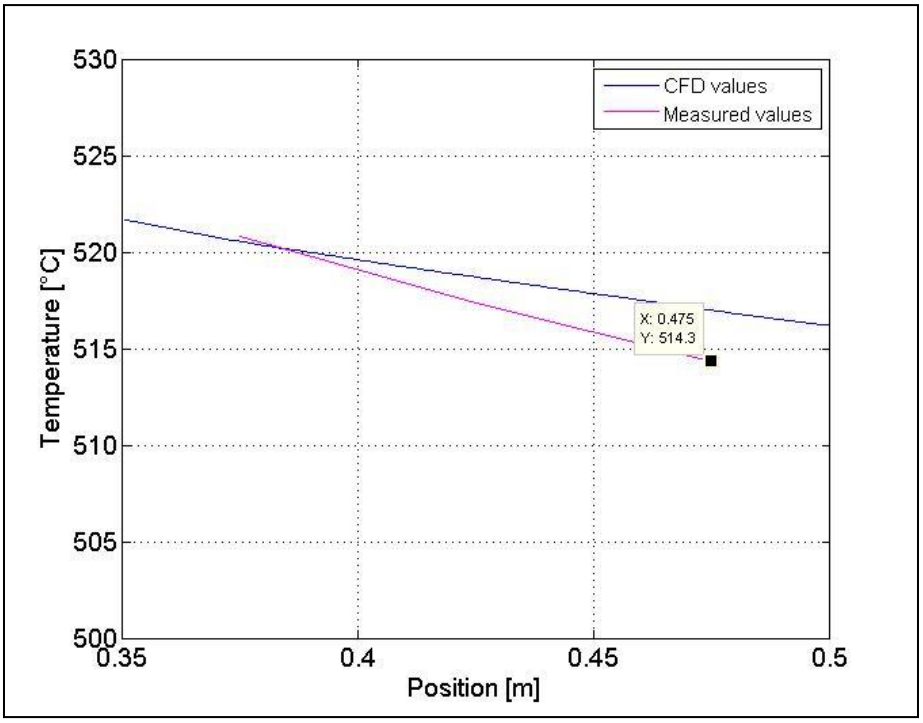

Figure 7.7 - Comparison between CFD data and measure values

The simulations predicted a temperature drop of about 10 K (see Figure above). The values measured by the thermocouple (averaged over time) indicated a temperature drop (along the same position) of about 12 K. This indicates that the simulation indeed correspond well with the experiments. This trend is noted even when comparing other EATS operating points with experimental measurement of temperature.

Appendix X: Sample time stability assessments

The initial data analysis included the time stamp syncing between the lab-view (desktop) and the DMS data. It the data was sampled at about 1Hz for both the DMS, however the EATS lab-view interface sampled at about once in 7 seconds. Thus the difference in time stamps between both the sets of data was corrected by including a 'time lag factor'. A final data matrix containing all the desired variables with their measured values was generated. This data matrix was used to plot the various experiments at the corresponding time stamps. The stability of the measured data was checked by plotting the measure time with the total particle size distribution (PSD). This plot aided in choosing the right time points for measured data analysis (i.e. data that was stable over time was chosen). The chosen time stamps were then plotted over an extended time range (chosen range ±60 seconds) in order to further verify that the right time stamps were chosen. A few demonstrative illustrations of this exercise are provided below –

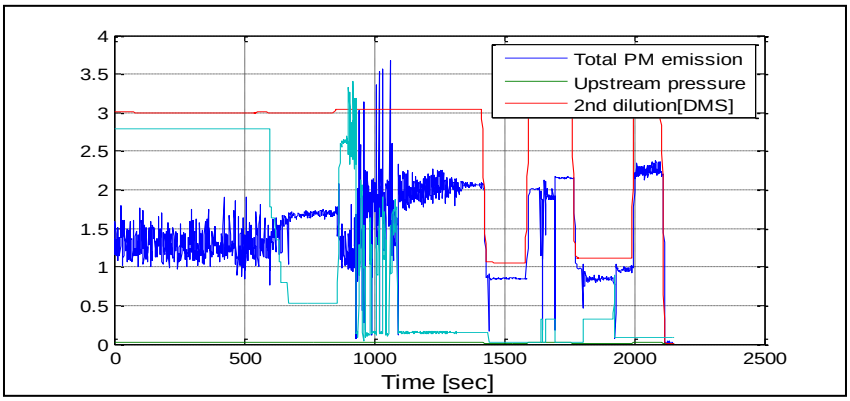

Figure 7.8 - Time plot to choice the right sampling points

The Figure 7.8 above was used to manually note down the corresponding time stamps for each experiment. The time stamps chosen here would be a preliminary estimate of the most stable measurements. In the next assessment these chosen time stamps are over laid over the measured data over the extended time interval in order to further refine the time intervals, to include only the most stable data points. A demonstrative example is illustrated below.

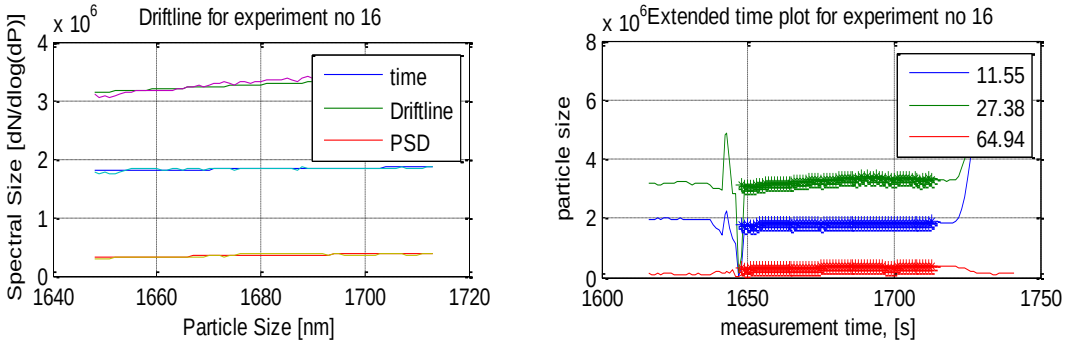

Figure 7.9 – Drift-line (left) and extended time plot (right)

Appendix XI: CE Experiments

Table 7.6 - Non-adiabatic CE trials operating conditions

Exp No.	Average Temperature (deg C)	Pressure across substrate (Pa)	Flow rate (LPM)	Sampling positions	Concent-ration	Up stream pressure	Heated pipe temperature (°C)	Total dilution at DMS	DMS Sample flow (LPM)	Number concentration at 28 nm peak (N/cc)	Total number concentration measured at DMS (N/cc)	Preliminary CE measured at 28 nm (%)
1	130.5	18.6	150	Bef	10000	4 bar	200	10	8.1	395000	303500	24.05
				After	10000	4 bar	200	10	8.11	300000	245000	
2				Bef	10000	4 bar	200	10	8.05	380000	298150	21.05
				After	10000	4 bar	200	10	8.07	300000	245000	
3				Bef	10000	4 bar	200	10	8.03	385000	298350	23.37
				After	10000	4 bar	200	10	8.09	295000	240000	
4		28.47	236	Bef	10000	4 bar	200	10	8.07	230000	171000	17.39
				After	10000	4 bar	200	10	8.11	190000	153500	
5				Bef	10000	4 bar	200	10	8.02	231000	171000	17.74
				After	10000	4 bar	200	10	8.07	190000	152000	
6				Bef	10000	4 bar	200	10	8.03	230000	179000	17.39
				After	10000	4 bar	200	10	8.09	190000	152000	
7		57.01	473	Bef	10000	4 bar	200	10	8.06	120000	95000	12.5
				After	10000	4 bar	200	10	8.09	105000	85600	
8				Bef	10000	4 bar	200	10	8.05	125000	96800	12
				After	10000	4 bar	200	10	8.09	110000	83750	

9				Bef After	10000 10000	4 bar 4 bar	200 200	10 10	8.05 8.05	125000 107500	94000 85600	14
10	172.5	18.8	150	Bef After	10000 10000	4 bar 4 bar	200 200	11.98 12	8.08 8.08	980000 700000	800000 615000	28.57
11				Bef After	10000 10000	4 bar 4 bar	200 200	11.99 12.03	7.99 8.08	980000 720000	800000 612000	26.53
12				Bef After	10000 10000	4 bar 4 bar	200 200	11.98 12	8.03 8	1000000 720000	800000 610000	28
13		28.59	236	Bef After	10000 10000	4 bar 4 bar	200 200	11.75 12	8.04 8.07	680000 560000	515000 415000	17.64
14				Bef After	10000 10000	4 bar 4 bar	200 200	11.94 12.03	8.05 8.02	680000 540000	525000 420000	20.58
15				Bef After	10000 10000	4 bar 4 bar	200 200	12.05 12	8.03 8.039	675000 540000	530000 420000	20.75
16		57.15	473	Bef After	10000 10000	4 bar 4 bar	200 200	12.04 12	8.08 8.08	380000 325000	295000 255000	14.47
17				Bef After	10000 10000	4 bar 4 bar	200 200	12.03 12	8.05 8.09	380000 320000	300000 260000	15.78
18				Bef After	10000 10000	4 bar 4 bar	200 200	12.05 12	8.05 8.05	381000 340000	300000 262500	10.76
19		18.8	150	Bef	10000	4 bar	200	15	7.98	900000	786565	26.67

				After	10000	4 bar	200	15	8.01	660000	600500	
20				Bef	10000	4 bar	200	15	8.02	920000	790000	28.26
				After	10000	4 bar	200	15	8.04	660000	600500	
21				Bef	10000	4 bar	200	15	8.03	920000	775000	28.26
				After	10000	4 bar	200	15	8.05	660000	600000	
22				Bef	10000	4 bar	200	15	8.04	680000	580000	26.47
				After	10000	4 bar	200	15	8.05	500000	470000	
23	213.5	31.65	236	Bef	10000	4 bar	200	15	8.05	660000	550000	24.24
				After	10000	4 bar	200	15	8.02	500000	445000	
24				Bef	10000	4 bar	200	15	8.03	660000	550000	18.18
				After	10000	4 bar	200	15	8.039	500000	450000	
25				Bef	10000	4 bar	200	15	8.06	375000	306000	17.33
				After	10000	4 bar	200	15	8.09	310000	270000	
26		63.56	473	Bef	10000	4 bar	200	15	8.05	360000	315000	16.67
				After	10000	4 bar	200	15	8.09	300000	278750	
27				Bef	10000	4 bar	200	15	8.05	360000	310000	16.67
				After	10000	4 bar	200	15	8.05	300000	275000	

Table 7.7 - Adiabatic CE trials operating conditions

Exp No.	Average Temperature (deg C)	Pressure across substrate (Pa)	Flow rate (LPM)	State	Concent-ration	Up stream pressure	Heated pipe temperature (°C)	Total dilution at DMS	DMS Sample flow (LPM)	Number concentration at 28 nm peak (N/cc)	Total number concentration measured at DMS (N/cc)	Preliminary CE measured at 28 nm (%)
28	152.3	18.6	150	Bef	10000	4 bar	200	11.98	8.05	680000	520000	26.47
				After	10000	4 bar	200	12	8.11	500000	410000	
29				Bef	10000	4 bar	200	12.03	8.05	675000	510000	25.78
				After	10000	4 bar	200	12.03	8.07	501000	410000	
30				Bef	10000	4 bar	200	12.05	8.03	670000	495000	25.37
				After	10000	4 bar	200	12	8.09	500000	405000	
31		28.47	236	Bef	10000	4 bar	200	11.98	8.07	400000	310000	18.75
				After	10000	4 bar	200	12	8.11	325000	260000	
32				Bef	10000	4 bar	200	11.99	8.02	400000	300000	18.75
				After	10000	4 bar	200	12.03	8.07	325000	265000	
33				Bef	10000	4 bar	200	12.05	8.03	400000	305000	18.03
				After	10000	4 bar	200	12	8.09	320000	250000	
34		57.01	473	Bef	10000	4 bar	200	11.98	8.06	155000	115000	16.13
				After	10000	4 bar	200	12	8.09	130000	100000	
35				Bef	10000	4 bar	200	12.03	8.05	150000	115000	13.33
				After	10000	4 bar	200	12	8.09	130000	98000	
36				Bef	10000	4 bar	200	12.05	8.05	145000	106000	13.79

				After	10000	4 bar	200	12	8.05	125000	97000	
37				Bef	10000	4 bar	200	11.98	8.06	225000	185000	37.78
				After	10000	4 bar	200	12	8.01	140000	115000	
38		18.8	150	Bef	10000	4 bar	200	11.99	7.99	220000	180000	36.37
				After	10000	4 bar	200	12.03	8.07	140000	115000	
39				Bef	10000	4 bar	200	11.98	8.03	210000	179000	38.1
				After	10000	4 bar	200	12	8	130000	110000	
40				Bef	10000	4 bar	200	11.75	8.04	140000	100000	28.57
				After	10000	4 bar	200	12	8.07	100000	70100	
41	201.7	28.59	236	Bef	10000	4 bar	200	11.94	8.05	139500	100500	29.89
				After	10000	4 bar	200	12.03	8.02	97800	68500	
42				Bef	10000	4 bar	200	12.05	8.03	137500	100000	30.5
				After	10000	4 bar	200	12	8.039	94800	69500	
43				Bef	10000	4 bar	200	12.04	8.06	61500	41000	18.69
				After	10000	4 bar	200	12	8.09	50000	30000	
44		57.15	473	Bef	10000	4 bar	200	12.03	8.05	62000	42100	19.35
				After	10000	4 bar	200	12	8.09	50000	31075	
45				Bef	10000	4 bar	200	12.05	8.05	65000	42500	19.07
				After	10000	4 bar	200	12	8.05	52600	31700	
46		18.8	150	Bef	10000	4 bar	200	12	7.98	170000	146500	41.17

				After	10000	4 bar	200	12	8.01	100000	90000	
47				Bef	10000	4 bar	200	11.99	8.02	168000	140000	40.47
				After	10000	4 bar	200	12.03	8.04	100000	88000	
48				Bef	10000	4 bar	200	11.98	8.03	170000	139000	41.17
				After	10000	4 bar	200	12	8.05	100000	90000	
49				Bef	10000	4 bar	200	11.75	8.04	100000	88070	25
				After	10000	4 bar	200	11.99	8.05	75000	59000	
50	252.35	31.65	236	Bef	10000	4 bar	200	11.94	8.05	100000	88006.5	30
				After	10000	4 bar	200	12.03	8.02	70000	60000	
51				Bef	10000	4 bar	200	12.05	8.03	100000	80000	27.63
				After	10000	4 bar	200	12	8.039	70000	57895	
52				Bef	10000	4 bar	200	12.04	8.06	50000	40600	20
				After	10000	4 bar	200	12	8.09	40000	30000	
53		63.56	473	Bef	10000	4 bar	200	12.03	8.05	52500	38000	26.67
				After	10000	4 bar	200	12	8.09	38500	28750	
54				Bef	10000	4 bar	200	12.05	8.05	51500	38500	22.33
				After	10000	4 bar	200	12	8.05	40000	29000	

Appendix XII: Non-adiabatic set up (Case II)

Effect of residence time on CE (at 150°C)

The effect of residence time for experiment numbers 2, 7 and 15 is evaluated (non-adiabatic set-up) .Also, the PSD_{before} and PSD_{after} results which are representing calculation of each single capture efficiency curve are also presented for each case. The results are presented in the Figure (7.11) below-

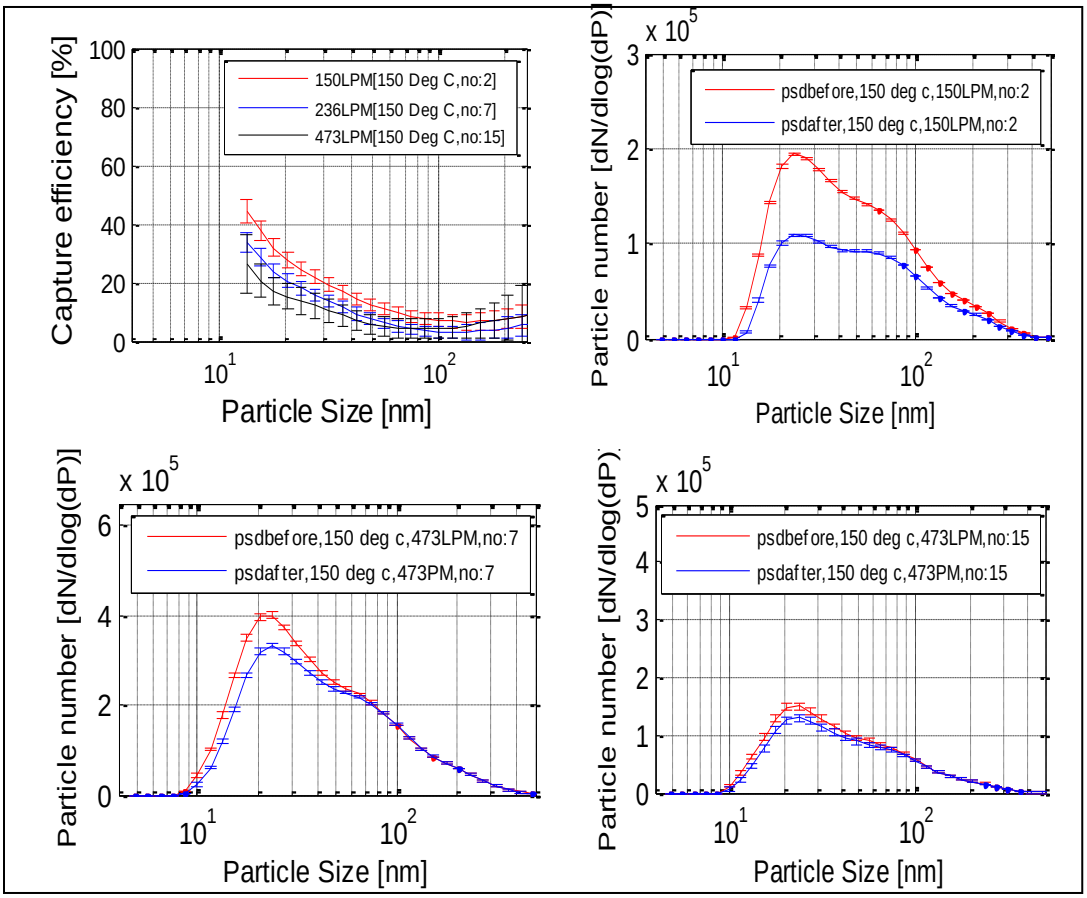

Figure 7.10 - Effect of residence time on capture efficiency at 150°C, non- adiabatic set up

Effect of residence time on CE (at 200°C)

The effect of residence time for experiment numbers 11, 14 and 17 is evaluated (non-adiabatic set-up and 200°C). The PSD_{before} and PSD_{after} results which are representing calculation of each single capture efficiency curve are also presented for each case. The flow conditions for different cases are listed in the Table (7.8).

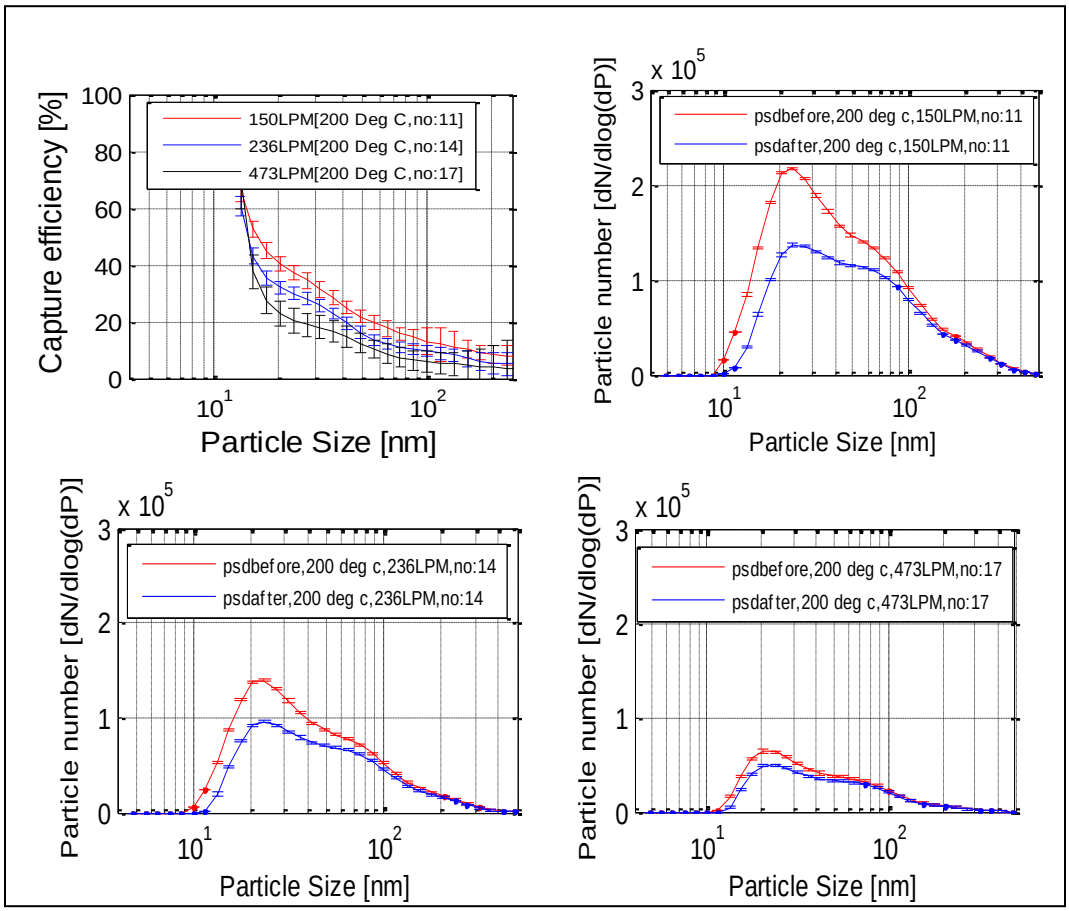

Figure 7.11 - Effect of residence time on capture efficiency at 200°C, non- adiabatic set up

Table 7.8 - CE Non- adiabatic trials summarized

Temperature	150 LPM	236 LPM	473 LPM
150 ° C (T_{avg} = 130.5 ° C)	**ΔP = 18.4 Pa** **U = 0.2 m/s** **Re = 7.76** **Sh (at 27 nm)= 10.37** **C.E (at 27 nm) = 22.83 %**	**ΔP = 28.5 Pa** **U = 0.3 m/s** **Re = 12.34** **Sh (at 27 nm)= 12.64** **C.E (at 27 nm) = 17.51 %**	**ΔP = 57.01 Pa** **U = 0.6 m/sec** **Re = 24.16** **Sh (at 27 nm)= 17.10** **C.E (at 27 nm) = 12.83 %**
200 ° C (T_{avg} = 172.5 ° C)	**ΔP = 18.8 Pa** **U = 0.2 m/s** **Re = 5.71** **Sh (at 27 nm) = 8.79** **C.E (at 27 nm) = 27.7 %**	**ΔP = 28.6 Pa** **U = 0.3 m/s** **Re = 8.92** **Sh (at 27 nm) = 10.66** **C.E (at 27 nm) = 19.66 %**	**ΔP = 57.15 Pa** **U = 0.6 m/s** **Re = 17.61** **Sh (at 27 nm) = 14.36** **C.E (at 27 nm) = 13.75 %**
250 ° C (T_{avg} = 213.5 ° C)	**ΔP = 20.95 Pa** **U = 0.2 m/s** **Re = 5.61** **Sh (at 27 nm) = 8.06** **C.E (at 27 nm) = 25.65%**	**ΔP = 31.65 Pa** **U = 0.3 m/s** **Re = 8.11** **Sh (at 27 nm) = 9.75** **C.E (at 27 nm) = 21.27%**	**ΔP = 63.56 Pa** **U = 0.6 m/sec** **Re = 15.13** **Sh (at 27 nm) = 13.09** **C.E (at 27 nm) = 15.55%**

Appendix XIII: Adiabatic set up (Case I)

Effect of residence time on CE (at 150 and 200 °C)

The effect of residence time for two remaining flow temperature of 150 (Figure 4.13) and 200°C (Figure 4.14) were assessed and are separately evaluated in this section. In addition, the PSD_{before} and PSD_{after} results which are representing calculation of each single capture efficiency curve are also presented for each case.

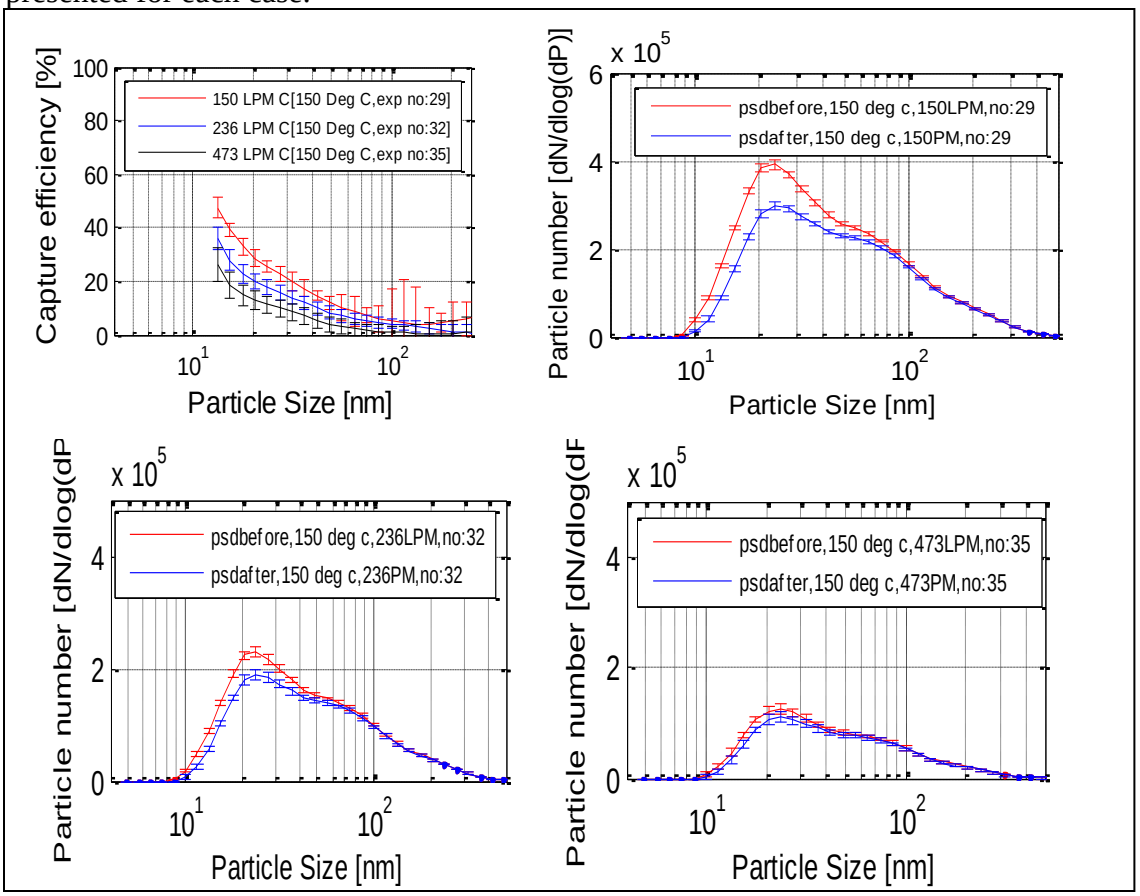

Figure 7.12- Effect of residence time on capture efficiency at 150 °C, Adiabatic set up [exp no: 29,32 and35]

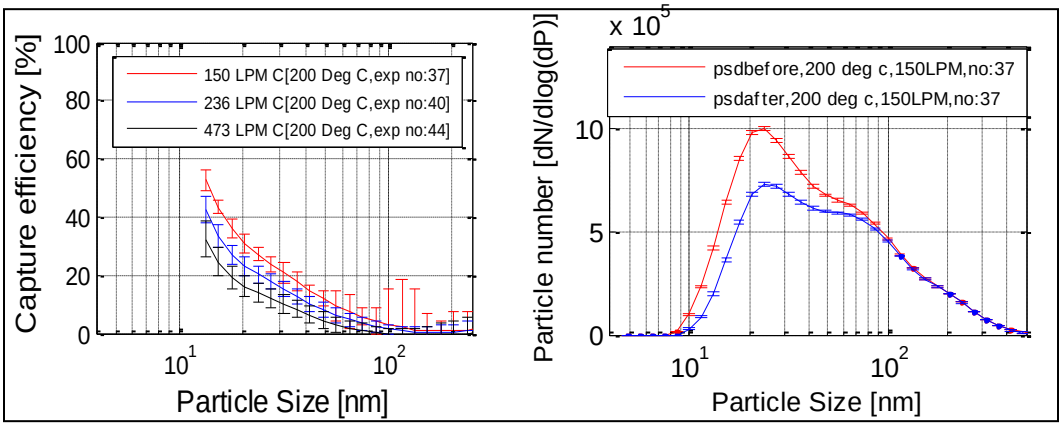

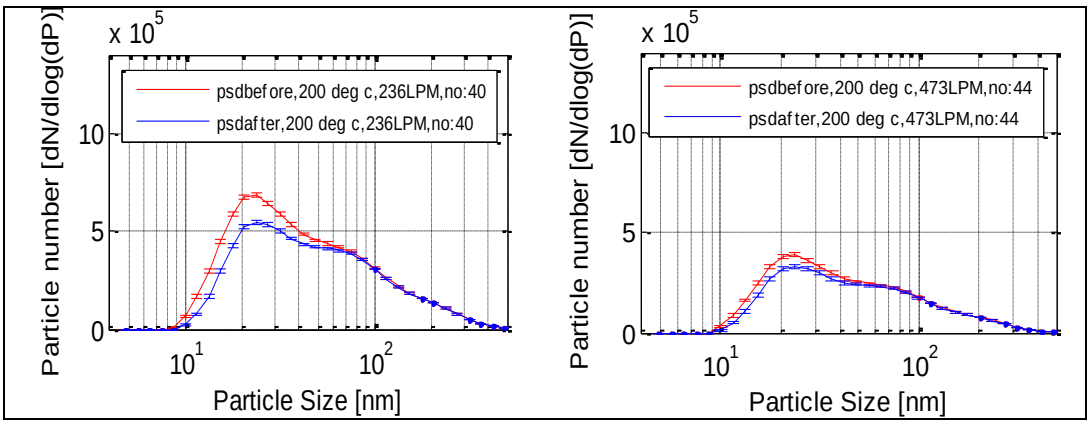

Figure 7.13- Effect of residence time on capture efficiency at 200°C, Adiabatic set up [exp no :37, 40 and 44]

Effect of temperature on CE (at 236 and 473 LPM)

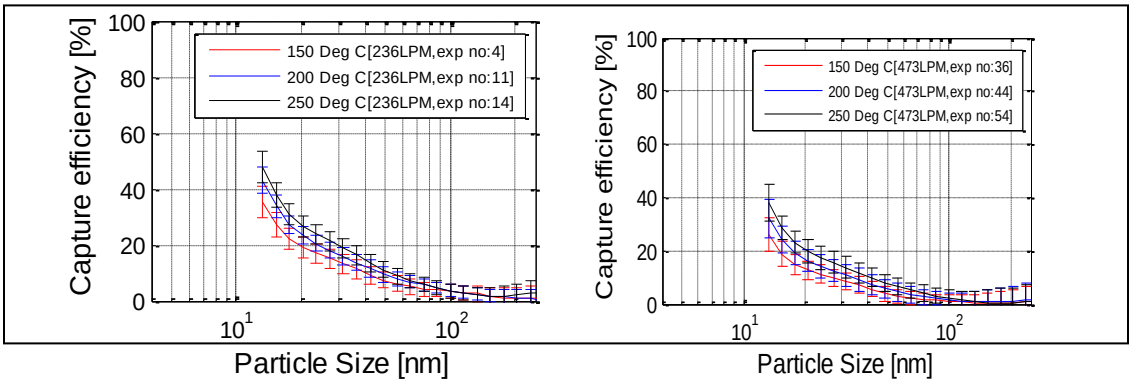

Figure 7.14 - Effect of temperature on capture efficiency at 236 (right) and 473 LPM (left)

Table 7.9 - CE adiabatic trials summarized

Temperature	150 LPM	236LPM	473 LPM
150 °C (T_{avg} = 149.6 °C)	**ΔP = 18.4 Pa** **U = 0.2 m/s** **Re = 7.78** **Sh (at 27 nm) = 10.37** **C.E (at 27 nm) = 25.87 %**	**ΔP = 28.5 Pa** **U = 0.3 m/s** **Re = 12.33** **Sh (at 27 nm) = 12.63** **C.E (at 27 nm) = 18.51 %**	**ΔP = 57.01 Pa** **U = 0.6 m/s** **Re = 24.65** **Sh (at 27 nm) = 17.10** **C.E (at 27 nm) = 14.41 %**
200 ° C (T_{avg} = 201.6 ° C)	**ΔP = 18.8 Pa** **U = 0.2 m/s** **Re = 6.05** **Sh (at 27 nm) = 8.79** **C.E (at 27 nm) = 37.41 %**	**ΔP = 28.6 Pa** **U = 0.2 m/sec** **Re = 8.83** **Sh (at 27 nm) = 10.65** **C.E (at 27 nm) = 29.65 %**	**ΔP = 57.15 Pa** **U = 0.6 m/s** **Re = 16.954** **Sh (at 27 nm) = 14.36** **C.E (at 27 nm) = 19.04 %**
250 ° C (T_{avg} = 252.6 °C)	**ΔP = 20.95 Pa** **U = 0.2 m/sec** **Re = 4.47** **Sh (at 27 nm) = 8.06** **C.E (at 27 nm) = 39.21%**	**ΔP = 31.65 Pa** **U = 0.3 m/sec** **Re = 7.74** **Sh (at 27 nm) = 9.74** **C.E (at 27 nm) = 31.2%**	**Δ P = 63.56 Pa** **U = 0.6 m/sec** **Re = 15.49** **Sh (at 27 nm) = 13.09** **C.E (at 27 nm) = 22.99%**

Appendix XIV

Comparison between adiabatic & non-adiabatic at different flow conditions are presented in the Figure (7.15) below-

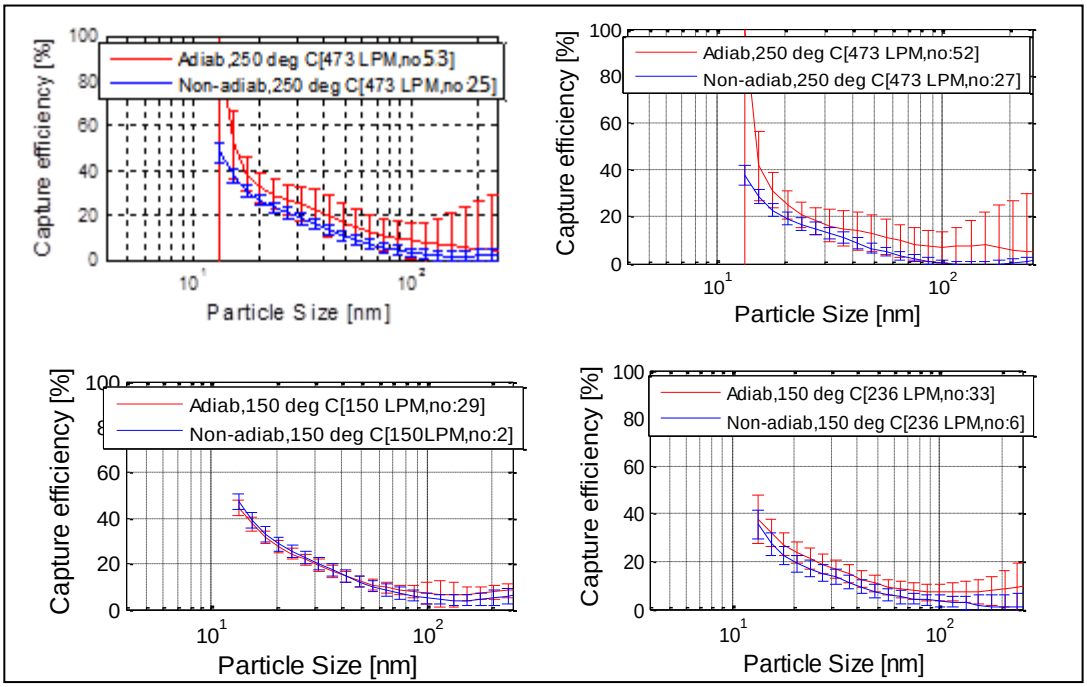

Figure 7.15- The comparison between two set ups, Adiabatic and non-adiabatic

Appendix XV: Temperature profile comparison from simulations

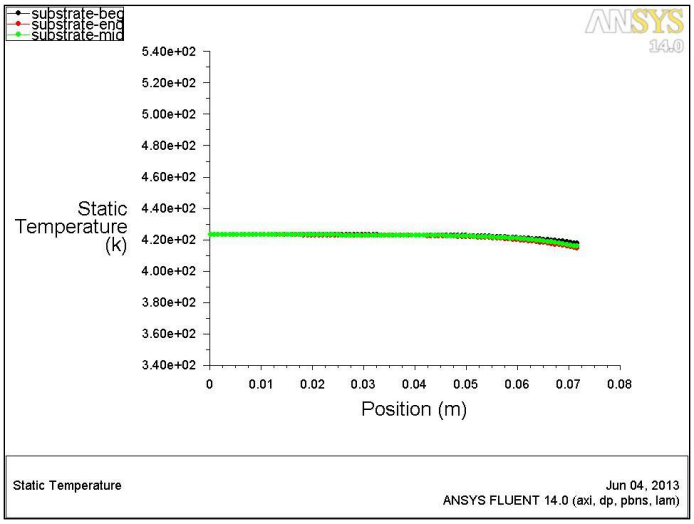

Figure 7.16 –Temperature profile for non-adiabatic substrate at 150°C and 473 LPM. The black, green and red lines represent temperature gradients at the beginning, middle and end of substrate respectively.

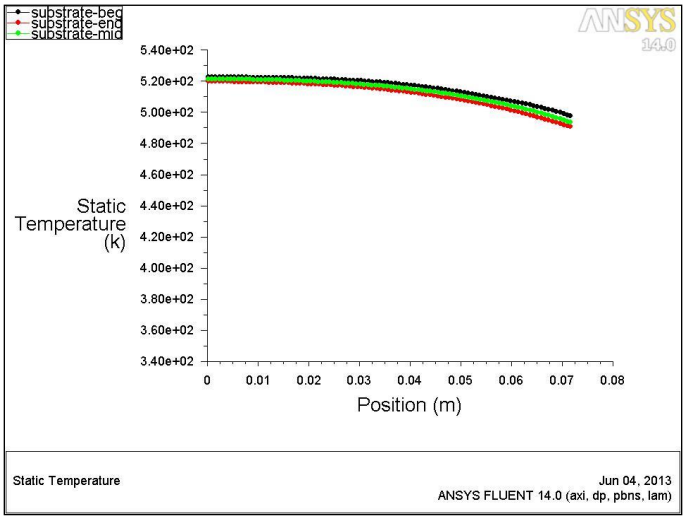

Figure 7.17 – Temperature profile for non-adiabatic substrate at 250°C and 150 LPM. The black green and red lines represent temperature gradients at the beginning, middle and end of substrate respectively.

The Figure 7.16 above represents the lower residence time (473 LPM) and lower temperature (150 °C). It is very apparent that the radial gradient is almost zero at a distance of quarter distance from the centre. The Figure 7.17 represents higher residence time (150 LPM) and higher temperature (250 °C) and it is easy to notice that temperature gradient starts from the centre of the geometry. Therefore, it can be concluded that in the first case, the average temperature of channels is higher than the second case.

Appendix XVI: Comparison between experiments and simulations

a) Adiabatic conditions

Comparison at constant temperatures

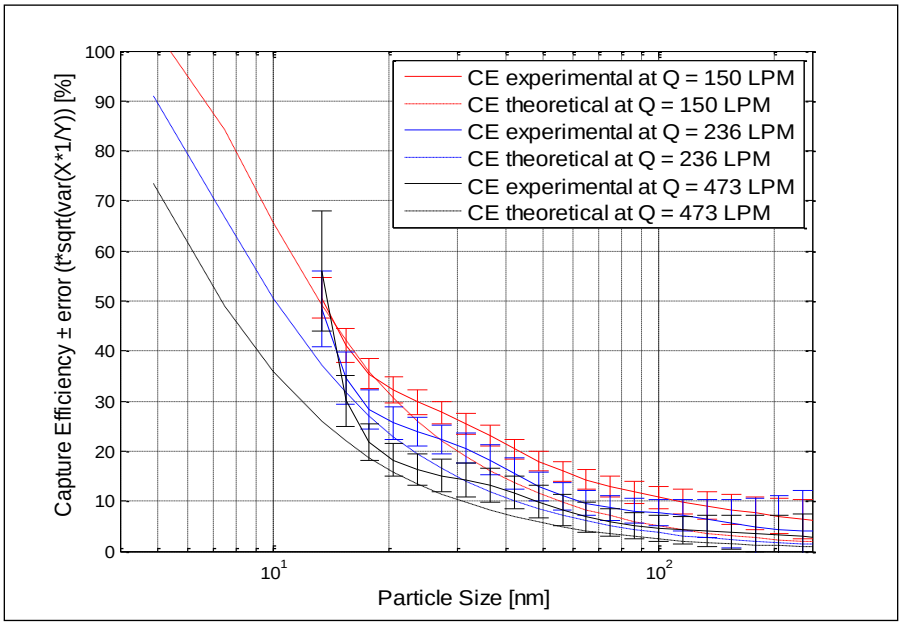

Figure 7.18 – Comparison between experiments and simulations at 200°C

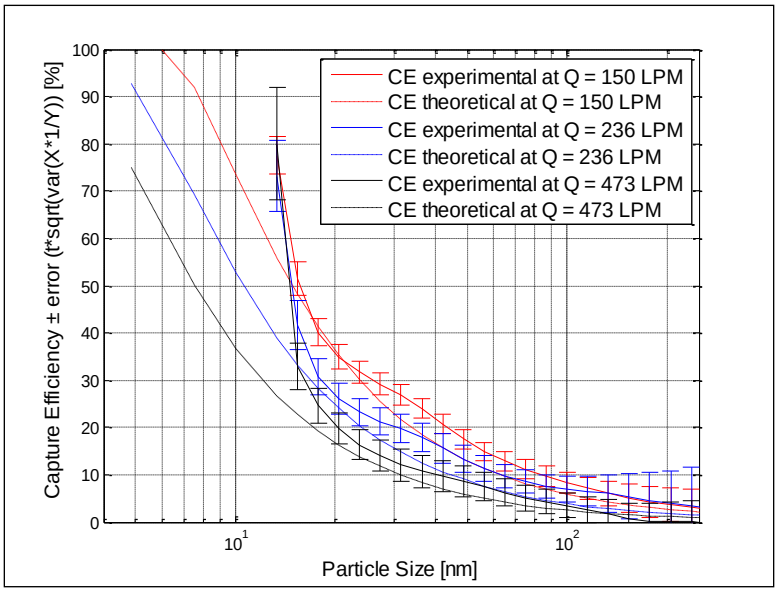

Figure 7.19 - Comparison between experiments and simulations at 250°C

Comparison at constant flows

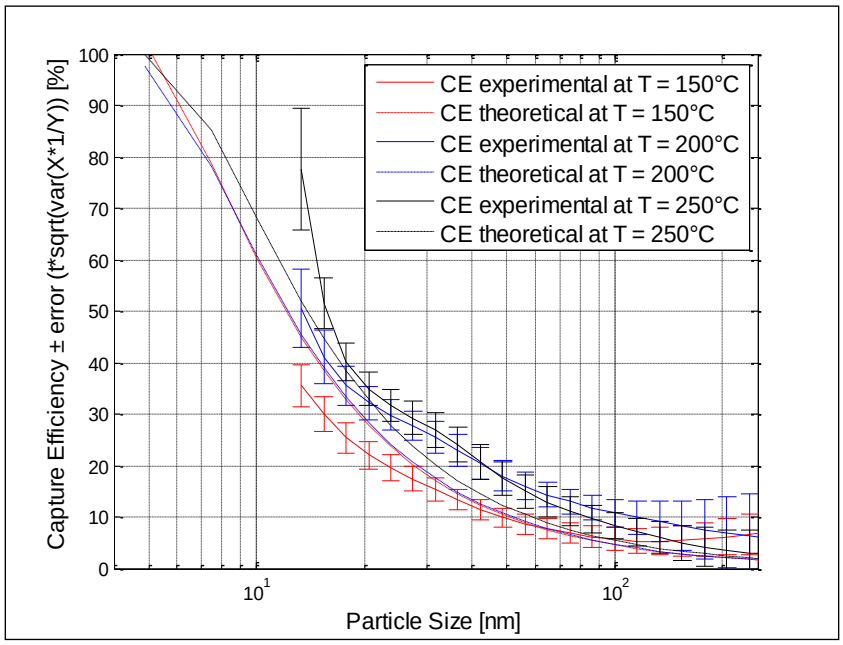

Figure 7.20 - Comparison between experiments and simulations at 150 LPM

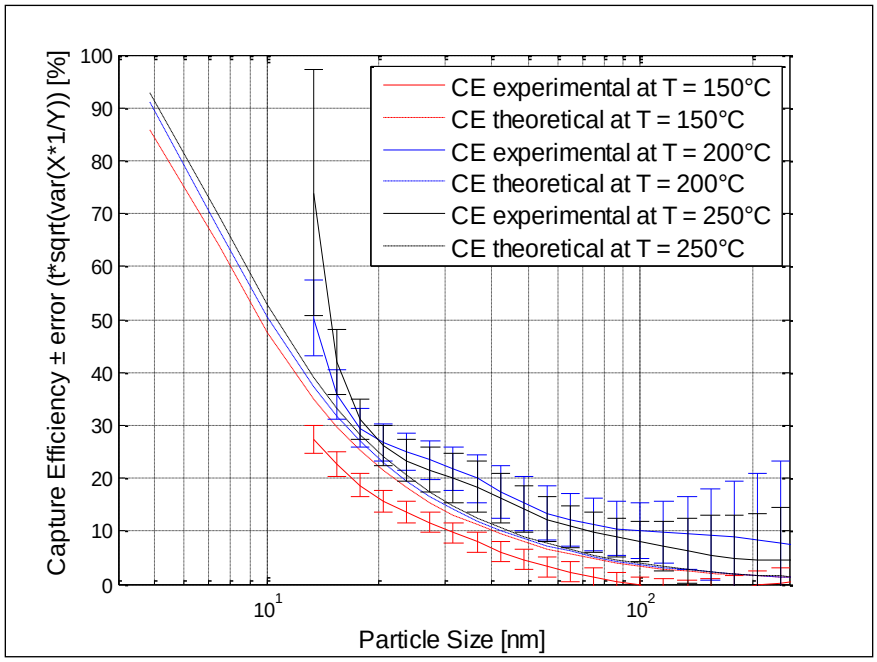

Figure 7.21 - Comparison between experiments and simulations at 236 LPM

b) Non adiabatic conditions

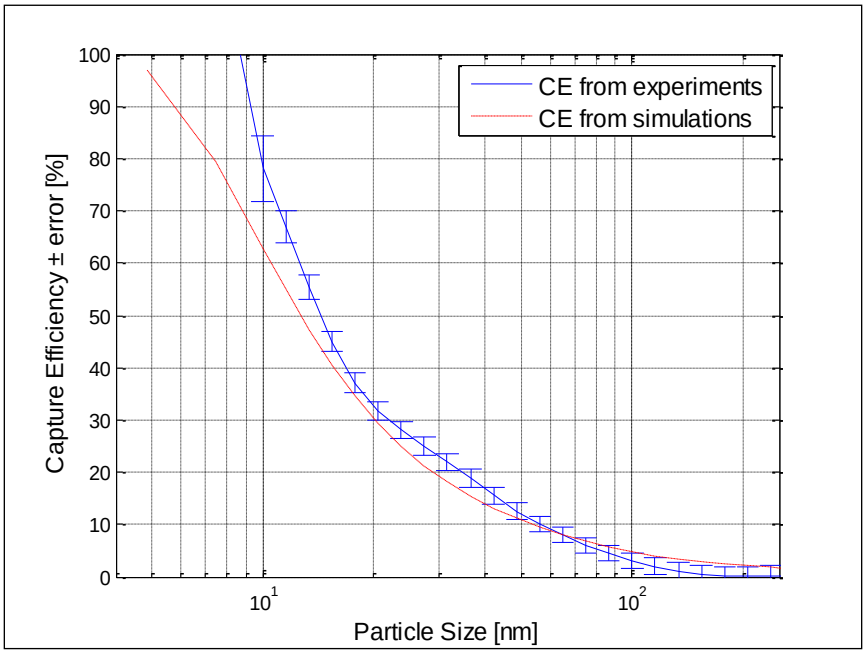

Figure 7.22 - Comparison of CE obtained from experiments and simulations (channel close the walls) at 250°C, 150 LPM

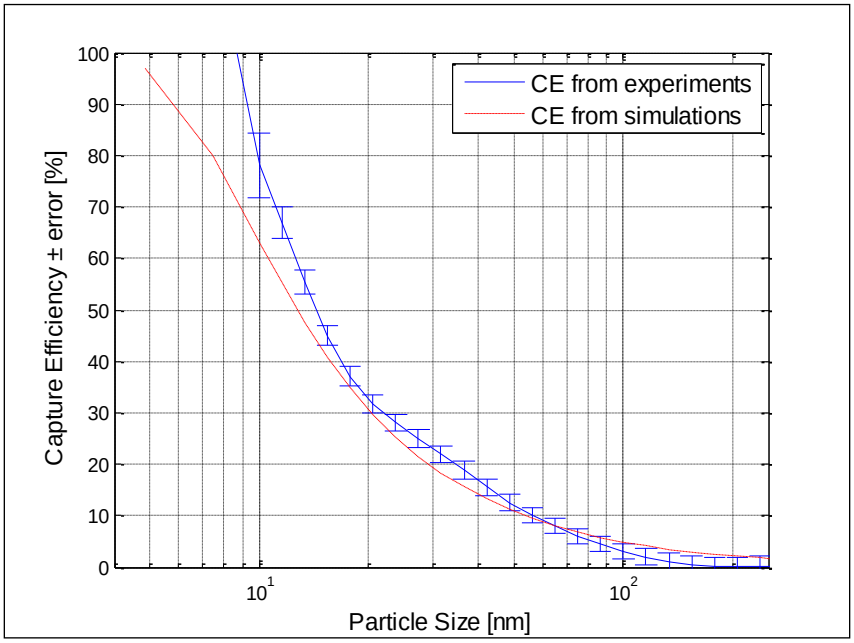

Figure 7.23 - Comparison of CE obtained from experiments and simulations (channel quarter distance away from the walls) at 250°C, 150 LPM

Figures 7.18 through 7.23 demonstrate that there is a good congruence between experiments and simulations at all chosen EATS operation points.

Appendix XVII: Sensitivity Analysis

Effect of monolith choice (channel hydraulic diameter) on CE

Square cell geometry in the wall-flow monolith with its characteristic checkerboard cell plugging pattern is shown in Figure 7.24. A number of monolith properties can be expressed in terms of the wall thickness (w) and the cell repeat distance (s), also known as the cell spacing (Gulati, Cybulski, & Moulijn, 1998)

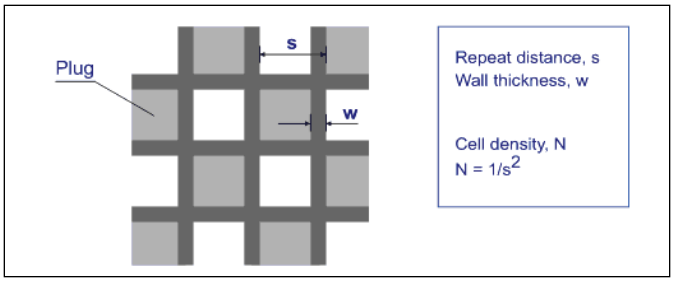

Figure 7.24 - Cell Geometry

The substrate *cell density* (N), defined as the number of channels per unit of cross-sectional area, is given for square cell geometry by Equation (1). The metric unit of cell density is $1/cm^2$, with the customary unit of cells per square inch (cpsi) widely used in the industry.

$$N = 1/s^2 \qquad (1.1)$$

Cell *hydraulic diameter* (d_h) is a measure of channel size used in hydraulics, mass transfer and heat transfer calculations. In the case of square cells, it can be simply expressed as the difference between repeat distance and wall thickness, as follows:

$$d_h = s - w \qquad (1.2)$$

The commercial cell substrates along with the respective values for 's' and 'w' are provided in the table below –

Table 7.10 – Common substrate geometries used in diesel cars

Geometry[4] type	Repeat distance (s) in mm	Wall Thickness (w) in mm	Hydraulic diameter (dh) in mm
300/6	1.46	0.15	1.31
400/6	1.27	0.15	1.11
500/6	1.13	0.15	0.98
600/6	1.03	0.15	0.88

The CE sensitivity (plotted using the theoretical CE expression Equation (1.15)) towards the change in geometry is shown in the figure below –

[4] The geometry provides 300, 400, 500 and 600 cell substrates per square inch (cpsi) with a wall of thickness 6/1000th of an inch.

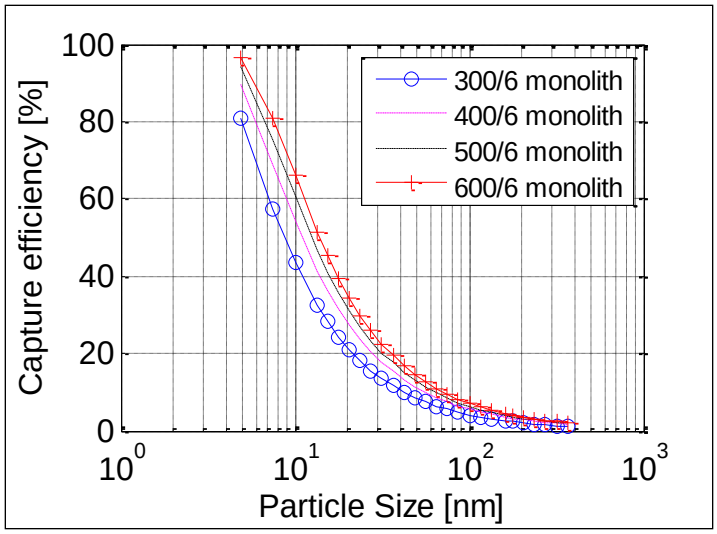

Figure 7.25 – Sensitivity of CE towards monolith type (varying dh) at 250°C and 150 LPM

The 600/6 monolith has the highest CE due to the smaller hydraulic diameter (shorter diffusion lengths). The noticeable trend is increase in CE with increase in cpsi of the monolith.

Effect of temperature on CE

The effect of temperature on CE has been extensively demonstrated in the Section 4.0. This appendix would extend this discussion by reaching the upper boundaries of conventional engine exhaust. Temperatures of 150, 250, 350 and 450°C have been examined (plotted using the theoretical CE expression Equation (1.15)).

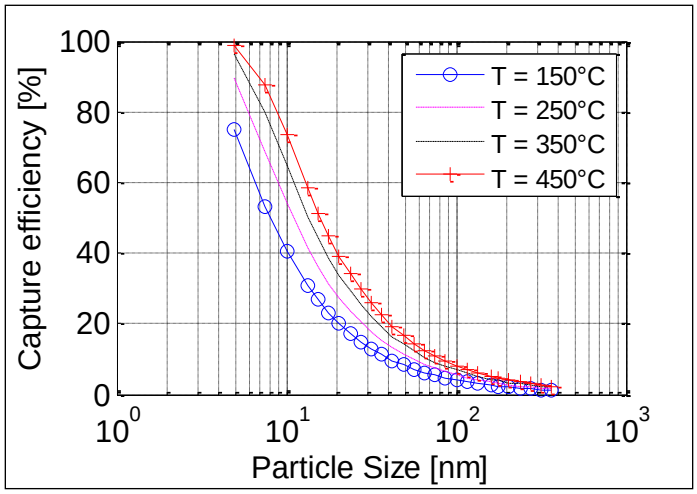

Figure 7.26 - Sensitivity of CE towards temperature at 150 LPM

Effect of engine exhaust flow on CE

Maximum exhaust gas flow is an important parameter for the aftertreatment device and other exhaust system components. Exhaust flow data may be available from the engine manufacturer or from other sources. Comprehensive listings of maximum exhaust gas flow and temperature

are often published by exhaust system and muffler manufacturers (Donaldson, 2009). A very approximate estimate of maximum exhaust flow based on rated engine power, is shown in Figure 7.27 below -

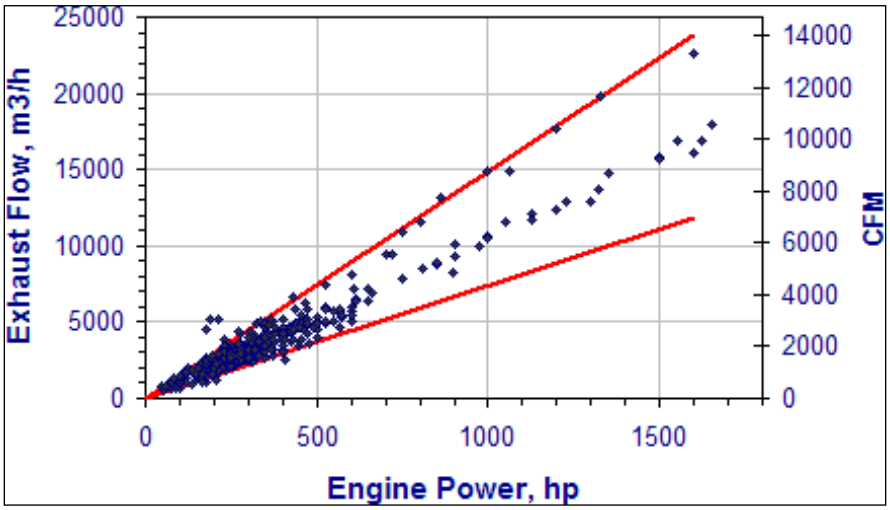

Figure 7.27 - Maximum Exhaust Flow Rate As Function of Engine Rated Power

The data in the chart correlates well with the traditional rule of thumb, which states that the flow rate of hot exhaust gas in m^3/h equals the engine power (in HP) multiplied by 10 (or by 6 to obtain the flow rate in CFM). The reader is cautioned however that this simple rule of thumb is subject to errors as high as ± 40 % (Donaldson, 2009).

A typical exhaust flow from an engine would be about 250 - 600 CFM for a 50 - 100 HP engine (nominal range of BHP observed in a diesel car). The sensitivity based on these respective engine exhaust flows is discussed here.

Table 7.11 – Common exhaust gas flows from diesel cars

Volumetric flow(CFM)	Volumetric flow(L/min)	Volumetric flow(m3/s)	Channel Inlet velocity (m/sec)
250	7079.21	0.11	9.36
425	12034.65	0.20	15.91
600	16990.10	0.28	22.47

These 3 flows are compared with the flows utilized in this work i.e., 150, 236 and 473 LPM (plotted using the theoretical CE expression Equation (1.15)),

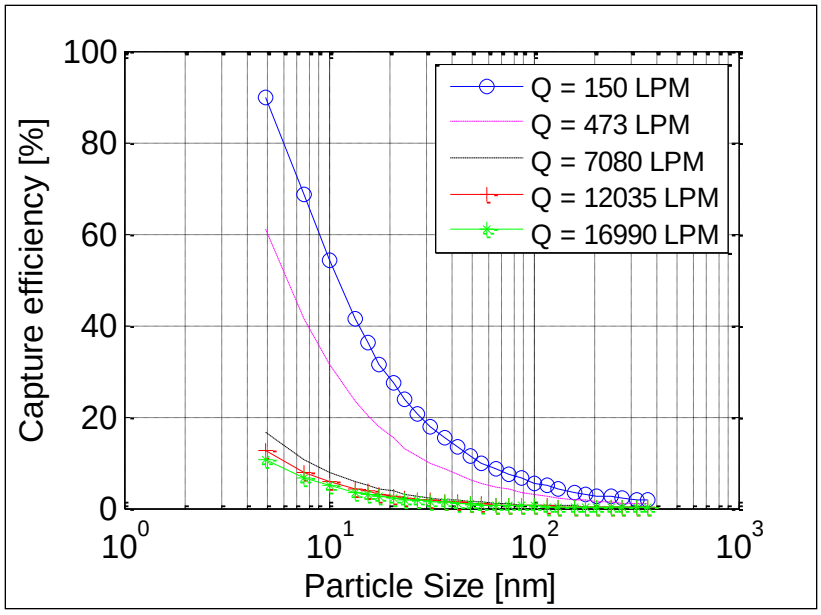

Figure 7.28 - Sensitivity of CE towards engine exhaust flow at 250°C

The common exhaust flows (7080, 12035 and 16990 LPM) noticed in a conventional diesel automotive would correspond to significantly lower ranges for PM CE (about 1- 20 % for a particle size range between 5- 90 nm). If these flows were chosen as experimental operating conditions, it would be very hard to notice any significant trends in the CE. Moreover at such high flows, the DMS signal to noise ratio would also be high leading to PM measurement at levels very close to the limit of detection of the instrument. Thus in order to appreciate the varying trends noticeable in CE of PM in an open substrate it is necessary that the substrate flows are sufficiently low.

Appendix XVIII: Accuracy of CFD results

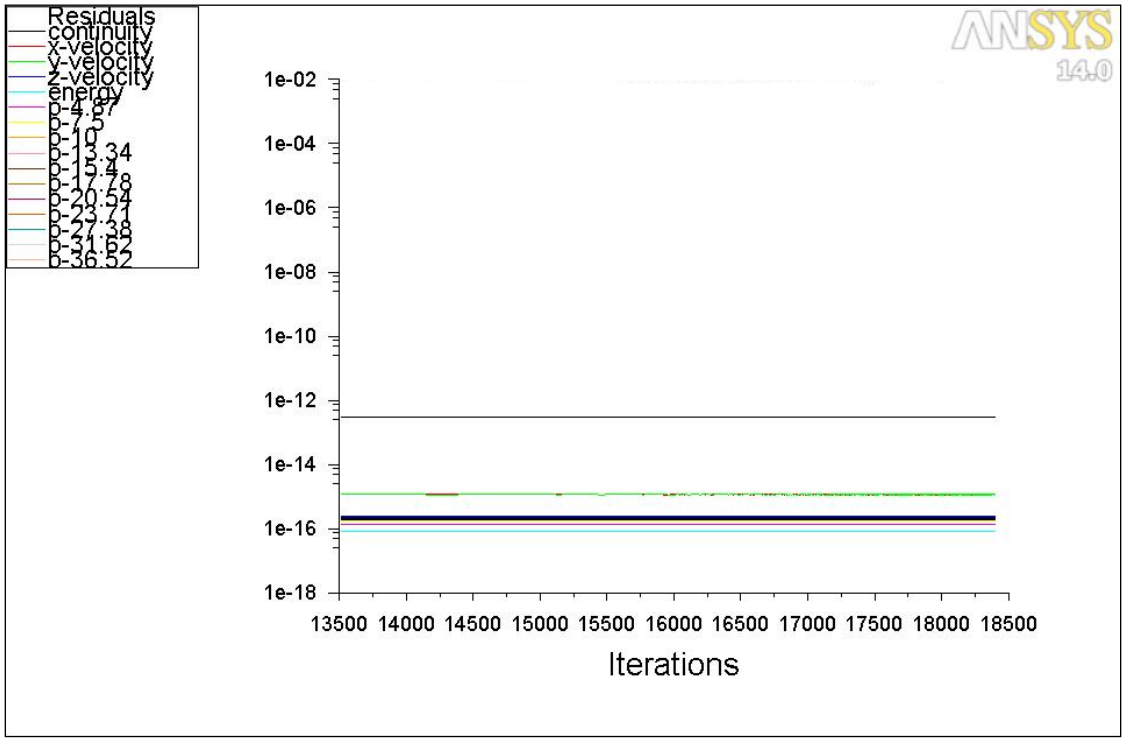

Figure 7.29 - Scaled residuals (for adiabatic channel simulation at 250°C and 150 LPM)

The Figure 7.29 above clearly demonstrates that the residuals of the solved variables (like x-velocity, y-velocity, species etc.) are well within below the cut-off value of $1e^{-6}$.

The mass fraction at the outlet (based on mass weighted average) of species 'p-365' was used as a metric to judge for convergence. Convergence was reached when there were minimal fluctuations in this value noted.

Appendix XIX: Comparison between theory and simulations (Validation of CFD results)

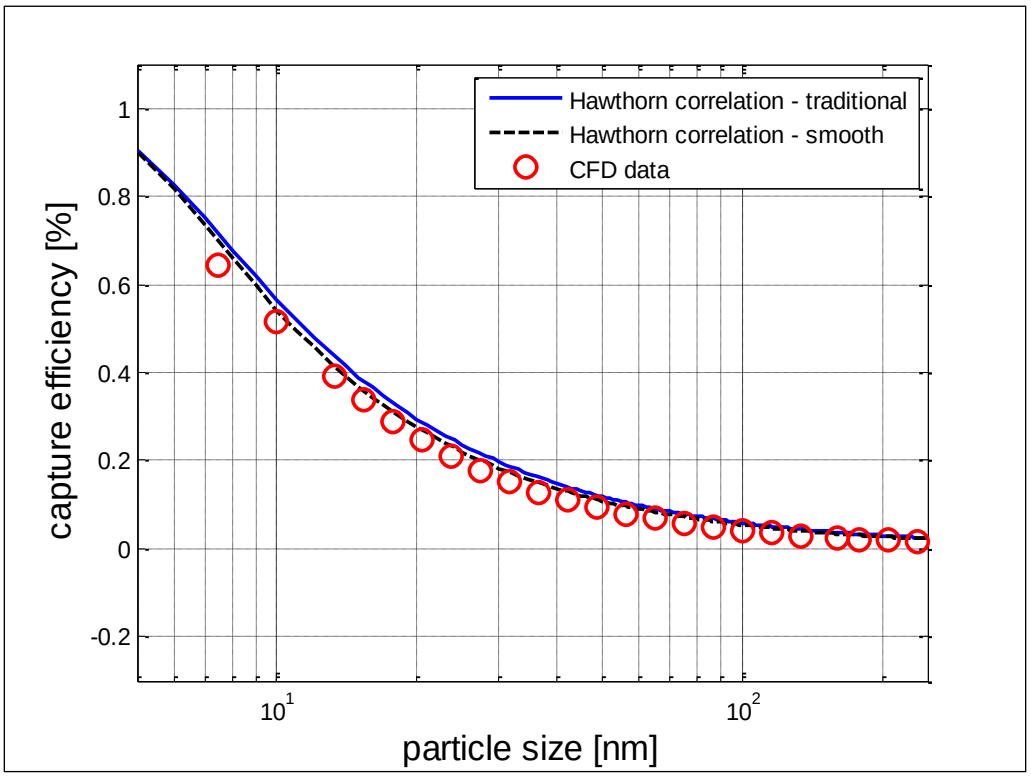

Figure 7.30 - Comparison between theory and simulations

The theoretical estimations and the CFD simulations agree very well. The former are based on empirical correlations and use only averaged values from the monolith channel. Thus, the correlations must ideally over-predict the CE's. This feature is generally used to validate simulations done in a single monolith channel in particular (Ström, 2011). The results obtained from the simulations were compared with the theoretical correlations (Equation (1.15), (1.16) and (1.17)) for each and every case. The result of one of these comparisons is shown in the Figure 7.30 above. The simulations results are clearly below the over-predicted results from theoretical expressions. Thus the simulation results are judged to have been accurate and could be relied upon.